MASTER THESIS

Thesis submitted in partial fulfillment of the requirements for the degree of Master of Science in Engineering at the University of Applied Sciences Technikum Wien

Degree Program in Tissue Engineering and Regenerative Medicine

Modeling of a Novel Filamin-C Mutation in Restrictive Cardiomyopathy using hiPSC-derived Cardiomyocytes

By: Beatrice Gabbin, BSc
Student Number: 1810692024

Supervisor 1: Dr. William Pu, MD
Dr. Maksymilian Prondzynski, PhD
Supervisor 2: Dorota Szwarc, MSc

Boston, September 29, 2020

FH University of Applied Sciences TECHNIKUM WIEN

Declaration of Authenticity

“As author and creator of this work to hand, I confirm with my signature knowledge of the relevant copyright regulations governed by higher education acts (see Urheberrechtsgesetz/ Austrian copyright law as amended as well as the Statute on Studies Act Provisions / Examination Regulations of the UAS Technikum Wien as amended).

I hereby declare that I completed the present work independently and that any ideas, whether written by others or by myself, have been fully sourced and referenced. I am aware of any consequences I may face on the part of the degree program director if there should be evidence of missing autonomy and independence or evidence of any intent to fraudulently achieve a pass mark for this work (see Statute on Studies Act Provisions / Examination Regulations of the UAS Technikum Wien as amended).

I further declare that up to this date I have not published the work to hand nor have I presented it to another examination board in the same or similar form. I affirm that the version submitted matches the version in the upload tool.”

Boston, September 29, 2020

Place, Date

Signature

Abstract

The purpose of this project was to establish an *in vitro* model for a novel *FLNC* missense mutation (c.7416_7418delGAA/p.Glu2472_Asn2473delAsp), which was identified at the Boston Children's Hospital in a patient diagnosed with restrictive cardiomyopathy (RCM). The mutation was studied with the use of use of human induced pluripotent stem cell- (hiPSC) derived cardiomyocytes (hiPSC-CMs) by applying two- and three-dimensional (2D, 3D) models, with the ultimate goal of developing a new therapeutic approach for the affected patient as well as other RCM patients.

The *FLNC* mutation was introduced by CRISPR/Cas9 genome editing into healthy control hiPSCs. CRISPR/Cas9-edited hiPSCs and their isogenic controls were differentiated into cardiomyocytes and assessed for differentiation efficiency and their genotype was determined. 2D and 3D disease modeling approaches recapitulated the restrictive phenotype caused by the novel *FLNC* mutation. Immunofluorescence assays showed and altered sarcomeric structure of mutant cardiomyocytes, whereby mRNA and protein expression analysis suggested that cells are undergoing extensive sarcomeric remodeling. 3D model of engineered heart tissues (EHTs) was able to give further insights on contraction parameters such as force, time and relaxation. Mutant EHTs showed lower contraction force and conduction deficiencies.

These important parameters resembled an RCM phenotype *in vitro* that will lay the basis for further understanding of disease mechanisms that lead to RCM and the testing of novel therapeutic approaches.

Acknowledgements

In these past two years, science gave me the opportunity to get to know incredible people who accompanied me through my journey and enriched me day after day, both professionally and personally.

I would like to start by thanking Dr. William Pu for having me as a student in his group at Boston Children's Hospital. Coming to work for a prestigious Harvard Medical School's associate laboratory was a privilege. Thank you to all the Pu lab team and staff who I worked with and always offered me a helping hand when needed.

A special thank goes to Dr. Maksymilian Prondzynski. Dear Maks, you are one of those teachers who made an impact in my academic career. You were a great supervisor and an inspiring researcher. Your passion for science is tangible and your curiosity contagious. Working together was a pleasure and I had a lot to learn from you as a young scientist.

I would like to thank the Austrian Marshall Plan Foundation for granting me the scholarship which allowed me to do research in the United States for my master thesis.

Thank you to Dr. Andreas Teuschl, program director of the master program, for being supportive and involved with his students. Moreover, I would like to thank my supervisor Dorota Szwarc for her constructive feedback and her availability.

Thank you to my friends: the old ones, the new ones and the ones who have been there for me even through hard times. I have always valued friendship, but never before this year I fully understood how important it is to have friends in your life. In particular, thank you to my friends from Italy for showing me love even across an ocean. Thank you to my amazing friends from Vienna and the memories we made together. Thank you to my friends from Boston and for making the lockdown caused by the global pandemic more tolerable. You were my family away from home.

Lastly, my greatest thank goes to my family. Being away from you during such tough times was one of the hardest situations that life put me through. Nevertheless, you have always infused me with positivity and continued to be my biggest supporters. I would never be who I am today if it was not for you and what you taught me: the ones who never doubted either my stubborn ambitions or my abilities, even if they caused us to be far away from each other. Thank you for making me believe that anything is possible if you truly want it. Cara nonna, grazie per aver contato i giorni che ci separavano dal rivederci ogni volta che partivo per un viaggio. Grazie per avermi insegnato che è importante lavorare duro per ottenere ciò che si vuole nella vita.

This year has been so far very challenging, but also full of experiences that led me to a huge self-improvement. Despite the difficulties, I consider myself proud of my achievements and grateful for being where I am now in life. Thanks to university years and internships, I opened my eyes to the beauty of science, and I could not be more excited to see what the future brings.

Table of Contents

1 Introduction

1.1 Restrictive cardiomyopathy

Restrictive cardiomyopathy (RCM) is a disease characterized by increased myocardial stiffness, which reduces filling for either or both the right and left ventricle, leading to a subsequent dysfunction of the diastolic phase. Systolic function usually remains normal at least in early stages of the disease, while wall thickness can either be normal or increased depending on the underlying cause. In addition to heart failure, arrhythmias and disturbances in conduction frequently occur [1]. *Figure 1* shows the cross-section of the anatomy of a normal heart compared to an RCM heart.

Cardiomyopathies have a lower incidence in children than in adults, occurring in approximately 1.1-1.5 per 100,000 children up to 18 years old [2]–[4]. The diseases carry a substantial risk of morbidity and mortality and are the primary indication for a heart transplant in childhood. Children affected by RCM make up <5% of cardiomyopathy cases [5], [6]. Pediatric RCM has the poorest outcome with a 1-year and 5-year transplant-free survival of 48% and 22%, respectively [7].

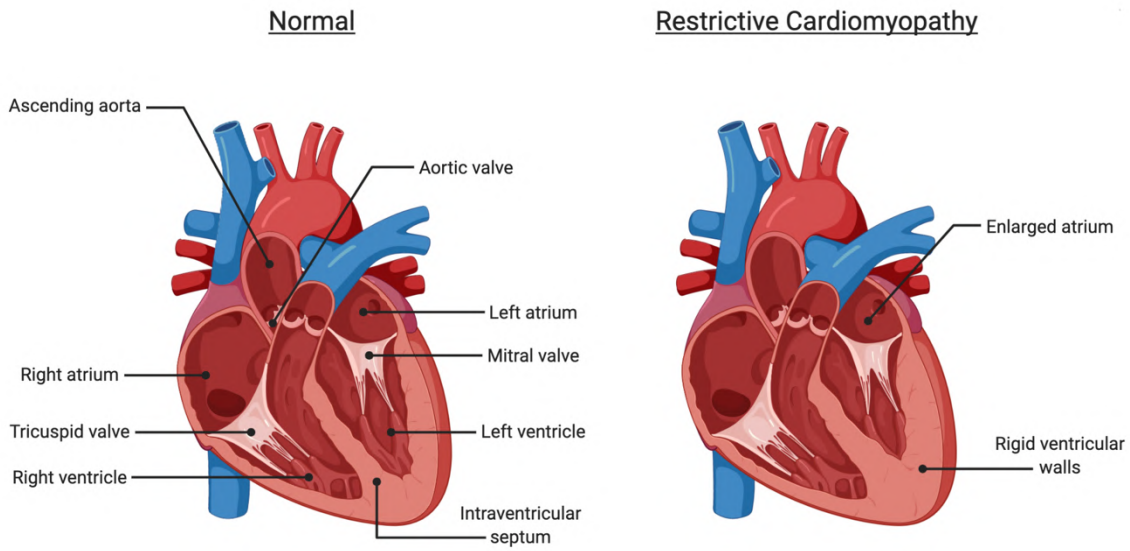

Figure 1. **Comparative illustration of a normal heart and a heart affected by RCM.** The figure shows the cross-section of the anatomy of a normal heart compared to one affected by restrictive cardiomyopathy. RCM is a type of cardiomyopathy in which heart muscle is replaced by abnormal tissue, causing ventricular stiffness and rigidity. As ventricles are not able to normally relax and fill with blood, atria become enlarged and blood flow is reduced. Figure generated with *BioRender*.

RCM has diverse etiologies, some systemic and some localized to the myocardium. *Table 1* gives an overview of the classification of the different classes of RCM according to cause, which are broadly defined as noninfiltrative, infiltrative or endomyocardial [1], [8].

Table 1. **Classification of types of RCM according to cause.** Adapted from [8].

Myocardial
Noninfiltrative
Idiopathic cardiomyopathy*
Familiar cardiomyopathy
Hypertrophic cardiomyopathy
Scleroderma
Pseudoxanthoma elasticum
Diabetic cardiomyopathy
Infiltrative
Amyloidosis*
Sarcoidosis*
Gaucher disease
Hurler disease
Fatty infiltration
Storage diseases
Hemochromatosis
Fabry disease
Glycogen storage disease
Endomyocardial
Endomyocardial fibrosis*
Hypereosinophilic syndrome
Carcinoid heart disease
Metastatic cancers
Radiation*
Toxic effects of anthracycline*
Drugs causing fibrous endocarditis (serotonin, methysergide, ergotamine, mercurial agents, busulfan)

*More likely than others to be encountered in clinical practice

Part of the noninfiltrative spectrum is idiopathic restrictive cardiomyopathy (iRCM), which presents no specific histopathological changes but hemodynamic abnormalities. The disease is characterized by a mild to moderate increase in cardiac weight; biatrial enlargement and often the presence of thrombi in atrial appendages. Cavity size and wall thickness of ventricles are average, with normal or reduced systolic function. If pulmonary hypertension occurs, the right ventricle may become enlarged. Moreover, patches of endocardial fibrosis are seen; interstitial fibrosis is usually patchy and can range from non-

existent to severe (*Figure 2*). The sinoatrial and atrioventricular nodes can also be affected by fibrosis, resulting in complete heart block that requires permanent pacing [8].

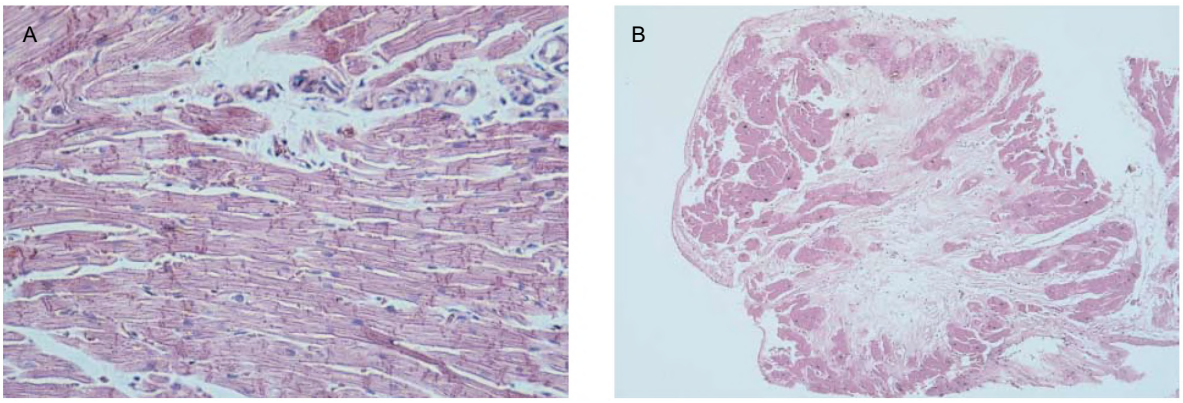

Figure 2. **Endomyocardial biopsy from an iRCM heart.** Histological sections from heart biopsies of two patients affected by iRCM. (A) Hematoxylin and eosin staining shows myocytes with slight hypertrophy (X250). (B) Marked interstitial fibrosis can be seen (X40). Adapted from [8].

Systemic disorders that result in accumulation of material within the heart can cause RCM. Among these disorders are storage diseases like Gaucher disease, Hurler disease and Fabry disease. Interstitial inflammation can be caused by cardiac sarcoidosis and initially impair diastolic function, while systolic function usually remains normal until subsequent injury and fibrosis. Hypokinesia can occur, but also focal abnormalities of regional wall motion and myocardial involvement. The course of the disease is variable, and death can occur in patients who showed no preexisting symptoms, but are rapidly worsening [8].

Primary amyloidosis is an infiltrative form of RCM and is caused by the plasma cells' production of immunoglobulin light chains. It is thought to result from injury to tissue due to infiltrative interstitial deposits of misfolded proteins as amyloids, replacing normal myocardial contractile elements [1]. Inherited forms of amyloidosis associated with RCM are caused by genetic variants of the plasma protein prealbumin (transthyretin). Patients affected by cardiac amyloidosis have a firm, rubbery and noncompliant myocardium. Ventricular cavities are usually normal or small to moderately dilated and characterized by the presence of thrombi in atrial appendages. Histological examination shows interstitial deposition of insoluble amyloid fibrils in all chambers, resulting in increased wall thickness without cavity dilatation. Other involved cardiac components include the pericardium, cardiac valves and coronary arteries. Amyloid deposits can also be found in bundle branches and in the sinoatrial and atrioventricular nodes. Consequently, a variety of cardiac arrhythmias can occur. Patients can present combinations of asymmetric septal thickening, angina, heart failure, abnormal diastolic function and reduced ejection fraction depending on the stage of the disease [8].

The other two common forms of infiltrative RCM, which are more likely to be encountered in clinical practice, are cardiac sarcoidosis and cardiac hemochromatosis. Cardiac sarcoidosis is characterized by the presence of T lymphocytes, mononuclear

phagocytes and noncaseating granulomas in involved tissues. Yet, the cause of this multisystem inflammatory disease remains unknown. On the other hand, cardiac hemochromatosis is caused by the increased absorption of dietary iron accumulating in various organs and leading to their dysfunction. Cardiac involvement occurs between 15% and 20% of cases and is less common than liver involvement or the incidence of diabetes mellitus or skin abnormalities [1].

Endomyocardial fibrosis and eosinophilic cardiomyopathy are thought to be manifestations of restrictive cardiomyopathy and are part of the endomyocardial forms of RCM. They are associated with eosinophilia, as the intracytoplasmic granular content of activated eosinophils is presumably responsible for the toxic damage to the heart. Prognosis for patients affected by endomyocardial fibrosis is poor and mostly depends on the degree and location in the heart. This disease typically has an insidious onset and failure of right- or left-sided heart increases severely over time. Even though sudden death and syncopal episodes are not common in this type of RCM, atrial fibrillation occurs and is more frequent in patients with right ventricular disease. Low QRS voltage, first-degree atrioventricular block and left atrial enlargement are among other electrocardiographic abnormalities. Moreover, thickening of the inferior basal left ventricular wall and endocardial deposition of thrombus with apical obliteration and mitral regurgitation can occur. Heart size in endomyocardial fibrosis is usually normal, while ventricular cavities vary in size and are markedly damaged by extensive endocardial thickening. The subendocardium may show patchy fibrosis and chronic valve regurgitation is often present [8].

Other restrictive conditions include carcinoid heart disease, which occurs as a late complication of the carcinoid syndrome in almost half of cases and shows tricuspid regurgitation as the predominant lesion. Fibrous plaques involving the tricuspid, pulmonary valves and the right ventricular endocardium are pathological lesions [8].

Table 2. **Genetic causes for RCM.** Adapted from [9].

Gene	Protein	Function	
ACTC1	Cardiac Actin	Sarcomere protein	[9]
ACTN2	α-Actinin 2	Z-band protein	[10]
BAG3	Bcl-2 Associated Athanogene 3	Co-chaperone	[11]
CRYAB	αB-Crystallin	Chaperone-like activity	[13]
DES	Desmin	Intermediate filament protein	[14]
FLNC	Filamin C	Cell junction organization	[15]
MYBPC3	Myosin Binding Protein C3	Sarcomere protein	[15]
MYH7	Myosin Heavy Chain 7	Sarcomere protein	[16]
MYH6	Myosin Heavy Chain 6	Sarcomere protein	[17]
MYL2	Myosin Light Chain 2	Sarcomere protein	[18]
MYL3	Myosin Light Chain 3	Sarcomere protein	[19]
MYPN	Myopalladin	Z-band protein	[21]

TMEM87B	Transmembrane Protein 87B	Endosome-to-trans-Golgi retrograde transport	[22]
TNNC1	Cardiac Troponin C	Sarcomere protein	[22]
TNNI3	Cardiac Troponin I	Sarcomere protein	[24]
TNNT2	Cardiac Troponin T	Sarcomere protein	[24]
TTN	Titin	Sarcomere protein	[26]
TPM1	Tropomyosin 1	Sarcomere protein	[27]
LMNA	Lamin A/C	Nuclear envelope	[28]
ABCC9	ATP-binding Cassette Subfamily C Member 9	ATP-binder transporter	[29]
CBL	Cbl proto-oncogene	E3 ubiquitin-protein ligase	[30]
ADD3	Gamma-adducin	Membrane skeletal protein	[30]
TTR	Transthyretin	Binding and transport of retinol and thyroxine	[32]

The discovery of specific gene mutations responsible for RCM is increasing in frequency thanks to the application of next generation sequencing technologies [33]. *Table 2* lists known genetic causes for RCM, distinguishing proteins based on their function.

The association of RCM with sarcomeric abnormalities has been made in both children and adults. Mutations in troponin I, beta myosin heavy chain and myosin light chains were encountered in patients exhibiting hypertrophic cardiomyopathy (HCM) or RCM [33]. In a study conducted by Webber *et al.*, patients were sorted into a HCM, RCM and HCM/RCM cohort and analyzed for event-free survival. The authors showed that the RCM/HCM group had significantly better event-free survival than the pure RCM group, suggesting that transplantation could be deferred for longer periods in the subgroup with a better prognosis [33], [7].

1.1.1 Diagnosis and treatment of RCM

Cardiac characterization is an important part of the evaluation of patients affected by RCM and should always be performed at diagnosis [33]. The diagnosis should be considered in patients with normal or near-normal systolic function presenting evidence of diastolic dysfunction and restrictive echocardiography filling patterns [1]. Symptoms of RCM include dyspnea, paroxysmal nocturnal dyspnea, orthopnea, peripheral edema, ascites and general fatigue and weakness. Angina generally occurs just in amyloidosis, while in advanced cases all signs of heart failure are present except cardiomegaly. Such clinical signs and symptoms are similar to those of severe constrictive pericarditis, and because of this the diagnostic approach should initially rule it out. One third of patients affected by iRCM may also show signs of thromboembolic pericarditis. Amyloidosis and sarcoidosis commonly show conduction disturbances; atrial fibrillation is common in iRCM and cardiac amyloidosis [8].

Particularly in children, symptoms of RCM include respiratory complaints, dyspnea on exertion, asthma and recurrent lower respiratory tract infections as well as exercise

intolerance. Abnormal heart sounds like gallop, loud P2 and murmur, hepatomegaly and ascites are among abnormal physical examination findings. Other signs and symptoms include chest pain, syncope, and sudden death. The electrocardiogram signal shows abnormalities in approximately 98% of cases. Common abnormalities are right and left atrial enlargement, ST segment depression and ST-T wave abnormalities. Ventricular hypertrophy and conduction abnormalities can be detected too. Pediatric patients have been reported with arrhythmias, which include atrial flutter, high-grade second- and third-degree atrioventricular block, atrial fibrillation, atrial tachycardias, Wolff-Parkinson-White syndrome with supraventricular and ventricular tachycardia and torsade and sinus bradycardia requiring pacing. Chest radiograph show abnormalities such as cardiomegaly, atrial enlargement and pulmonary venous congestion. On echocardiography, consistent findings are evidence of restrictive filling, which include elevated mitral valve doppler diastolic filling velocity over atrial filling velocity ratios (E/A ratios), short mitral deceleration times, increased pulmonary vein atrial reversal velocity and duration, plus pulmonary vein atrial reversal duration greater than mitral A duration. Systolic function is typically preserved and ventricular hypertrophy is not prominent [33].

Following the identification of the underlying cause of the disease, currently used treatment options include heart failure management or cardiac transplantation, while diuretics are used to regulate volume overload [1]. Diuretics serve to treat venous congestion in both pulmonary and systemic circulation. They can reduce ventricular filling pressures if extensively used in patients with restrictive diseases, leading to decreased cardiac output, fatigue and lightheadedness, with signs of hypotension and hypoperfusion. Digoxin may be used with caution as it is potentially arrhythmogenic, particularly in patients affected by amyloidosis. Sinus rhythm must be maintained and, for this purpose, medications such as amiodarone are needed. Advanced conduction-system diseases need to be treated with the implantation of a pacemaker and, in cardiac sarcoidosis, malignant ventricular arrhythmias may require automatic implantable defibrillators or antitachycardia devices. As there is an increased propensity for thrombus to form in the atrial appendage, with the subsequent risk of embolic complications, anticoagulation with warfarin is recommended. Cardiac transplantation can be considered in patients with idiopathic or familiar RCM and refractory symptoms [8].

In pediatric patients affected by RCM, poor outcomes and limited transplant-free survivals have been reported [34]. No medical therapies have shown to clearly improve outcomes in RCM children and therapies are mainly symptom-based. Moreover, children affected by RCM are at increased risk of thromboembolic events and, therefore, the use of anticoagulants is generally warranted. If systolic dysfunction occurs during the progression of the disease, the use of angiotensin converting enzyme inhibitors may be considered. β-blockers have been proposed in cases of ischemia at higher heart rates based on analysis of the ST-segment on electrocardiogram or Holter. Cardiac defibrillators may also be considered in patients with ischemia, unexplained syncope or ventricular tachycardia [33].

1.2 Filamin-C

Filamins are actin-crosslinking proteins capable of binding and precipitating actin filaments. There are three filamin isoforms: filamin A, filamin B and filamin C. Filamins interact with different proteins and are involved in multiple cellular processes such as cell-cell and cell-matrix adhesion, mechanoprotection, actin remodeling and numerous intracellular signaling pathways [35].

The *FLNC* gene is located on chromosome 7q32.1 and consists of approximately 29.5 kb of genomic DNA, containing 48 coding exons [36]. Filamin-C (FLNC) is a 290.8 kDa protein, composed of 2725 amino acids and encoded by the *FLNC* gene and is also known as *actin-binding-like protein* (ABLP) or *filamin-2* (FLN2) [37]. This protein consists of an N-terminal actin-binding domain followed by 24 immunoglobulin-like repeats with two intervening calpain-sensitive hinges separating domains 15 to 16 (hinge 1) and domains 23 to 24 (hinge 2). FLNC can form homodimers via self-association through domain 24, resulting in a Y-shaped molecule connecting actin filaments. Calpain cleaves off the dimerization domain to regulate the mobility of the subunits [36], [38]. The protein is structurally very similar to its other isoforms except for an insertion of 20 AA in domain 20. Moreover, its hinge 1 is spliced out during myogenesis [36].

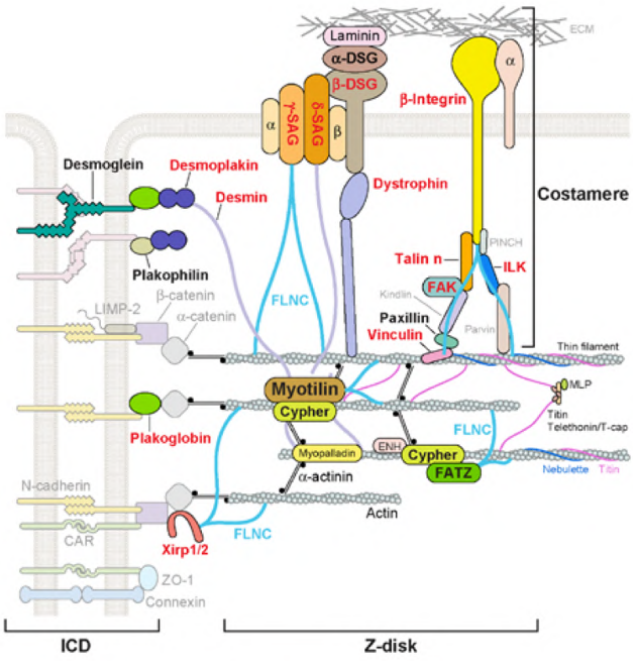

Figure 3. **Interactions of FLNC in the cell.** Filamin-C is localized at costameres that couple the sarcomere to the lateral sarcolemma of cardiomyocytes and to the extracellular matrix. Moreover, it directly interacts with components of the *fascia adherens*, therefore allowing the attachment of Z-disc components to the intercalated disks. Adapted from [39].

FLNC is expressed in skeletal and heart muscle: in the sarcomere, FLNC is responsible for cross-linking actin in the Z-disc region and additionally binds myotilin,

calsarcins (FATZ/myozenin), myopodin and Xin actin-binding repeat proteins (XIRPs); at the sarcolemma, the protein scaffolds a range of different structural and signaling proteins, interacting with *e.g.* sarcoglycans γ and δ, which are components of the distroglycan complex [40] (*Figure 2*).

The precise function of FLNC is yet to be understood. As it is mainly localized in striated muscle, its functions are likely associated with the sarcomere and mechanical sensing or stabilization. One plausible function of FLNC is serving as a mediator between membrane and sarcomere, since it is found both in subsarcolemmal regions and at Z-discs.

In skeletal muscle, FLNC is found at sites of formation of skeletal myopathies, and alterations in its subcellular localization have been exhibited in several muscular dystrophies such as myofibrillar myopathies (MFMs). MFMs are a group of progressive, devastating hereditary skeletal and cardiac muscular dystrophies, which are often inherited in an autosomal-dominant fashion and mainly caused by mutations in *BAG3*, *CRYAB*, *DES*, *DNAJB6*, *FHL1*, *LDB3*, *MYOT* and *FLNC* [1], [40]. These genes encode for proteins that have an essential role in cellular muscle homeostasis. Proteins linked to MFM are normally associated with Z-discs, where the linking of sarcomeres for the formation of myofibrils occurs and resistance to filament sliding is provided. Genetic mutations that cause MFM lead to the formation of protein clumps in muscle fibers, therefore disrupting sarcomeres and diminishing fiber strength [41]. Signs and symptoms of MFM vary among individuals, usually depending on the underlying genetic cause. The disorder is characterized by the development of muscle weakness and it manifests mostly in mid-adulthood, even though features of the condition can appear anytime between infancy and late adulthood. Distal muscles (hands and feet) are often the first affected. Nevertheless, individuals can develop muscle weakness in proximal muscles or throughout their body. Weakness in facial muscle can cause difficulties in swallowing and speaking. MFMs can also show the weakening of heart muscle, myalgia, peripheral neuropathy and respiratory failure. Joint stiffness and scoliosis are among the skeletal problems which are manifested; cataracts rarely develop [41].

Mutations in the *FLNC* gene often lead to filaminopathies, which are part of the spectrum of MFMs [42]. Three distinct types of filaminopathies have been identified. The first type is referred to as MFM-type FLNC myopathy. It is associated with mutations found in various locations around the FLNC rod domain and results in diseases causing loss of myofibrils and filamentous intracellular aggregates of myocyte proteins: desmin, dystrophin and sarcoglycans [43]. In addition, it is characterized by progressive muscle weakness, predominantly proximal. Biopsies from muscles of patients with aggregation-causing *FLNC* mutations show disintegrated myofibrils and desmin-positive protein aggregates forming within muscle fibers. Muscle weakness in MFM-type FLNC myopathy mostly starts when patients are between 24 to 60 years old. Initial signs of the disease include proximal muscle weakness, impairing uphill and upstairs walking. Both distal and proximal leg and arm muscles are progressively damaged in the course of the illness. Moreover, associated cardiac and respiratory muscle involvement contribute to reduced life expectancy. As a

matter of fact, cardiac abnormalities including conduction blocks, left ventricular hypertrophy and diastolic dysfunction were detected in patients affected by this filaminopathy variant [44].

The second type of filaminopathy (distal FLNC myopathy) is associated with mutations in the actin-binding domain of the protein and results in disease variants initially characterized by weakness and wasting of distal muscles. Muscle biopsies from patients affected by this filaminopathy variant show non-specific myopathic abnormalities without MFM pathology [44]. Distal FLNC myopathy usually develops in the third decade of life. Firstly, intrinsic hand muscles are affected and the strength in grip is reduced. Leg muscle weakness causing difficulties in running and jumping follow the progression of the disease. Cardiomyopathy signs were reported in some patients, while respiratory insufficiency is not associated with this particular variant [44]. A third, intermediate filaminopathy phenotype affecting distal muscles and the upper and lower limbs has been described, where no desmin-positive protein aggregates were detected [44].

Mutations in *FLNC* were originally reported to cause MFM, while their cardiac involvement was noted but yet not studied extensively. Recent reports show instead the involvement of the gene in a spectrum of cardiomyopathies which include RCM, HCM and dilated cardiomyopathy (DCM) where arrhythmias, cardiac conduction disease and SCD were also reported [43]. The phenotypic spectrum associated with the different variants is particularly interesting as it suggests that they either act through divergent and tissue-specific manners or that they are modified by other genetic factors present in the given family [45]. A correlation between the subtype of cardiomyopathy and the nature of the disease-causing variant was underlined [46].

FLNC mutations causing cardiac phenotypes without affecting the skeletal muscle were described in patients affected by HCM and DCM [47], [48]. A truncating mutation in the dimerization domain of FLNC was found in patients from diverse ethnical origins, indicating that this alteration marks a mutational hotspot [44]. The filaminopathy-associated truncating mutation, p.W2710X, is unique for two reasons: it is the first-ever reported *FLNC* mutation causative for MFM and HCM and, in addition, it is the first mutation in a dimerization domain shared by all filamins [44], [49]. *Table 3* lists known *FLNC* variants which are associated with RCM.

Table 3. **FLNC variants associated with RCM.** The following table represents the state of the art on known FLNC variants causative for RCM. Adapted from [9].

Gene mutation	Protein mutation	Mutation type	Exon	Reference
c.6893C>T	p.Pro2298Leu	Missense	41	[50]
c.7688A>G	p.Tyr2563Cys	Missense	47	[50]
c.4871C>T	p.Ser1624Leu	Missense	29	[51]
c.6478A>T	p.Ile2160Phe	Missense	40	[51]
c.6889G>A	p.Val2297Met	Missense	41	[45]
c.3548C>T	p.Ala1183Leu	Missense	26	[52]

c.3557C>T	p.Ala1186Val	Missense	26	[52], [53]
c.6902C>T	p.Pro2301Leu	Missense	41	[54]
c.6451G>A	p.Gly2151Ser	Missense	40	[54]
c.8129G>A	p.Trp2710*	Missense	48	[55]
c.4636G>A	p.Gly1546Ser	Missense	28	[56]
c.6397C>T	p.Arg2133Cys	Missense	40	[57]
c.7177C>T	p.Pro2393Ser	Missense	44	[57]
c.3557C>T	p.Ala1186Val	Missense	26	[53]
c.2265+4del	-	Splicing	14	[53]
c.4916G>A	p.Cys1639Tyr	Missense	28	[53]
c.7942G>T	p.Ala2648Ser	Missense	47	[53]
c.1322G>T	p.Arg441Ile	Missense	8	[53]

RCM phenotype was identified in patients harboring the p.V2297M mutation, where FLNC displayed diminished sarcomeric localization. The mis-localization was linked neither to aggregation as reported for HCM nor to altered actin-binding capability; it was rather hypothesized that it is a result of altered interactions between mutant FLNC with additional sarcomeric components [45]. Protein aggregation was detected in a family carrying the missense mutations p.R2133C and p.P2393C [57]. Schubert *et al.* also reported a missense mutation in families affected by RCM: the mutation p.P2298L resulted in FLNC protein aggregates with co-localized actin aggregates, causing the weakening of myofibers [50]. It was seen that the pathogenic myofibrillar myopathy-causing mutation in the rod of *FLNC* promotes misfolding of affected immunoglobulin-like domain, inducing aggregation of the mutant protein. Muscle fibers can compensate for this effect for long periods of time through mechanisms like protein degradation strategies. However, proteasomal and autophagic degradation pathways were shown to decline in relation to oxidative stress and mitochondrial alterations, therefore attenuating protection mechanisms. As a result, the accumulation of mutated FLNC and other proteins was triggered, resulting in a disturbance of Z-disc protein homeostasis and focal myofibril destruction [40].

In a study conducted by Begay *et al*. and in line with the findings of Ortiz-Genga *et al.*, the analysis of tissue carrying a *FLNC* truncation showed no protein aggregates as in MFM, but instead Z-discs abnormalities, altered distribution of junction proteins and subepicardial fibrofatty infiltration. They theorized a haploinsufficiency model of *FLNC*, in which the altered production of the protein may disrupt the normal functions of cross-linking actin filaments, which connect the subsarcolemmal sarcomere Z-discs to the cell membrane and integrins as well as actin to cell-cell adhesion junctions in intercalated disks. This results in an interference with the desmosomal/cell-cell junction pathway and manifests as an arrhythmogenic cardiomyopathy [43], [58].

Other reported FLNC mutations causative for RCM were all characterized by similar phenotypes. Heavily dilated atria with normal ventricular dimension and systolic function was reported for the mutation p.Y2563C [50]. Normal left ventricular wall thickness and systolic

function with various degrees of diastolic dysfunction, pulmonary hypertension and left biatrial enlargement were described in RCM patients with novel missense mutations p.S1624L and p.I2160F [42]. p.S1624L was not the only mutation found in Ig-like domain 14; Sanoja *et al.* also reported an RCM phenotype associated with the mutation p.G1546S [56]. Similar phenotypic findings leading to the diagnosis of RCM were encountered in adults carrying the missense mutations p.P2301L and p.G2151S [54].

Diverse *FLNC* mutations were found in pediatric RCM patients. Mutation p.A1186V was identified in patients up to three years old affected by muscle weakness, atrial enlargement, cardiac valves deficiencies and general heart failure [52], [53]. Mitral and tricuspid regurgitation were also observed in association with missense mutations p.C1639Y, p.A2648S and the splicing mutation c.2265+4del, while atrial and left ventricle enlargement were detected in patients carrying the mutation p.R441I [53]. Finally, fiber splitting in combination with necrotic fibers and disrupted myofibril organization was reported for the mutation p.A1183L [52].

To better understand the role of FLNC in muscle, its ablation was also investigated in a mouse model. *FLNC* knock out shows a severe morphological phenotype both *in vitro* and *in vivo*. It was reported that cells start differentiation normally, but fusion slows progressively and the expression of transcriptional markers of differentiation plateaus prematurely, indicating a block of later stages of differentiation. In addition, myotubes collapse to form large multinucleated “balls” instead of maintaining an elongated tube morphology. *In vivo*, FLNC-deficient mice showed few, short and rounded fibers with centrally located nuclei and disorganized sarcomeric structure. Even though mice were born alive, they showed difficulty in breathing and moving and died quickly due to respiratory failure [59]. In regard to heart muscle, conditional loss of FLNC resulted in fetal death in embryonic cardiomyocytes. *FLNC* knock out mice developed rapid and fulminant dilated cardiomyopathy within two weeks, confirming that the loss of the protein is catastrophic for heart function [39].

Overall, filamins interact with more than 90 cellular proteins with a broad range of functions including cell to cell matrix connections, machanoprotection and various signaling networks. Recent studies show evidence of FLNC as a key protein involved in myofibril repair for skeletal and cardiac muscle cells, suggesting that FLNC may be more of a mobile signaling core rather than a structural and static protein [60]. Moreover, the early onset of RCM in several families suggests the importance of its expression and its role in heart development and function. Nowadays, cardiomyopathies caused by *FLNC* mutations present a challenge in the extrapolation of correlations between genotype and phenotype based on variant position [50].

1.3 Human induced pluripotent stem cells

Cloning and nuclear transfer stay at the root of induced pluripotency in differentiated cells. With the generation of the first experimentally cloned animal in 1895, Hens Dreish

brought up the concept of totipotency, pluripotency and multipotency to life sciences [61]. Totipotency is defined as the ability of cells to differentiate into all types of cells; pluripotency is the ability of cells to differentiate into all types of intra-embryonic cells, while multipotency is the ability to differentiate into a limited number of cell types [62]. The use of nuclear transfer was published in 1938 by Spemann, whereas the first successful nuclear transfer into enucleated eggs was performed using tadpoles by Briggs and King in 1952 [63], [64]. In their experiments, a cloned frog could not be produced when using the nuclei from a stage later than the tail bud. They concluded that, when the cell fates were committed to a specific lineage during development, the nuclei of differentiated cells lost the information of other types of cells [64]. However, almost 10 years later, Sir John Gurdon obtained tadpoles by transplanting the nuclei of small intestinal epithelial cells of adult frogs into enucleated unfertilized eggs, therefore demonstrating that even nuclei of adult frogs maintained all the information necessary for the development of a tadpole [65]. Further results such as the famous cloned sheep Dolly, in 1997, provided important knowledge on the fact that information contained in the nuclei is not irreversibly deleted when cells commit to a specific fate during development. Somatic cells can indeed be converted into other kinds of cells even after differentiation and development [62], [66].

Pluripotent embryonal carcinoma cells (ECCs) were isolated from teratocarcinoma in 1964 and were able to differentiate into various types of cells *in vitro* [67]. When fused with differentiated cells, ECCs could reprogram them toward a pluripotent state. However, they were useless for genome engineering due to their incompetence for germ line contribution and frequent teratoma formation [62], [68]. In 1981, embryonic stem cells (ESCs) were established from mouse blastocysts and started being used for genetic engineering and biological applications [69]. Finally, embryonic germ cells (EGCs) were first isolated in 1992 from primordial germ cells (PGCs) [70]. All these cell lines had the ability to maintain a normal karyotype and differentiate into all types of somatic cells after blastocyst injection. Moreover, ECCs, ESCs and EGCs could reprogram the nuclei of somatic cells towards a pluripotent state; this indicated that not only oocytes, but also pluripotent cells are able to reprogram nuclei toward the pluripotent state and possess the so-called *reprogramming factors* [71]. As a matter of fact, the first successful reprogramming of differentiated human somatic cells occurred in 2007, when Takahashi *et al.* demonstrated the generation of iPSCs from adult human dermal fibroblasts through the expression of the factors *OCT3/4*, *SOX2*, *cMyc* and *KLF4*. Such cells were similar to ESCs in their morphology, proliferation, surface antigens, gene expression, telomerase activity and epigenetic status of pluripotent cell-specific genes. In addition, they could differentiate into cell types of all three germ layers *in vitro* and in teratomas [71]. Based on this information, Tanabe *et al.* hypothesized, in 2014, that ESCs fate could also be induced in somatic cells. They speculated that differentiated cells could be converted into an ESCs fate through the overexpression of several important factors [62]. The set of reprogramming factors can vary depending on the donor cell type, as specific cell types might endogenously express some of them [72]. Nowadays, hiPSCs can be generated directly from the primary cells of mutation carriers by direct reprogramming, but mutations

can also be induced using genome editing techniques such as CRISPR/Cas9 or transcription activator-like effector nucleases (TALENs). Furthermore, hiPSCs can be modified by either the overexpression or the decreased expression of specific mutant proteins through *e.g.* RNA interference [72].

The discovery that human dermal fibroblasts expressing transcription factors can be reprogrammed to a pluripotent state *in vitro* made new possibilities in research arise [62] [71]. iPSC technology allowed to overcome the ethical concerns surrounding the use of human embryonic stem cells (hESCs) and, nowadays, the study of genetic diseases *in vitro* and disease modeling are largely available for scientists. Most importantly, cells can be reprogrammed from patients, and therefore share the same genetic information for personalized medicine approaches. In the cardiovascular field, iPSCs represent an attractive tool due to the limited availability of human cardiac tissue. The differentiation of hiPSCs into cardiomyocytes (CMs) is a versatile resource for research, as hiPSCs carrying disease-specific mutations can be used to observe the related phenotypes and compare them to healthy or isogenic controls [73], [74].

1.3.1 hiPSC-derived cardiomyocytes

Primary human cardiomyocytes are hard to obtain due to invasive cardiac biopsies, difficulties in the dissociation process to single cells and poor long-term survival in culture. Currently, murine, atrial cardiomyocytes-related HL-1 cell line is the only contracting CM cell line available. On the other hand, while primary CMs isolated from rodent hearts differ from human ones in *e.g.* electrophysiology [75]. For this reason, patient-specific hiPSC-CM technology represents a powerful tool for basic research and clinical and translational applications such as disease modeling and drug discovery.

Cardiogenesis is a complex cellular and molecular process *in vivo*, where a large spectrum of transcription factors, growth factors and microRNAs are time-dependently expressed and regulated. Zhang *et al.* originally described the differentiation of CMs from hiPSCs. Early efforts in CM differentiation employed protocols using embryoid bodies (EBs) formed in suspension, however, the method was still relatively inefficient [76]. In time, several efficient hiPSC monolayer-based CM differentiation protocols were developed [77], [78]. Discoveries from developmental biology made it possible to recognize recombinant growth factors that can be used to improve the efficiency of *in vitro* differentiation of CMs such as *BMP4*. Moreover, the modulation of the *Wnt* pathway by small molecules like CHIR99021 and IWP2 has made it possible to increase CM differentiation up to 90%. Further accumulation of CMs can be obtained through metabolic selection by glucose depletion in combination with lactate supplementation [72], [79].

Methods for the functional analysis of hiPSC-CMs include histochemical and molecular methods like RNA-seq or proteomics, but also specific techniques for the *in vitro* analysis of their electrophysiological and contractile properties. Patch clamping and multiple electrode arrays can be used for the analysis of monolayers, while the application of Ca^{2+}-

specific fluorescence dyes such as Indo1 allows for the analysis of Ca^{2+} transients. Voltage-sensitive fluorescence dyes can also be used for the study of electrophysiological properties. On the other hand, in order to analyze the contractile properties of hiPSC-CMs, microscopic traction force measurements and atomic force microscopy can be used [72].

1.3.2 Disease modeling using hiPSCs-CMs

The functional knowledge about mutations associated with cardiomyopathies is limited due to the lack of adequate models. hiPSCs carrying specific mutations are a promising alternative to time-consuming, expensive and nonetheless challenging animal models. As a matter of fact, there are some cases in which human cardiomyopathies cannot be modeled though animal models because of species differences. Therefore, hiPSC-CMs represent the only available human cellular model for the direct functional analysis of specific genetic cardiomyopathies. During the last decade, impressive progress in the reprogramming, differentiation procedure and genome editing techniques such as CRISPR/Cas9 allowed for the development of defined cardiomyocyte models and their isogenic control lines [72].

To this day, hiPSC-CMs have been used for (i) the characterization of genetic variants of unknown significance, (ii) analyses of molecular pathomechanisms and (iii) the development of specific therapies. However, difficulties in modeling cellular and molecular crosstalk between inflammatory cells, fibroblasts, myoblasts and CMs are encountered when using hiPSCs. Limitations in the use of hiPSC-CMs include (i) genomic instability, (ii) heterogeneity of hiPSC-CMs and (iii) cellular, molecular and functional differences of adult ventricular CMs and hiPSC-CMs [72].

For several genes whose mutations have been associated with cardiomyopathies, different iPSC lines have already been generated [72]. On the other hand, there are still no available lines for rarer genes also due to the high heterogeneity of inherited cardiomyopathies. In the future, it will be important to continue generating novel iPSCs lines to be able to compare molecular differences and commonalities, which lead to the development of non-ischemic cardiomyopathies.

1.4 Aim

The position of the heterozygous mutation found in a young patient at the Boston Children's Hospital (p.Glu2472_Asn2473delAsp) is very close to a previously described FLNC mutational hotspot and might therefore cause a similar pathology. It has been previously reported that this variant leads to a partial disturbance of the secondary structure of the dimerization domain, which results in massive protein aggregation in muscle tissue of affected patients as well as in overexpression studies using cell culture models [40], [49], [80]. A similar pathology was expected for our novel *FLNC* mutation, since the dimerization domain of the protein is also affected. Nevertheless, it was not clear whether the pathomechanism is defined by expression of a misfolded protein, overstraining the protein

degradation systems in the cell, or the generation of a toxic gain-of function protein which alters ligand binding properties. The modeling of this novel *FLNC* mutation helped to elucidate the pathomechanism, allowing testing of novel therapeutic strategies for RCM and ultimately helping with the design of a personalized medicine for the patient carrying this mutation.

1.5 Relevance

Cardiomyopathies are myocardial disorders causing heart failure or sudden cardiac death. Even though they can be treated pharmacologically to soften pathology, they do not target the genetic cause of the disease. Many patients affected by end-stage cardiomyopathy are therefore in need of a heart transplant. For the RCM case studied in this project, sarcomere-related protein aggregation can cause heart wall stiffness and damage in ventricular filling, resulting in an impaired diastolic phase of the cardiac cycle that can lead to significant dysfunctions in the long term, if left untreated.

Because limited therapeutic approaches for RCM have been described, the technology of hiPSCs represents a very promising resource especially for pediatric patients. Thus, it is of extreme importance to continue investigating and implementing such innovative strategies, as they are an efficient tool to better understand diseases and they allow for the development of personalized medicines.

What we expected to obtain was a model resembling aspects of the RCM phenotype found in a young patient who was positively identified with a novel mutation in *FLNC*. Successful establishment of this disease model represents the key for studying this specific form of RCM and for the development of a tailored treatment not just to manage RCM, but to cure it.

2 Methods

WTC-11 (WTC) cell lines were originally developed by the Coriell Institute (catalogue #GM25256). Cells were extracted from a skin biopsy of a 30 years old male Japanese characterized by an apparently normal karyotype [81].

WTC-Cas9 cells belong to a genome-edited line where the doxycycline-inducible SpCas9 was inserted into the AAVS1 safe harbor *locus* of the WTC-11 hiPSCs. This cell line is heterozygous for the SpCas9 allele and, therefore, an additional allele is available for further knock-ins. The line was created by Dr. Xujie Liu using the plasmids pAAVS1-PDi-CRISPRn (*Addgene* #73500) and pSpCas9(BB)-2A-GFP (PX458) (*Addgene* #48138).

Mutant cell lines were generated by Dr. Maksymilian Prondzynski by inducing Cas9 expression through doxycycline supplementation, followed by transfection using the *4D-Nucleofector*™ System (*Lonza*) and the single guide RNA (sgRNA).

For the purposes of this thesis, disease modeling was carried out using WTC-Cas9 cells and both heterozygous and homozygous clones carrying the mutation (see *Appendix A*). In particular, two clones were selected: FLNC 28-12 and FLNC C1-C3, respectively.

2.1 Maintenance of WTC-Cas9 and FLNC clones cell lines

Cryotubes containing the cell lines were routinely collected from liquid nitrogen stores and thawed at 37°C before seeding them for expansion. The used plates were coated with 0.5% Geltrex LDEV-Free, Reduced Growth Factor Basement Membrane Matrix (*Thermo Fisher* #A1413302) in PBS (*Thermo Fisher* #10010049) and incubated at 37°C at least half an hour before plating the cells.

HiPSCs were stored in aliquots of one million in mFreSR cell freezing medium (*StemCell Technologies* #05855) and resuspended in E8 medium (*Thermo Fisher* #A1517001) supplemented with Y-27632 (*R&D* #1254, 10 μM) after thawing. One passage is needed before starting differentiation experiments with hiPSCs. hiPSC-CMs are kept stored in aliquots of one million in *STEMdiff*™ Cardiomyocyte Freezing Medium (*StemCell Technologies* #05030) and resuspended in RPMI 1640 Medium, GlutaMAX Supplement (*Thermo Fisher* #61870127) supplemented with B27 (minus insulin, *Thermo Fisher* #A1895601) after thawing.

Aliquots of both hiPSCs and differentiated hiPSC-CMs were frozen throughout the course of the experiments as a backup. Medium was first aspirated from cells, which were then incubated with Versene (*Thermo Fisher* #1540066) for up to seven minutes at 37°C. Standard culture medium was used to block the reaction. Cells were counted and centrifuged before gently resuspend them in pre-warmed mFreSR or *STEMdiff*™ cell freezing medium. Finally, cells were transferred to cryotubes and placed in a cooling rack at -80°C overnight before storing them in the liquid nitrogen reserves at -150°C.

2.2 Cardiomyocyte differentiation of hiPSCs

Once the expanded cells in 6-well-plates reached the ideal confluency of approximately 60-70%, 2D differentiation experiments were carried out. Cells were detached from the wells with Versene and resuspended in E8 + Y-27632. 0.5% Geltrex-coated, 12-wells plates were used for 2D differentiation. Plates were prepared in advance and incubated at 37°C overnight before use. The following subchapters will describe the culture routine used to achieve fully differentiated cardiomyocytes, which is schematically represented in the timeline from *Figure 4*.

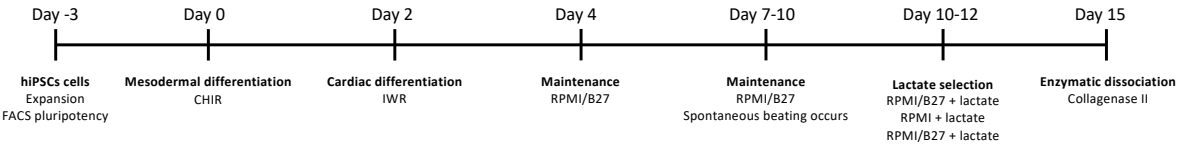

Figure 4. **2D differentiation timeline.** The timeline shows the most important steps in the culture of iPSC to achieve a monolayer of beating CMs.

2.2.1 2D differentiation

Pre-warmed, 0.5% Geltrex-coated 12-well-plates were seeded with 10^5 cells per well. Cells were resuspended in E8 + Y-27632 and kept in culture for 24 hours before performing a full medium change to E8; E8 was used to keep them in culture for the following 48 hours until desired confluency for differentiation start was reached.

A full medium change to RPMI/B27 supplemented with CHIR909921 (*StemCell Technologies* #72054, 7 µM) marked the beginning of mesodermal differentiation (day 0-1). After 48 hours of culture, cardiac differentiation was induced with a full medium change to RPMI/B27 supplemented with Y-27632 and IWR1-endo (*StemCell Technologies* #72564, 10 mM) (day 2-3). Starting from day 4, cells were maintained in culture using RPMI/B27. Spontaneous beating of differentiated cardiomyocytes occurred between day 7 and 10 in culture.

2.2.2 Lactate selection

Lactate selection was used as a purification method to enrich hiPSC-CMs. The approach is based on the biochemical differences in lactate and glucose metabolism between CMs and non-CMs. Even though mammalians use glucose as their main energy source, CMs are capable of energy production from sources such as lactate or fatty acids [82]. Lactate selection was performed over the period of three days from day 10 of differentiation. Medium was switched to RPMI/B27 supplemented with 5 mM lactate (*Sigma Aldrich*, #L7900) for 24h; it was then changed to RPMI + 5 mM lactate for 24h and back to RPMI/B27 + 5 mM lactate for the remaining 24h.

2.2.3 Enzymatic dissociation

Collagenase II was used to dissociate differentiated cardiomyocytes to utilize them for downstream applications or to freeze them as backup. The collagenase solution was prepared with 1 mg/ml collagenase II (200 u/mg; *Thermo Fisher*, #NC9693955) in HBSS (without Ca^{2+}, *Sigma Aldrich* #55021C) supplemented with 1 mM sterile filtered HEPES (pH 7.4, *Sigma Aldrich* #H4034) + 10 µM Y-27632 (1:1000) + 30 µM N-benzyl-p-toulene sulphonamide (BTS; *Sigma Aldrich*, #203895, 1:1000). Medium was aspirated from the selected wells and replaced with pre-warmed HBSS without Ca^{2+}. HBSS was then aspirated and replaced with the pre-warmed collagenase solution before one-hour incubation at 37°C. The reaction was stopped by using a blocking buffer composed of RPMI supplemented with 6 µL DNase per ml (*Sigma Aldrich*, #D8764-150KU). Cells were transferred to 50 ml tubes and centrifuged for 10 minutes at 100 $\vec{g}$. Lastly, pellets were resuspended in RPMI.

2.3 Quality control

2.3.1 Genotyping using polymerase chain reaction

Polymerase chain reaction (PCR) was consistently used throughout the project as a quality control to verify the genotype of the CRISPR/Cas9-edited hiPSC-CMs and their isogenic control. For this purpose, the *DNeasy® Blood & Tissue Kit* (*Qiagen* #69504) and the *QIAquick PCR Purification Kit* (*Qiagen* #28104) were used. Sanger sequencing was performed by *Genewiz®* and results were implemented in the *SnapGene®* software for further analysis. The figure depicts the PCR conditions used to target the *locus* where the mutation was inserted (*Figure 5*). For this purpose, *PrimeSTAR HS DNA Polymerase, 5x PrimeSTAR Buffer and dNTPs,* (Takara *#R010B*) were used. Primer sequences were designed by Dr. Prondzynski and can be consulted in *Appendix B*.

Touchdown PCR		
98°C	10"	
*61°C	30"	11x
72°C	45"	
98°C	10"	
56°C	30"	24x
72°C	45"	
72°C	7 min	
4°C	∞	

Name	Primer bank number	TmeIt	Fragment
FLNC_for	26	62°C	666
FLNC_rev	27		

Figure 5. **FLNC PCR conditions.**

2.3.2 Off-target analysis

In order to avoid effects such as *e.g.* unintended point-mutations, deletions or insertions leading to non-specific genetic modifications, off-target analysis was performed. *Figure 6* depicts PCR conditions used for the three addressed off-targets. Primer sequences

were designed by Dr. Prondzynski and can be consulted in *Appendix B*. Off-targets will be referred to as *Off1*, *Off2* and *Off3*.

Touchdown PCR		
98°C	10"	11x
*63°C	30"	
72°C	45"	
98°C	10"	24x
58°C	30"	
72°C	45"	
72°C	7 min	
4°C	∞	

Name	Primer bank number	TmeIt	Fragment
FLNC_for_Off1_Deletion	1	62.4°C	359
FLNC_rev_Off1_Deletion	2		
FLNC_for_Off2_Deletion	3	63.5°C	350
FLNC_rev_Off2_Deletion	4		
FLNC_for_Off3_Deletion	5	63°C	503
FLNC_rev_Off3_Deletion	6		

Figure 6. **FLNC off-targets PCR conditions.**

2.3.3 Amplicon sequencing

PCR products, or amplicons, can be pooled and sequenced with high-throughput next-generation sequencing (NGS). As NGS-based targeted sequencing results in high coverage of a specific region of interest, amplicon sequencing can detect variants at very low levels and frequencies. Figure 7 depicts the PCR conditions and primers used for the analysis. Primer sequences were designed by Dr. Prondzynski and can be consulted in *Appendix B*. Amplicon sequencing was performed by *Genewiz®.*

Touchdown PCR		
98°C	10"	11x
*65°C	30"	
72°C	30"	
98°C	10"	24x
60°C	30"	
72°C	30"	
72°C	7 min	
4°C	∞	

Name	Primer bank number	TmeIt	Fragment
FLNC_for_Amplicon	34	80°C	411
FLNC_rev_Amplicon	35		

Figure 7. **FLNC amplicon PCR conditions.**

2.3.4 Gel electrophoresis

Gel electrophoresis was performed to visualize the PCR products. In order to visualize the targeted fragments, a 2% agarose (*Apex*, #9012-36-6) gel in tris-acetate-EDTA (TAE) buffer (*Thermo Scientific*, #28354) was casted. Samples were prepared by mixing 10 µl of raw PCR product with 3 µl of (purple) 6X gel loading dye (*New England Biolabs*, #B7024S); as a reference, the *NEB* 100 bp ladder (*New England Biolabs*, #N3231L) was used. Loaded wells were run for one hour at 150V.

2.3.5 Karyotyping

Karyotyping analyzes chromosomes in a sample of cells, providing a genome-wide snapshot and therefore helping in the identification of genetic problems causing a disorder or disease. The *nCounter®* Human Karyotype Panel from *NanoString Technologies®* allows

to accurately quantify chromosome number and detect aneuploidy, the existence of either more or less than two chromosomes in a diploid genome. Karyotyping is an important step for quality control in disease modeling, as chromosomal aberrations occur in *in vitro* cultures and may alter the biological properties of cells in culture and possibly compromise experimental results [83]. DNA extracted from samples was used for this analysis.

2.4 Fluorescence-activated cell sorting

Fluorescence-activated cell sorting (FACS) analysis was performed using the *BD LSRFortessa™*. FACS working solution was prepared using PBS, 5% FCS, 0.5% saponin (*Sigma Aldrich* #47036) and 0.05% sodium azide (*Sigma Aldrich* #S2002) and stored at 4°C until further use. The preparation of hiPSCs and CMs followed the procedure described in a previously published protocol [84]. Cells were collected in FACS-tubes, 3 ml of PBS were added on top and the aliquots were centrifuged at 400 $\vec{g}$ at 4°C for five minutes; this washing step was performed after every change of reagent. After decanting the supernatant, cells were fixed using 200 µl of methanol (stored at -20°C) for ten minutes. Cells were permeabilized overnight in 500 µl working solution at 4°C.

2.4.1 FACS analysis for pluripotency markers

The isotype (REA) control-PE (*Miltenyi Biotec* #130-104-613, 1:50) and human anti-SSEA-4 (*Miltenyi Biotec* #130-098-347, 1:11) staining were diluted in 100 µl working solution per sample. Samples were then incubated for 45 minutes to one hour at 4°C in the dark. Finally, samples were resuspended in 200 µl of PBS and stored at 4°C until FACS analysis.

2.4.2 FACS analysis for differentiated cardiomyocytes

The efficiency of differentiation was evaluated through FACS. The isotype (REA) control-PE and the anti-cTnT-PE (*Miltenyi Biotec* #130-106-688, 1:10) staining were diluted in 100 µl working solution per sample. Samples were then incubated for 45 minutes to one hour at 4°C in the dark. Finally, samples were resuspended in 200 µl of PBS and stored at 4°C until FACS analysis.

2.5 Disease modeling with hiPSC-derived cardiomyocytes

2.5.1 2D disease modeling

Differentiated hiPSC-CMs were used for several downstream applications. 2D disease modeling was carried out by plating cells in different densities on both 12-well-plates and 96-well-plates. 12-well-plates were seeded with $4.4x10^5$ cells/well, while three different cell densities were used for 96-well-plates: 10^3, $5x10^3$ and $2x10^4$ cells per well. The chosen timepoints for experiments were day 7 in culture and day 30.

CMs from 7 and 30 days *in vitro* (div) were dissociated with *Accutase* (*StemCell Technologies*, #07920) and collected in 1.5 ml tubes. After centrifugation for 10 minutes at 200 $\vec{g}$, pellets were either snap frozen or resuspended in RPMI for further experiments.

2.5.1.1 Fixation of 2D disease modeling plates

For their fixation, 96-well-plates were washed in PBS and subsequently incubated for 10 minutes with 4% paraformaldehyde (PFA, *Electron Microscopy Sciences* #30525-89-4) in PBS. An additional PBS washing step was required antibody incubation for immunofluorescence experiments.

2.5.2 Generation of EHTs

The generation of engineered heart tissues was performed following the steps previously published in Breckwoldt *et al.* as a guideline, and is briefly described in the following section [84].

The generation of EHTs relies on the fabrication of agarose casting molds and fibrin gels with single-cell suspension around flexible PDMS posts (*Figure 8)*. Slots for EHTs were prepared with 2% agarose (*Invitrogen* #15510-027) in PBS (approximately 1.5 ml/well) in a 24-well-plate. During the polymerization time of the molds, a master mix was prepared: $0.5x10^6$ cells/EHT were mixed with RPMI + B27 + Y-27632, 10% Matrigel (*BD Biosciences* #354234) and fibrinogen (*Sigma-Aldrich* #F8630, 200 mg/ml in 0.9% NaCl-solution) in solution with aprotinin (*Sigma-Aldrich* #A1153, 33 mg/ml in *aqua ad injectabilia*). 100 µl of master mix in one 3 µl thrombin aliquot (*Biopur* #BP11-10-1104, 100 U/ml in *aqua ad injectabilia*) were mixed and pipetted into the agarose-slot; the process was repeated for each mold. EHTs were incubated at 37°C for one hour before taking the PDMS posts out of the molds and transferring them to a new, 24-well-plate with 1.5 ml RPMI + B27 + insulin per well. During the first phases of the construction, when the gel solution is formed, PDMS posts have to be oriented in a parallel configuration, in order to apply an auxotonic load to the tissues, therefore facilitating the longitudinal alignment of the cardiomyocytes embedded in fibrin. The remodeling action of the resident cells causes the bending of PDMS and results in the shortening of the muscle strip. 10-15 days after, the first, spontaneous beating is expected to occur. PDMS posts further deflect due to beating and the force-producing capability of the tissue is assessed by the measurement of such deflection.

Contraction analysis is performed by an optogenetic approach and the ImageJ plugin *MUSCLEMOTION*, enabling the definition of disease-specific phenotypes on a functional level. For this purpose, 30 frames per second (fps) videos were taken systematically and analyzed to detect changes in contraction and observe the phenotype of the control EHTs compared to the mutants (a guide for the use of *MUSCLEMOTION* is available in *Appendix C*).

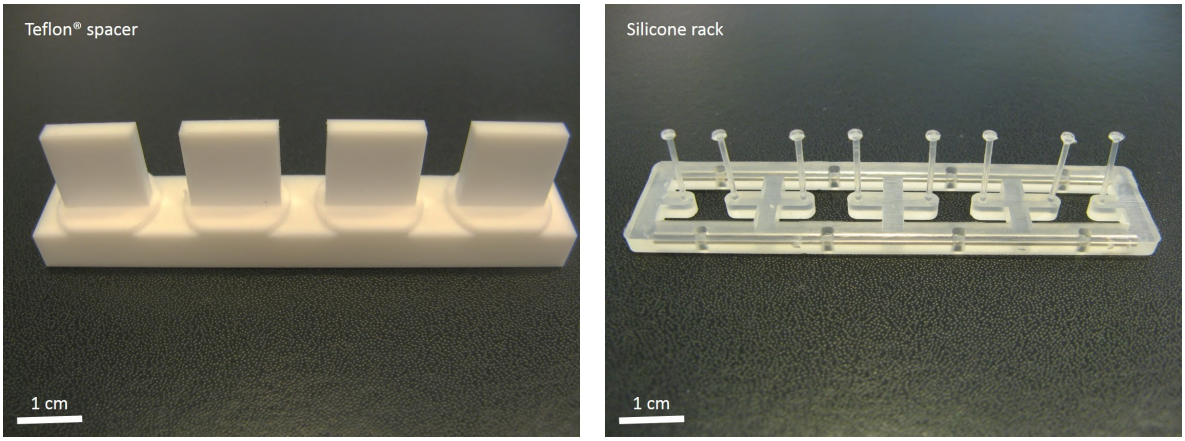

Figure 8. **EHT spacer molds and PDMS posts rack.** Depicted are the commercially available spacer molds and the posts rack used for the generation of EHTs in 24-well-plates. Scale bars are shown in the pictures. Adapted from [84].

EHTs were kept in culture and monitored for 30 days in RPMI medium supplemented with aprotinin (1:1000). After 30 div, EHTs were washed in PBS before incubating them for five minutes in RPMI without B27 and supplemented with 0.3% 2,3-butanedione 2-monoxime (BDM; *TCI*, #B0683). This step is necessary for the inhibition of chemical and motile activity and, therefore, for tissue relaxation. EHTs were then carefully taken off the posts, selected and placed into 2 ml tubes according to the planned experiments. EHTs used for molecular biology assays were snap frozen in liquid nitrogen and stored at -80°C.

2.5.2.1 Fixation of EHTs

The fixation of EHTs was performed by incubating them in 1 ml PFA. EHTs used for immunofluorescence experiments were incubated for 24 hours in 4% PFA and washed thoroughly in fresh PBS. Tissue was fixated in 1% PFA for 24 hours before undergoing sucrose protection for its preservation. The sucrose method is composed of three steps: one-hour incubation with 10% sucrose (*Sigma-Aldrich* #S0389) in distilled water and supplemented with 0.05% sodium azide which is then replaced by 20% sucrose solution for two hours and, finally, by 30% sucrose solution overnight. Lastly, EHTs were snap frozen in liquid nitrogen and stored at -80°C.

2.5.2.1.1 Cryosectioning of tissue

EHTs used for immunocytochemistry were thawed and mounted on disposable vinyl specimen molds. Enough tissue freezing medium (*GeneralDatal*, #TFM-5) to fill the mold was poured on top of each EHT and specimens were transferred for six hours at -80°C. After incubation, sections of tissue were cut using a cryostat microtome and mounted on glass slides. For fixation, slides were washed in PBS and incubated for 10 minutes in 3% PFA. Three washing steps in PBS were necessary before staining of samples.

2.5.3 Immunofluorescence

Immunofluorescence (IF) permeabilization buffer was prepared using 5% bovine serum albumin (BSA, *Sigma Aldrich* #A9647) and 0.1% Triton X-100 (*Sigma Aldrich* #T9284) in PBS. The following table summarizes the antibodies used for IF purposes (*Table 4*).

Antibodies were diluted in IF buffer in their respective dilutions. Incubation of primary antibodies was performed overnight at 4°C, while the incubation time of secondary antibodies was of one hour at room temperature. Direct stainings were added just 10 minutes before the end of secondary antibodies' incubation. Each step was followed by a PBS washing step. Samples used for IF experiments included iPSC and iPSC-CMs 96-well-plates and EHT tissues.

Table 4. **List of antibodies used for IF.** The following table displays the antibodies used for IF purposes. Both stainings used for iPSCs and iPSC-CMs are included.

Primary antibodies

Name	Species	Clone	Manufacturer	Product number	Dilution	Category
ACTN2	Mouse	Monoclonal	*Sigma Aldrich*	A7811	1:200	Heart, skeletal muscle
α-actinin	Goat	Polyclonal	*Santa Cruz*	SC-7454	1:400	Cytoskeleton
FLNC	Rabbit	Polyclonal	*Sigma Aldrich*	HPA006135	1:200	Heart, skeletal muscle
FLNC	Rabbit	Polyclonal	*Abcam*	AB244284	1:200	Heart, skeletal muscle
Ki-67	Mouse	Monoclonal	*Santa Cruz*	SC-23900	1:400	Cell proliferation
Oct4	Goat	Polyclonal	*Santa Cruz*	SC-8628	1:200	Pluripotency marker
Sox2	Goat	Polyclonal	*Santa Cruz*	SC-17320	1:200	Pluripotency marker
Vimentin	Rat	Monoclonal	*R&D Systems*	MAB2105	1:400	Intermediate filament

Secondary antibodies

Name	Species	Clone	Manufacturer	Product number	Dilution	Category
Alexa Fluor® 488	Rabbit	Polyclonal	*Thermo Fisher*	A11008	1:500	-
Alexa Fluor® 555	Mouse	Polyclonal	*Thermo Fisher*	A28180	1:500	-

Direct staining

Name	Manufacturer	Product number	Dilution	Category
Alexa Fluor® Phalloidin 488	*Thermo Fisher*	A12379	1:250	Cytoskeleton
Alexa Fluor® Phalloidin 647	*Thermo Fisher*	A22287	1:250	Cytoskeleton
Hoechst 33342	*Thermo Fisher*	H3570	1:50	Nuclei
SSEA-4	*Miltenyi Biotec*	130-098-347	1:11	Pluripotency marker

Wheat germ agglutinin	*Thermo Fisher*	W32466	1:250	Cell membrane

2.5.3.1 Immunocytochemistry of EHTs

Glass slides were washed in PBS and incubated in 0.25% Triton X-100 in PBS for 15 minutes. Three PBS washing steps of 15 minutes were necessary before blocking for 90 minutes with 10% FCS, 50 mM glycine (*GE Healthcare Life Sciences*, #17132301) and 0.05% Triton X-100 in PBS. The blocking buffer was replaced with primary antibodies in 5% FCS, 0.05% Triton X-100 in PBS overnight at 4°C. Three PBS washing steps of 15 minutes were performed before incubation with secondary antibodies or direct stainings in 5% FCS, 0.05% Triton X-100 in PBS for one hour at room temperature. Slides were washed once in PBS and post-fixed with 3% PFA in PBS for 10 minutes. The solution was thoroughly washed away with three PBS washing steps of 5 minutes. To seal glass slides, a couple of drops of the *Prolonged Diamond Antifade* mounting medium (*Invitrogen*, #P36961) were placed on top of the specimens and covered with a cover slip.

2.5.4 Image analysis

Image analysis of CMs was performed using *Fiji*. For the purposes of this thesis, both cell area and sarcomere disarray were measured.

2.5.4.1 Sarcomere disarray analysis

Sarcomere disarray analysis was performed as described by Prondzynski *et al.*, using confocal images that were stained for α-actinin 2 [85]. Three regions of interest (ROIs) in proximity to the borders of a single cell were selected. For each ROI, a segment in the range of 10 to 12 µm was drawn using the straight tool of the software; the drawn segment perpendicularly intersected up to six Z-discs of the sarcomere's structure. Values of the maxima along the *x* axis were recorded (*Figure 9*). The same steps were repeated after moving the segment in a parallel position with the scrolling tool. The length of the sarcomere was calculated by subtracting two subsequent maxima, while the disarray value was given by the ratio between the two. The standard deviation (SD) was calculated using the disarray values of each ROI.

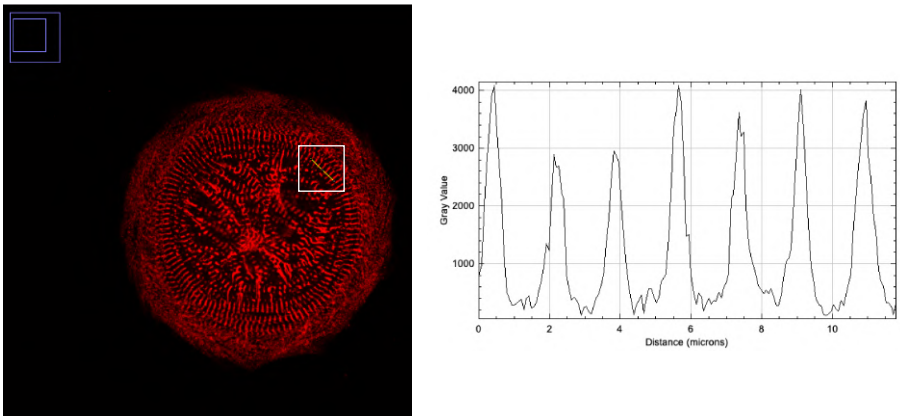

Figure 9. **Sarcomere disarray analysis.** Depicted on the left-hand side, one ROI selected from the α-actinin 2 staining of a CM picture; on the right, peaks indicate the incidence of a Z-disc.

2.5.4.2 Cell area measurement

Cell area was measured for α-actinin 2 channels as previously described [86]. Moreover, the number of nuclei from the Hoechst channel for each single cell was noted down. Cell perimeter was first traced with the wand tool and data from the area, maxima and minima were collected.

2.5.5 RNA extraction

RNA extraction was performed using the *TRIzol® Reagent* (*Thermo Fisher*, #15596026) protocol [87]. For this purpose, cell pellets from 2D disease modeling plates and frozen, homogenized EHTs were used. Cell pellets were incubated with 500 µl TRIzol® reagent for five minutes at room temperature. Similarly, homogenized EHT samples were incubated for 5 minutes in 300 µl TRIzol® reagent at room temperature. 0.2 ml of chloroform per 1 ml TRIzol® were added, tubes were vigorously shook for 15 second and incubated for two minutes at room temperature. Phase separation of RNA, DNA and protein occurred after a 12000 $\vec{g}$, 15 minutes centrifugation step at 4°C. Tubes were tilted at 45° and the aqueous solution of each was carefully pipetted out and transferred into a new tube. 0.5 ml of 100% isopropanol per 1 ml TRIzol® were added to the aqueous solution and samples were incubated for ten minutes at room temperature. A 15 minutes, 12000 $\vec{g}$ centrifugation step at 4°C was performed before the final RNA wash. Supernatant was removed from tubes and pellets were washed using 1 ml of 75% ethanol per 1 ml of initial TRIzol®. Samples were vortexed and centrifuged at full speed for 5 minutes at 4°C. Lastly, tubes were decanted and left for five minutes to dry before resuspending pellets in 20 µl ultrapure water.

2.5.6 Quantitative polymerase chain reaction

Real-time polymerase chain reaction (qPCR), also known as quantitative PCR (qPCR), was used to amplify and quantify DNA content of samples. In order to obtain the

first-strand of complementary DNA (cDNA), the *SuperScript™III First-Strand Synthesis SuperMix* for qPCR (*Thermo Fisher*, #11752-050 and #11752-250) kit was used [88]. 1 µg of cDNA samples were diluted in ultrapure water in a 1:10 ratio; 4.5 µl of diluted cDNA was mixed with 5 µl 2X SYBR Green and 0.5 µl of 10 µM primer pair for each qPCR sample. Primers used for qPCR can be consulted in *Appendix B*. Three technical replicates were prepared for each sample. qPCR was run using the *BioRad CFX384™ Real-Time System* and *C1000 Touch™* Thermal Cycler.

2.5.7 Western blot

Western blot (WB) analysis was used to detect protein expression. Protein concentration was detected through the *Qubit® Protein Assay Kit* (*Thermo Fisher*, #Q33211, Q33212). WB was performed using the *ProteinSimple Wes* machine. Samples were prepared according to the *Jess/Wes Separation* protocol from manufacturer and run in 66-440 kDa 8 x 25 capillary cartridges (*ProteinSimple*, SM-W008-1). Vinculin was used as a loading control (anti-Vinculin antibody V284: mouse, monoclonal, *Santa Cruz*, #SC-59803, 1:300). Antibodies used for IF purposes were also suitable for WB analysis.

2.5.8 Statistical analysis

Statistical analysis was performed using *Graph Pad Prism 8*. One-way analysis of variance (ANOVA) was used to compare the means of different datasets. The Bonferroni correction was used for multiple comparisons.

3 Results

3.1 Wnt/β-catenin pathway modulation of human iPSCs resulted in CM differentiation

2D monolayer-based differentiation of hiPSCs to mature CMs was obtained over a time span of 20 days, through the modulation of Wnt/β-catenin signaling [89]. *Figure 10* depicts the morphology of cells at the most important timepoints of differentiation. After approximately three days of expansion, as cells reached a confluency of 60-70%, mesodermal differentiation was induced with CHIR909921, a GSK3-β inhibitor. Several CHIR909921 concentrations were tested at first (data not shown); however, 7 μM was the concentration which yielded the best differentiation and that was used for all experiments. After 24h of CHIR909921, substantial amounts of cell death in all cell lines were observed. IWR1-endo is a Wnt inhibitor and was given after CHIR909921 as a substrate in culture medium to induce cardiac differentiation for 24h.

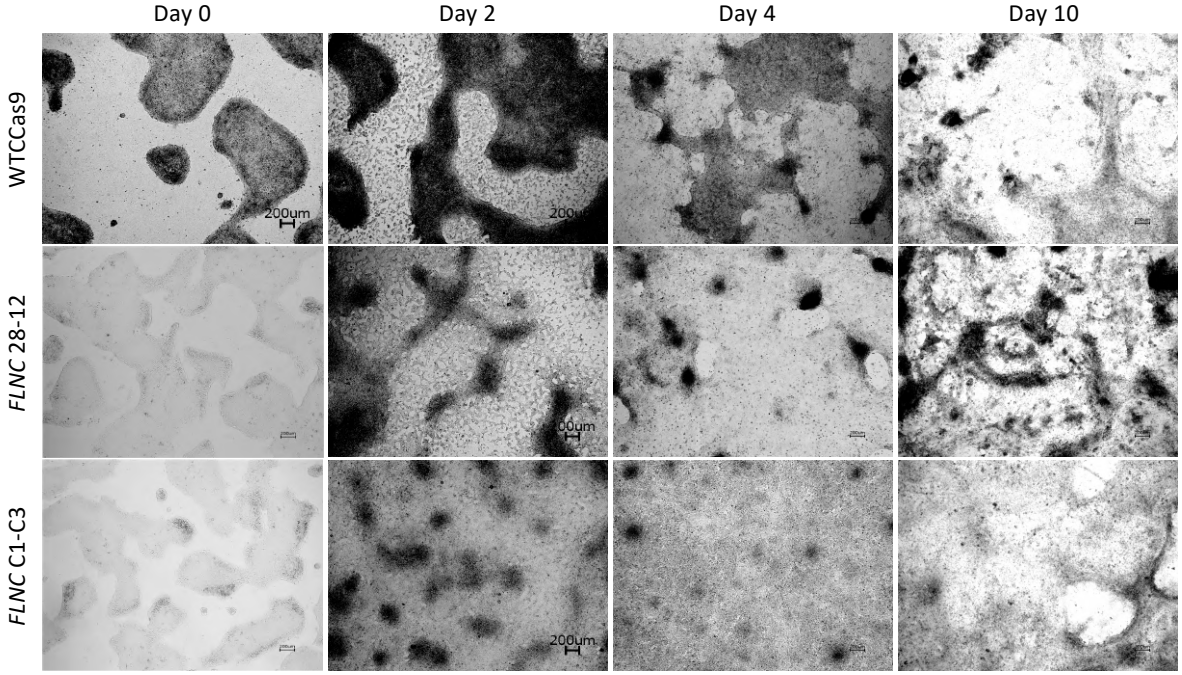

Figure 10. **2D cardiomyocyte differentiation of hiPSCs.** Depicted are the three different cell lines at the most important timepoints of differentiation from a state of pluripotency to the cardiac lineage. Day 0 represents the beginning of differentiation through incubation with CHIR90992; at day 2 cells were incubated with IWR1-endo; day 4 marks the beginning of maintenance and maturation until day 10, when lactate selection was performed to yield a higher purity of CMs in culture. Scale bars are shown in the images.

After 10 days of feeder-free culture, the hiPSC grew in flat colonies and formed monolayers. Spontaneous beating occurred from day 7 onwards and originated in isolated cell colonies to then expand to a confluent monolayer. Lactate selection was performed as

a purification method to enrich iPSC-CMs. Lactate was gradually supplemented for three days. The availability of different substrates allowed the cells to commit to the cardiac lineage and form a robust, synchronously beating monolayer.

The cell lines that yielded the best results, characterized by high iPSC-CM purity, were selected. Experiments were carried out using the control cell line WTCCas9, a heterozygous clone 28-12 and a homozygous clone C1-C3 for *FLNC*-mutant cell lines created in the WTC background.

3.1.1 Quality control validation of edited cell lines confirmed the creation of a functional disease model

Cell aliquots were frequently frozen and thawed. The genotype of used WTCCas9 and *FLNC*-mutant cell lines was verified before the beginning of every differentiation round by PCR amplification and Sanger sequencing. The intended single-nucleotide polymorphism (SNP) and three base pair (bp) deletion were detected (*Figure 11*). Results were consistent with the experimental design which can be found in *Appendix A*.

Unintended point-mutations, deletions or insertions can lead to non-specific genetic modifications. For off-target detection, PCR analysis was performed. The top three most likely off-targets were considered. *Figure 12* depicts the sequencing results for Off1 for the three cell lines, showing the presence of an intronic sequence in the targeted *locus* that is not altered. *Figure 13* shows the sequencing results for Off3 in WTCCas9. The sequence is not fully aligned most likely due to an error-prone polymerase reaction, since Off3 is a homopolymeric region. PCR was not successful for Off2. No sequencing results were collected, and further experiments will need to be performed to validate the off-target.

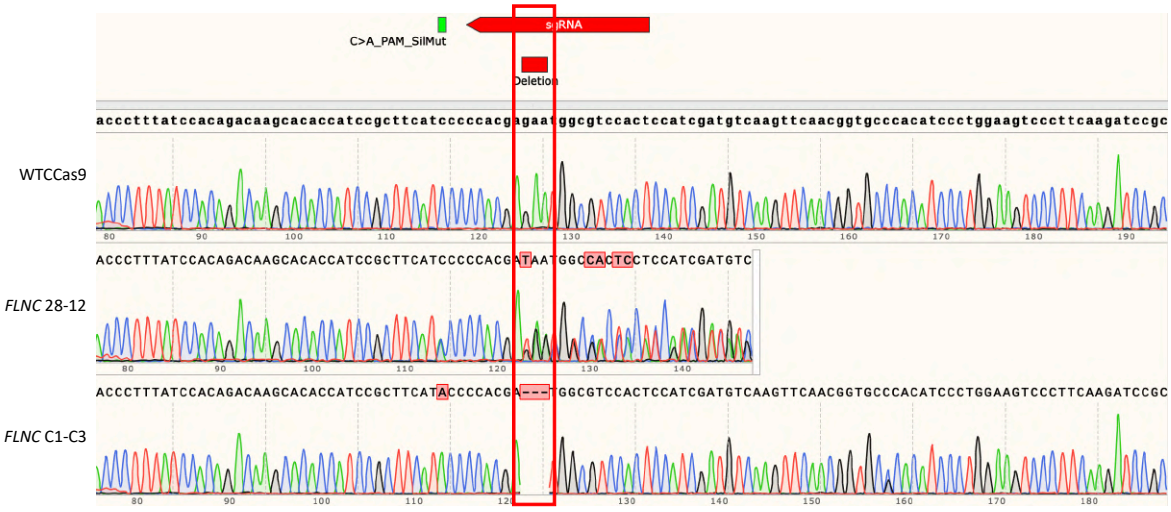

Figure 11. **Genotyping.** Sanger sequencing results for genotyping of WTCCas9, *FLNC* 28-12 and C1-C3 cell lines. Results were consistent with experimental design and the intended mutations were identified.

Figure 12. **Off-target sequencing for Off1.** Depicted are the results from off-target analysis for Off1 for WTCCas9, *FLNC* 28-12 and C1-C3.

Figure 13. **Off-target sequencing for Off3.** Depicted are the results from off-target analysis for Off3 for WTCCas9.

Amplicons were pooled and sequenced with NGS from *Genewiz®*. The intended deletion was detected in 55% of *FLNC* 28-12 alleles and 98% of *FLNC* C1-C3 alleles, confirming that these are heterozygous and homozygous mutations, respectively (*Figure 14*).

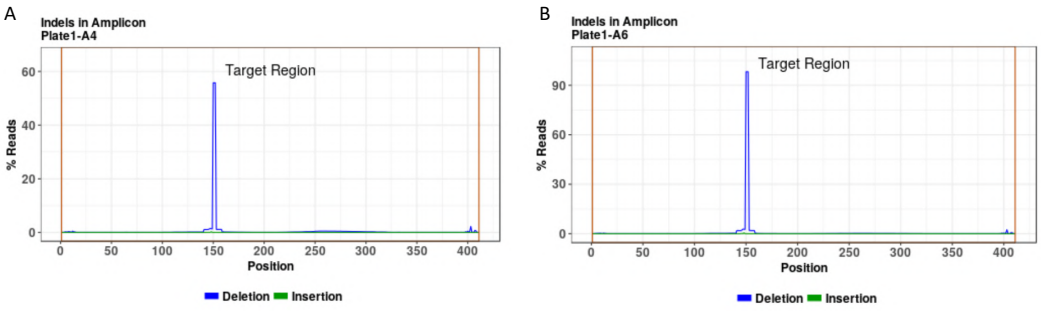

Figure 14. **Amplicon sequencing.** (A) 55% of *FLNC* 28-12 samples showed the intended deletion; (B) 98% *FLNC* C1-C3 showed the intended deletion.

Karyotyping was performed as a standard quality control analysis to accurately quantify chromosome number and detect aneuploidy, as chromosomal aberrations occurring in *in vitro* cultures may compromise experimental results. Results from the *nCounter®* Human Karyotype Panel are depicted in *Figure 15*. No chromosomal abnormalities were detected in the control cell line WTCCas9 and homozygous mutant cell line C1-C3. Chromosome 1, on the other hand, showed abnormalities for mutant cell line 28-12 visible as higher counts for certain genes. Chromosomal aberrations in sex chromosome Y were not considered as relevant for the purpose of the project.

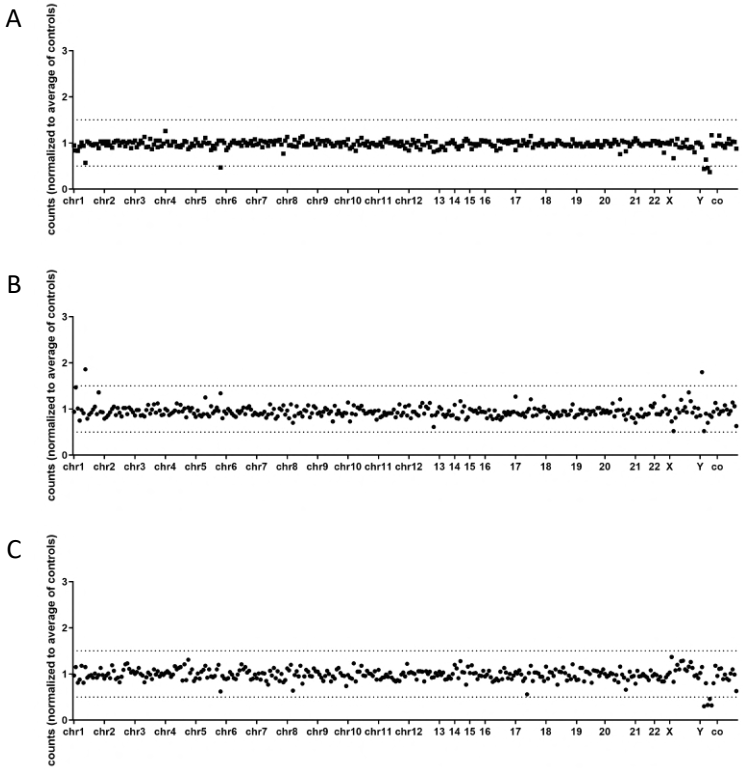

Figure 15. **Karyotyping of iPSC lines.** (A) WTCCas9 and (C) *FLNC* C1-C3 showed an apparently normal karyotype; (B) Potential gene duplication was detected for chromosome 1 in *FLNC* 28-12.

3.1.2 Cell lines are pluripotent and express cardiomyocyte markers

FACS experiments were performed to investigate pluripotency of used iPSC cell lines and to estimate the cardiac population after differentiation. *Figure 16* shows the results of the pluripotency analysis of the control cell line and the selected clones. The used molecular marker that verified the pluripotent status of stem cells was the cell surface protein SSEA-4. A second aliquot of cells from WTCCas9 was stained with the isotype control-PE to evaluate unspecific staining (*Figure 16-A*). Over 80% of WTCCas9 and clone 28-12 were positive for SSEA4 (*Figure 16-B, C*).

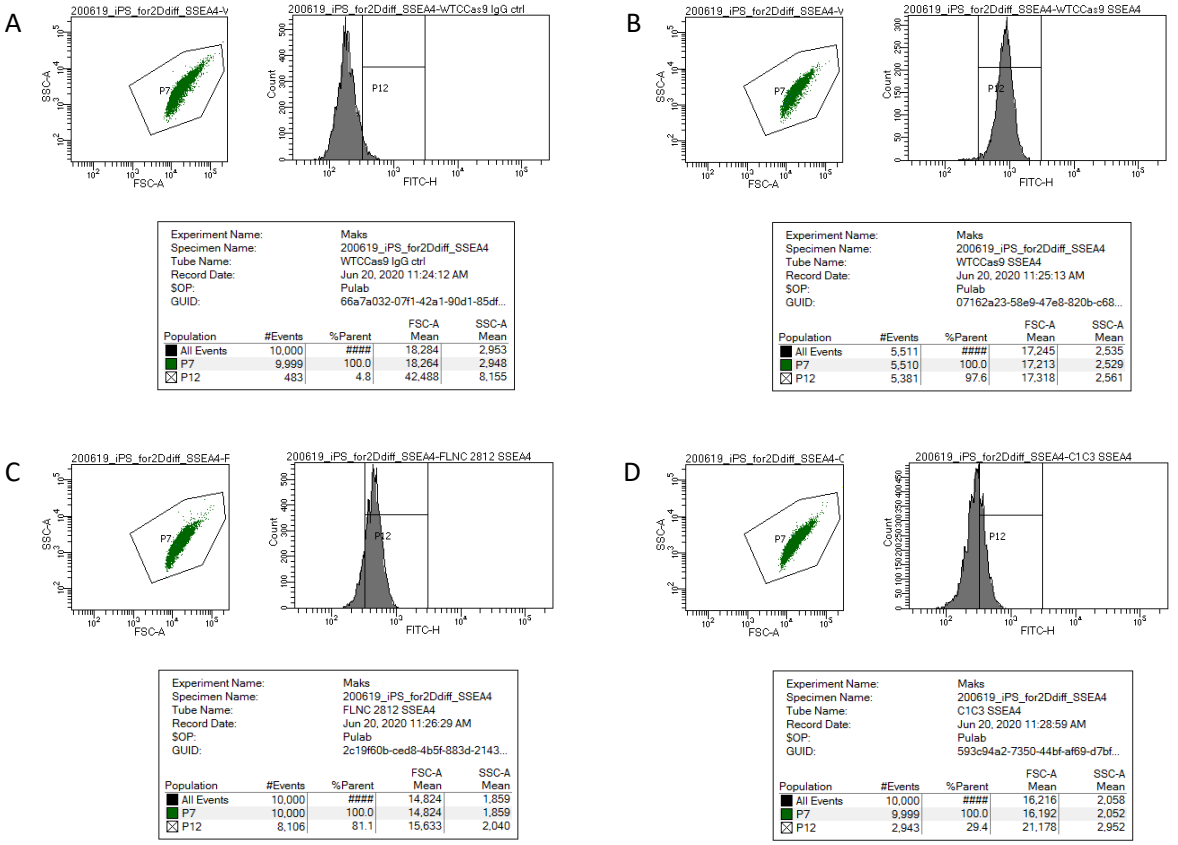

Figure 16. **FACS for pluripotency markers.** The panel picture shows the results from FACS staining using anti-SSEA4 for pluripotency. (A) Isotype (REA) control-PE staining of WTCCas9 was used to assess unspecific staining. (B) WTCCas9 showed 97.6% positive staining for SSEA4. (C) Clone 28-12 showed 81.1% and (D) clone C1-C3 showed 29.4% positive staining for SSEA4.

On the other hand, the cell population from the homozygous clone C1-C3 showed around 30% of positive staining in one of the FACS experiments (*Figure 16-D*).

Figure 17 shows the results of the evaluation of the CM population for the control cell line and the selected clones after differentiation. hiPSC-CMs express cardiac troponin T, a sarcomeric protein which is used as a standard marker for cardiomyocytes [79]. Therefore, the staining anti-cTnT was used. The cardiomyocyte population was in all cases above 80% and, in particular, of 98.4% for 28-12 and 99.3% for C1-C3. These results demonstrate the high efficiency of the differentiation protocol.

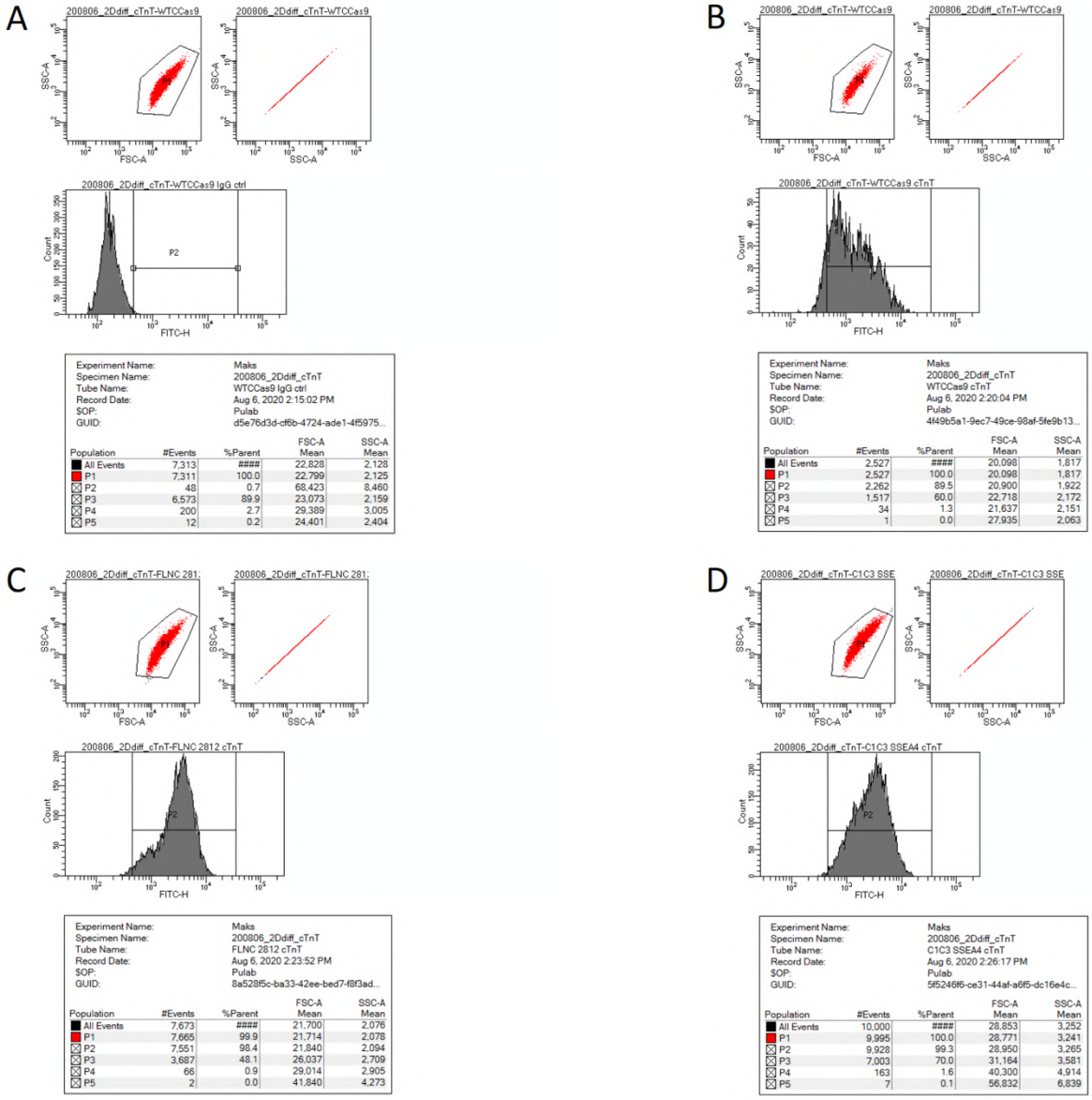

Figure 17. **FACS analysis for CM differentiation using anti-cTnT.** (A) Isotype (REA) control-PE staining on WTCCas9 was used to assess unspecific staining. (B) WTCCas9 was 89.5% positive for cTnT staining. (C) Clone 28-12 and (D) clone C1-C3 resulted positive 98.4% and 99.3% for cTnT staining, respectively.

Expression of pluripotency markers in iPSCs was also investigated by immunohistochemistry staining. *Figure 18* (A-C) shows the expression of pluripotency markers Oct4 (green) and Sox2 (red). The expression of surface marker SSEA4 (green) in iPS cell lines is visible in *Figure 18* (D-F).

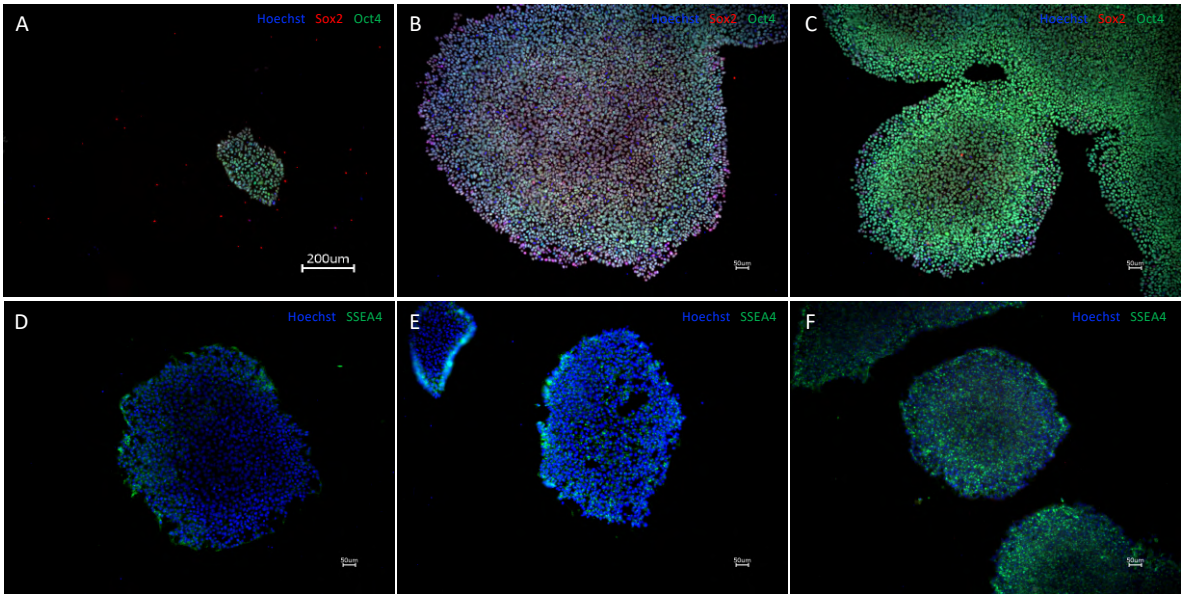

Figure 18. **Expression of pluripotency markers in iPSC lines.** Oct4 (green) and Sox2 (red) expression in cell colonies from (A) WTCCas9, (B) *FLNC* 28-12 and (C) *FLNC* C1-C3. SSEA4 expression (green) in cell colonies from (D) WTCCas9, (E) *FLNC* 28-12 and (F) *FLNC* C1-C3. Scale bars are shown in the images.

The presence of FLNC was investigated in iPSC. Interestingly, as shown in *Figure 19*, the protein is expressed in iPSCs (green).

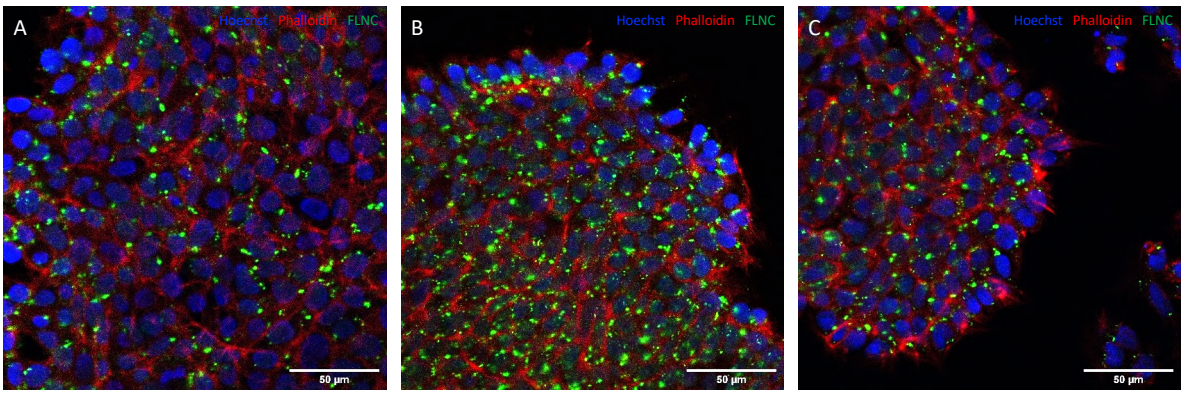

Figure 19**. FLNC expression in iPSC lines.** FLNC expression (green) in cell colonies from (A) WTCCas9, (B) *FLNC* 28-12 and (C) *FLNC* C1-C3. Scale bars are shown in the images.

3.2 Disease modeling using mutant iPSC-CMs reveals hallmarks of RCM

3.2.1 2D disease modeling suggests poor sarcomerogenesis in FLNC-mutant cell lines

WTCCas9, *FLNC* 28-12 and C1-C3 cells were seeded at low densities in 96-wells-plates and fixed after 7 and 30 days.

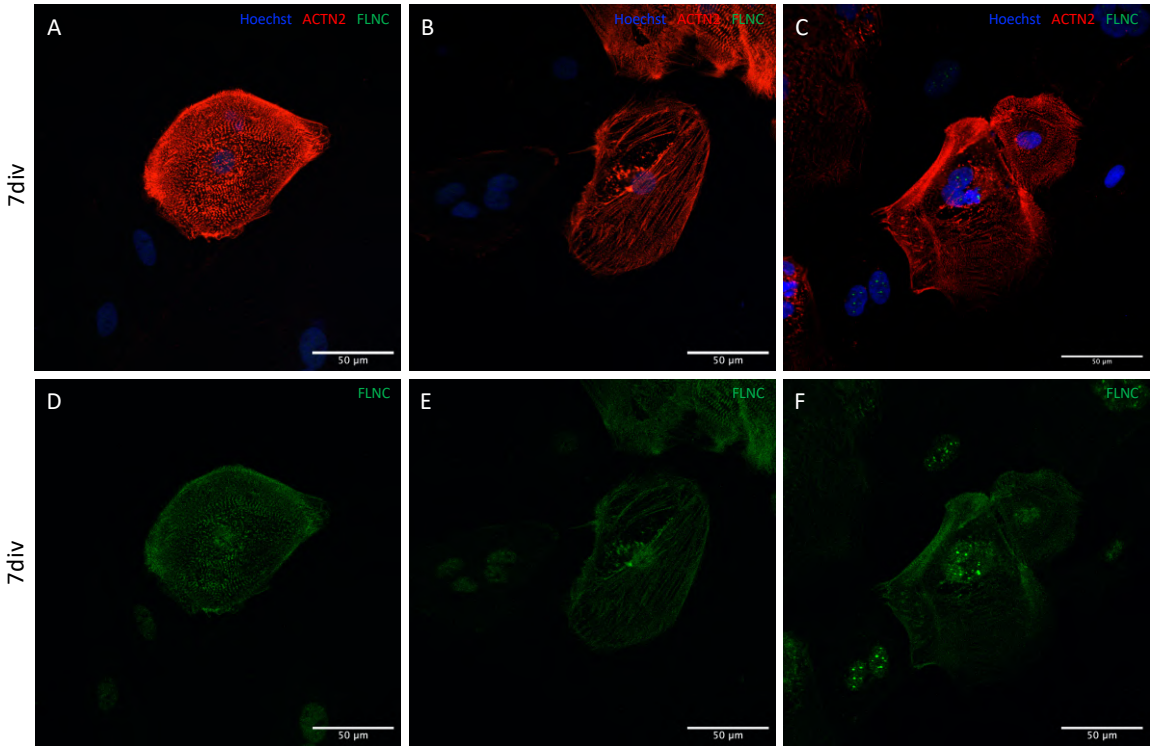

Figure 20. **2D disease modeling IF staining at 7 div.** The pictures show 2D disease modeling 7 div cells from (A), (D) WTCCas9, (B), (E) *FLNC* 28-12 and (C), (F) *FLNC* C1-C3 lines stained with Hoechst (blue), anti-*ACTN2* (red) and anti-*FLNC* (green). Magnification 63x. Scale bars are shown in the images.

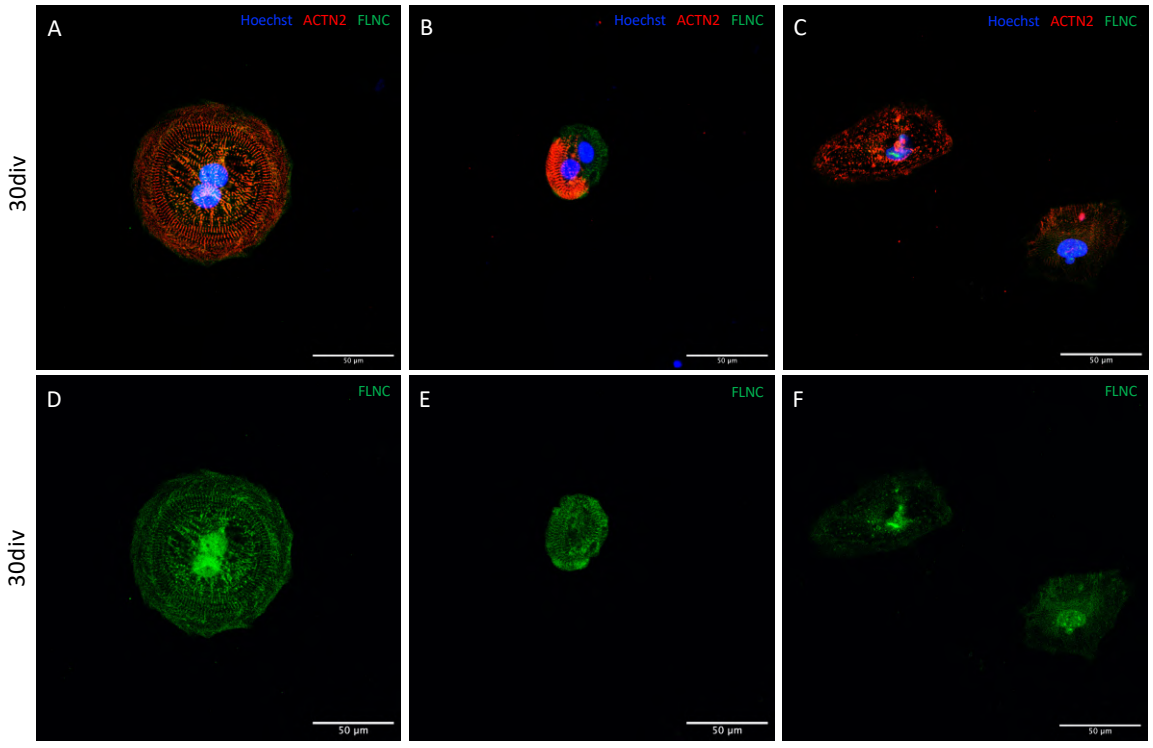

Figure 21. **2D disease modeling IF staining at 30 div.** The pictures show 2D disease modeling 30 div cells from (A), (D) WTCCas9, (B), (E) *FLNC* 28-12 and (C), (F) *FLNC* C1-C3 lines stained with anti-*FLNC* (green). Magnification 63x. Scale bars are shown in the images.

The two timepoints were chosen to investigate where FLNC localizes in the cell and how the *FLNC* mutation affects the cell phenotype over time.

Figure 20 compares single cells from the three cell lines. ACTN2 can be seen in red and corresponds to the Z-discs. The effect of the mutation on sarcomerogenesis is evident between the two timepoints, as sarcomeres from mutant cell lines appear less organized and generally disrupted when compared to the control. The signal for FLNC (green) is present prevalently as dots all over cell nuclei (blue) for the 7 div timepoint for all lines. On the other hand, the filament is expressed ubiquitously in the cell cytoplasm after 30 days *in vitro*. *Figure 21* shows the same pictures with the isolated channel for *FLNC*.

Cell area measurement was performed through the analysis of pictures with *Fiji* software. For this purpose, single cells stained with anti-ACTN2 were captured. The number of nuclei was also investigated. *Figure 22* depicts the results of the measurements from 7 div and 30 div. Cell area was bigger when compared to the control for both mutant lines at 7 div. On the contrary, cells belonging to *FLNC* C1-C3 reduced in size at 30 div. It appears that the initial hypertrophic signaling received by cells was altered by the homozygous mutation at 30 div. The number of multinucleated cells increased over time for *FLNC* 28-12.

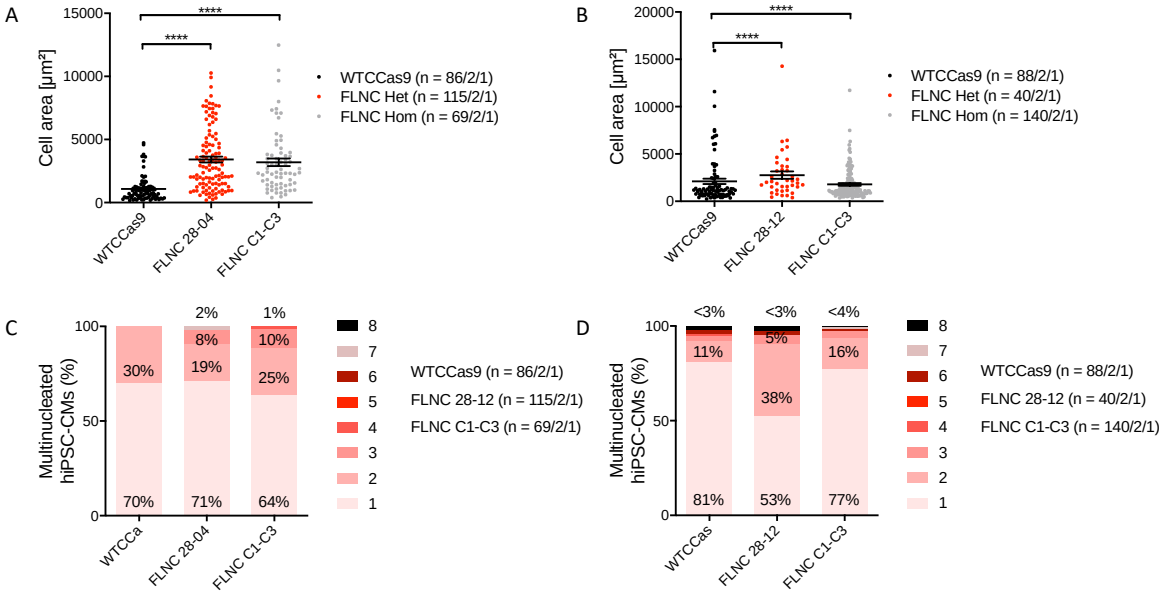

Figure 22. **Cell area and multinucleation analysis at 7 div and 30 div of 2D-cultured hiPSC-CMs.** Figure (A) and (B) show the results for cell area analyzed with *Fiji* software for the three cell lines at 7 div and 30 div, respectively. While cell area measurements for WTCCas9 remain similar between the two timepoints, the mutation affected hypertrophic signaling in cells from *FLNC* 28-12 and C1-C3, which shrunk in volume. Data are expressed as mean, SEM, one-way ANOVA with Bonferroni's post-test; **** $p<0.0001$ and n-numbers are indicated in the figure (number of cells/wells/differentiation). Figure (C) and (D) show the number of nuclei encountered in the three cell lines at 7 div and 30 div in percentages.

Sarcomere disarray analysis was performed using pictures collected with the α-actinin staining channel with *Fiji*. Ten pictures were analyzed for each cell line for both the 7

div and 30 div timepoint; three ROIs where defined for each analyzed cell using one-way ANOVA. *Figure 23* shows the collected results. Even though the pooled data is not enough to be statistically significant, it is evident that there is a trend for increased myofibrillar disarray in mutant cell lines when compared to their isogenic control. Further images will have to be analyzed to be able to make more accurate statistics and draw conclusions.

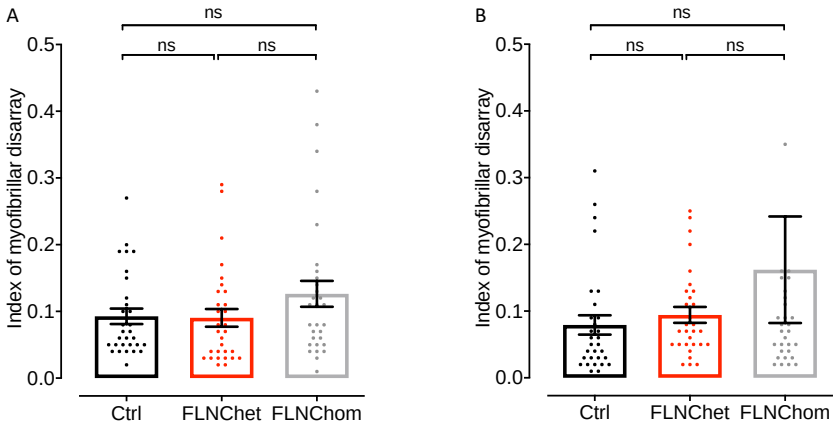

Figure 23. **Sarcomere disarray analysis at 7 div and 30 div of 2D-cultured hiPSC-CMs.** The figure depicts the results from the sarcomere disarray analysis performed using 7 div (A) and 30 div (B) images from 2D disease modeling cells (n=10 for each cell line). Data are expressed as mean, SEM, one-way ANOVA with Bonferroni's post-test.

Quantification of mRNA expression was done by qPCR. Genes playing an important role in the interaction with FLNC as well as important cardiomyocyte markers were investigated and will be discussed later on. The expression of hypertrophy marker *ACTA1* was not altered at the 7 div timepoint; it was downregulated in *FLNC* 28-12 while upregulated in the homozygous clone C1-C3 at the 30 div timepoint (*Figure 24*-A). This was true for the isoform *ACTA2* in both timepoints (*Figure 24*-B). The other two investigated hypertrophy markers were *NPPA* and *NPPB*. While the expression of NPPA was not subjected to significant changes, NPPB was upregulated at both 7 div and 30 div (*Figure 24*-N, O). The fibrosis marker *COL1A1* was downregulated at 30 div for both *FLNC* 28-12 and C1-C3 when compared to the control (*Figure 24*-G). *COL3A1* was instead downregulated for both mutant lines when compared to WTCCas9 at 7 div, while it was subjected to a significant downregulation at 30 div just for C1-C3 (*Figure 24*-H). The expression of the sarcomeric, actin-binding protein-encoding gene *ACTN2* was upregulated in homozygous mutant samples at 7 div and 30 div; on the other hand, it was downregulated in heterozygous mutant cell line at 30 div (*Figure 24*-C). *AXIN2*, coding for the β-catenin regulator of the Wnt pathway Axin2, was not subject to a significant change in expression (*Figure 24*-E).

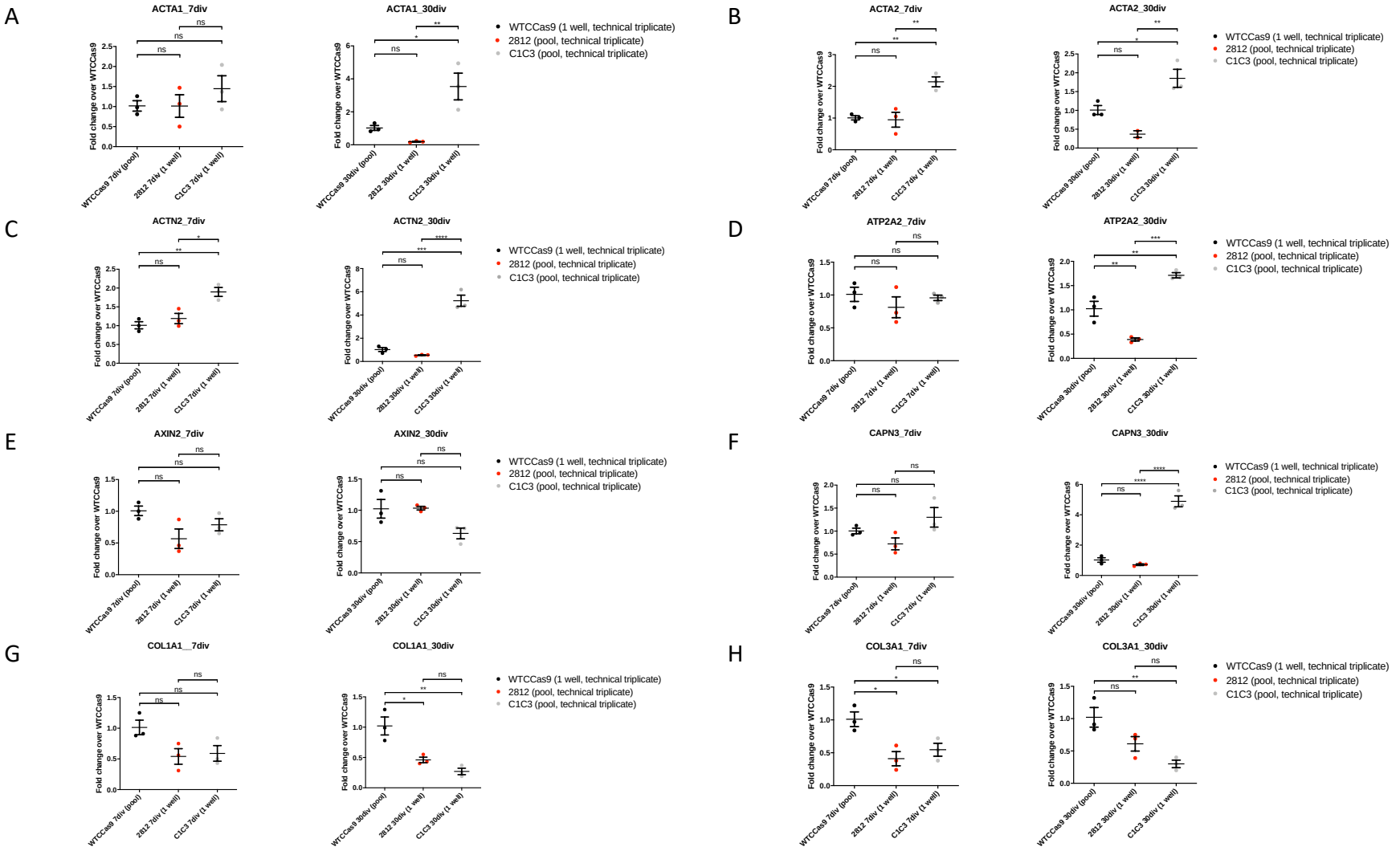
A
ACTA1_7div
ACTA1_30div
B
ACTA2_7div
ACTA2_30div
C
ACTN2_7div
ACTN2_30div
D
ATP2A2_7div
ATP2A2_30div
E
AXIN2_7div
AXIN2_30div
F
CAPN3_7div
CAPN3_30div
G
COL1A1__7div
COL1A1_30div
H
COL3A1_7div
COL3A1_30div
Fold change over WTCCas9
WTCCas9 7div (pool)
2812 7div (1 well)
C1C3 7div (1 well)
WTCCas9 30div (pool)
2812 30div (1 well)
C1C3 30div (1 well)
WTCCas9 (1 well, technical triplicate)
2812 (pool, technical triplicate)
C1C3 (pool, technical triplicate)

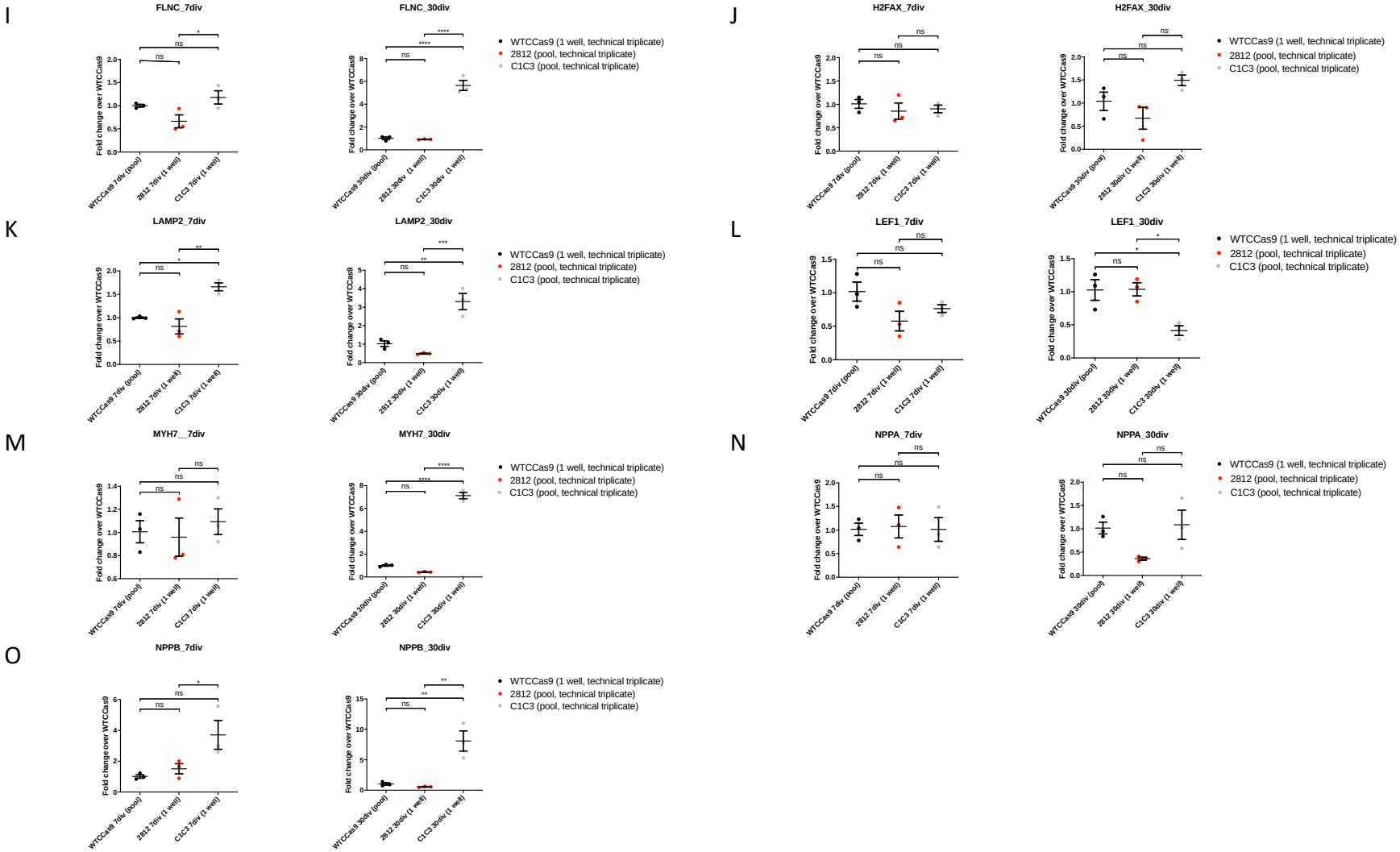

Figure 24. **Gene expression analysis of 7 div and 30 div 2D-cultured hiPSC-CMs using qPCR.** Data are expressed as mean, SEM, one-way ANOVA with Bonferroni's post-test; * p<0.05; ** p<0.01; *** p<0.001.

ATP2A2, which codes for the Ca^{2+} pump located in the endoplasmic reticulum and is associated with hypertrophic signaling, was downregulated in *FLNC* 28-12 samples but upregulated in *FLNC* C1-C3 samples at 30 div (*Figure 24*-D). Similar results were found for the expression of *CAPN3*. Gene expression did not experience any significant variation in mutant lines at the 7 div timepoint; it was downregulated in *FLNC* 28-12 samples while upregulated in *FLNC* C1-C3 samples at 30 div (*Figure 24*-F). When comparing heterozygous and homozygous mutants, the expression of *FLNC* was upregulated in *FLNC* C1-C3 samples on both timepoints and downregulated for *FLNC* 28-12 at 30 div (*Figure 24*-F). The double strand break marker gene *H2FAX* expression was not significantly affected by the mutation (*Figure 24*-J). The activity of *LAMP2*, an autophagy marker, was upregulated at 7 div and 30 div for the homozygous mutants when compared to the control line, while it was downregulated in *FLNC* 28-12 at 30 div (*Figure 24*-K). *LEF1*, coding for a T-cell receptor-alpha enhancer, was upregulated for *FLNC* 28-12 while downregulated in C1-C3 for the 30 div timepoint (*Figure 24*-L). While *MYH7*, the gene encoding for one of the heavy chains composing the myosin filament, did not vary its expression at the 7 div timepoint, it was significantly upregulated in *FLNC* C1-C3 cells at the 30 div timepoint; on the other hand, the expression in the control and *FLNC* 28-12 was downregulated when comparing the results from 7 div to 30 div (*Figure 24*-M).

WB analysis for protein expression in 2D disease modeling samples was performed using the *ProteinSimple Wes* capillary system. *VCL* was used as the housekeeping gene of choice as FLNC has a much higher molecular weight compared to GAPDH (used instead for qPCR) and cartridges available from the manufacturer did not support this difference.

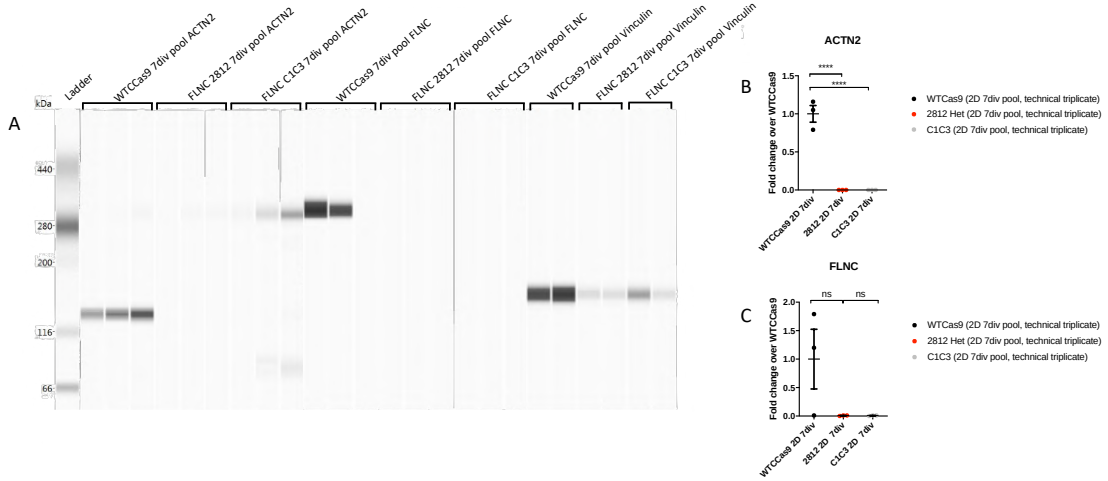

Figure 25. **Western blot for FLNC expression in 2D-cultured hiPSC-CMs 7 div samples.** (A) The picture shows the result of the blot performed with the *Wes* machine. Lane 2 to 9: ACTN2 (100 kDa) is expressed in WTCCas9 samples; for mutant samples, faint bands are visible at the same height of FLNC. Lane 11 to 19: FLNC (290 kDa) is expressed in control cell line samples, but no band is visible for mutant cells. Lane 20 to 25: vinculin (117 kDa) was used as a loading control and is expressed in all specimens, as represented from its defined bands. (B) ACTN2 expression was significantly downregulated in mutant cell lines. (C) Statistical analysis yielded no significant result for FLNC expression. One-way ANOVA analysis was used; **** $p<0.0001$.

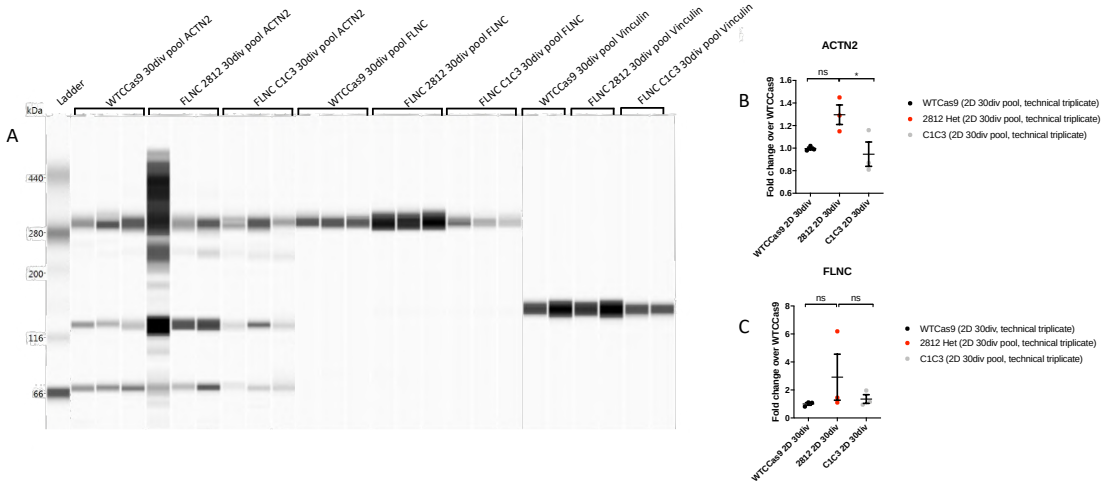

Figure 26. **Western blot for FLNC expression in 2D-cultured hiPSC-CMs 30 div samples.** (A) The picture shows the result of the blot performed with the *Wes* machine. Lane 2 to 9: ACTN2 (100 kDa) is expressed in all samples; multiple bands were detected both at ACTN2 molecular weight, but also at the same height as FLNC. Lane 5: overloaded. Lane 11 to 19: FLNC (290 kDa) is expressed in all cell lines. Lane 20 to 25: vinculin (117 kDa) was used as a loading control and is expressed in all specimens. (B) ACTN2 expression was significantly downregulated in mutant cell line C1-C3 when compared to the control. (C) Statistical analysis yielded no significant result for FLNC expression. One-way ANOVA analysis was used; * $p<0.05$.

Figure 25 and *26* illustrate the results from the analysis for the 7 div and 30 div timepoints samples, respectively. Three replicates from one pooled sample of each cell line were used. At 7 div, the expression of ACTN2 (100 kDa) appears to be present only for the control cell line, while a slight expression can be observed at the same height of FLNC (290 kDa) for mutant samples. The expression of FLNC was detected for WTCCas9 samples. Mutant cell lines show no expression of FLNC, yet results may be compromised by the high expression of vinculin, which caused normalization during statistical analysis with one-way ANOVA to be null. At 30 div, the expression of ACTN2 was present for all samples. Multiple bands were detected, also at the same height of FLNC, suggesting the proteins might interact at a sarcomeric level. FLNC expression was detected in all samples.

3.2.2 3D disease modeling recapitulates the hallmarks of RCM caused by the *FLNC* mutation

EHTs were fixed and snap frozen after 32 div. Glass slides were prepared for IF experiments to investigate the phenotype of the mutant *FLNC* models when compared to the control. *Figure 27* and *28* show cryosections of the 3D models taken with 63x and 40x objectives. Consistent with previous observations in 2D models, sarcomerogenesis appears to be compromised in *FLNC* 28-12 and C1-C3, where the ACTN2 staining (red) highlights rather isolated islets of cardiomyocytes in the tissue.

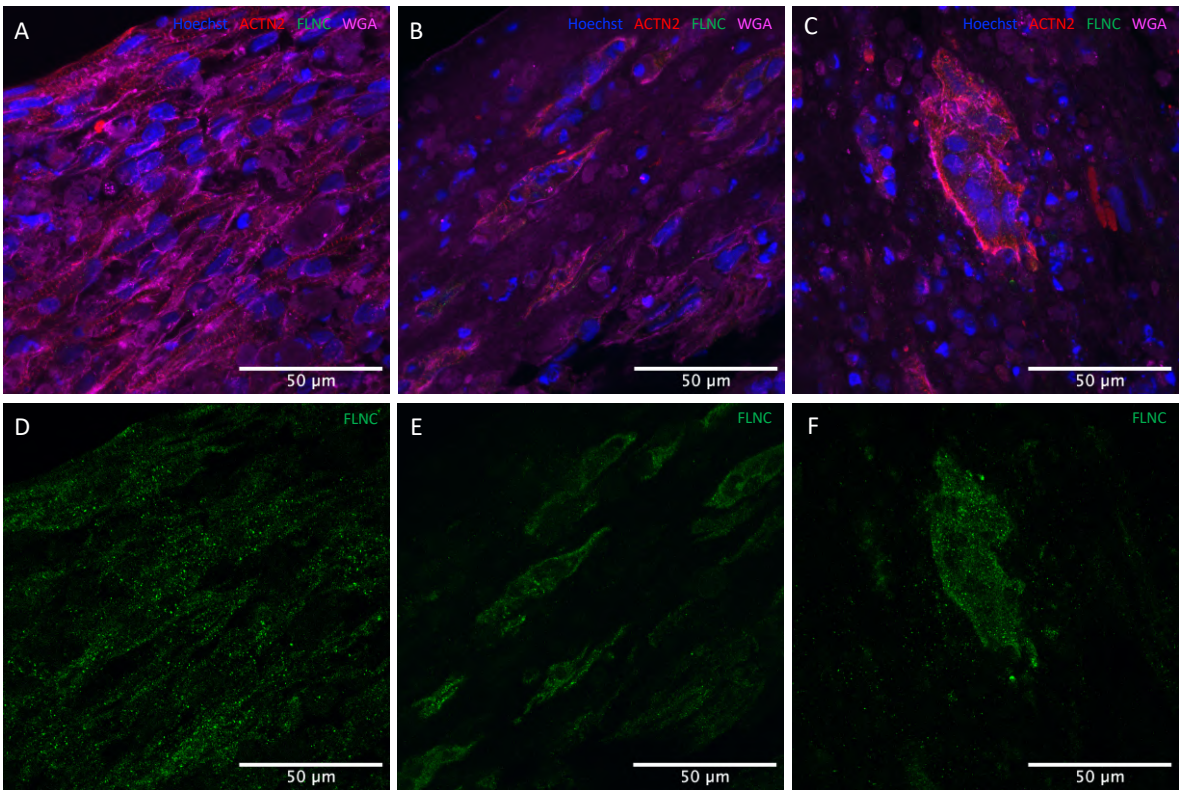

Figure 27. **IF staining of EHTs.** The figure depicts sections of EHTs fixed at 32 div from (A), (D) WTCCas9, (B), (E) *FLNC* 28-12 and (C), (F) *FLNC* C1-C3. Magnification 63x. Scale bars are shown in the images.

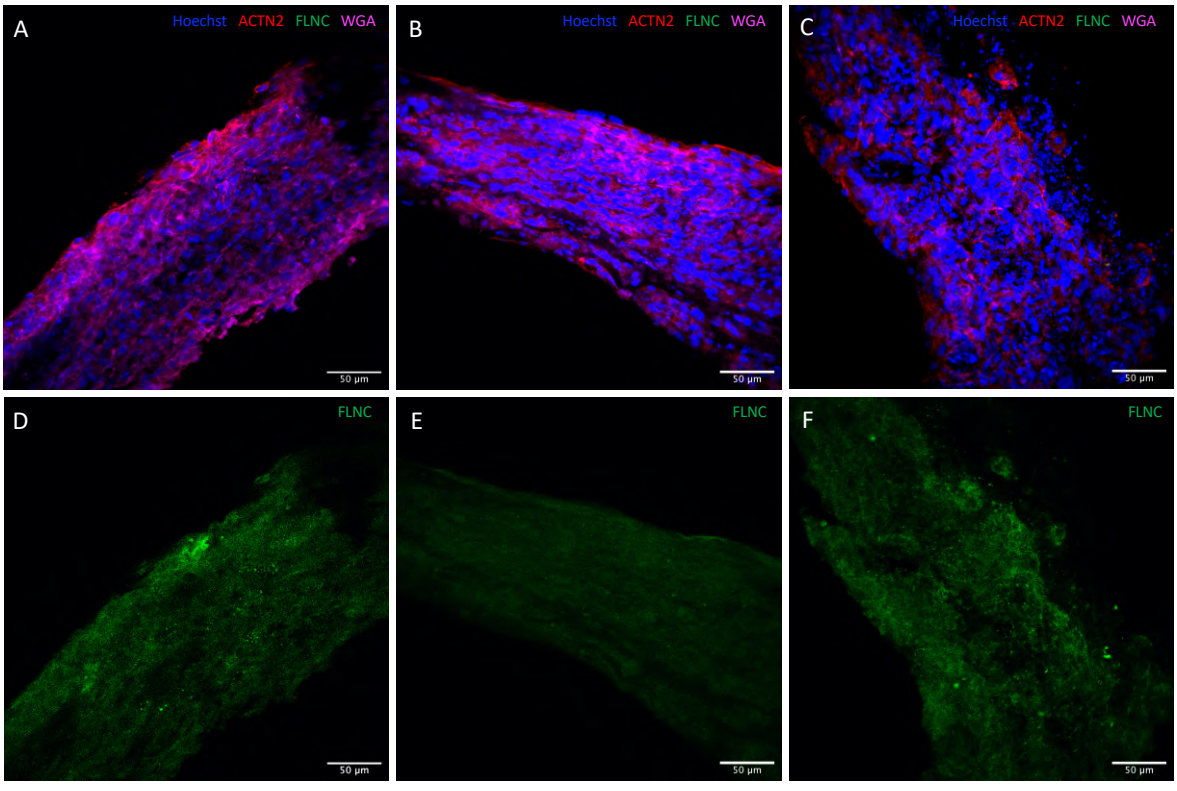

Figure 28. **IF staining of EHTs.** The figure depicts sections of EHTs fixed at 32 div from (A), (D) WTCCas9, (B), (E) *FLNC* 28-12 and (C), (F) *FLNC* C1-C3. Magnification 40x. Scale bars are shown in the images.

WGA (magenta), which binds to glycoproteins of the cell membrane and is used to determine myocyte density, accentuates the visualization of this prominent difference to the control. Multinucleation and nuclear fragmentation is particularly evident in the 40x pictures (blue). The signal for FLNC (green) colocalizes with cardiomyocytes and, particularly, with both ACTN2 and their nuclei.

Quantification of mRNA expression was done by qPCR. Once again, the expression of various genes potentially connected to the function of FLNC and different cardiomyocyte markers was investigated. *ACTA1*, *ACTA2*, *NPPA* and *NPPB* are hypertrophy markers. *ACTA1* and *ACTA2* were significantly upregulated in homozygous mutant EHTs (*Figure 29*-A, B); while *NPPA* is generally downregulated in mutant lines, *NPPB* is upregulated (*Figure 29*-N, O). The expression of *ATP2A2* was downregulated in EHTs from mutant cell lines (*Figure 29*-D). *ACTN2* expression and, therefore, the transcription of the corresponding actin-binding protein was not differently regulated in mutant EHTs (*Figure 29*-B). The gene encoding another protein associated with sarcomerogenesis, *MYH7*, was also unaltered (*Figure 29*-M). The expression of *CAPN3*, the gene coding for isoform 3 of calpain, was not significantly different among EHTs (*Figure 29*-F). Fibrosis markers *COL1A1* and *COL3A1* were downregulated in heterozygous mutant EHTs, yet the expression of *COL1A1* was upregulated in the homozygous EHT when compared to the heterozygous counterpart (*Figure 29*-G and H). *LAMP2*, an autophagy marker, was downregulated in the *FLNC* C1-C3 EHT (*Figure 29*-K). Similarly, the gene related to the β-catenin regulator in the Wnt pathway, Axin2, was downregulated in the homozygous mutant (*Figure 29*-E). *H2FAX*, a DNA double strand break marker, was downregulated in the heterozygous mutant EHT (*Figure 29*-J). T-cell receptor-alpha enhancer LEF1-related gene showed no significant changes (*Figure 29*-L). Finally, while *FLNC* expression remained unchanged in heterozygous mutant EHT, it was upregulated in the homozygous counterpart (*Figure 29*-I).

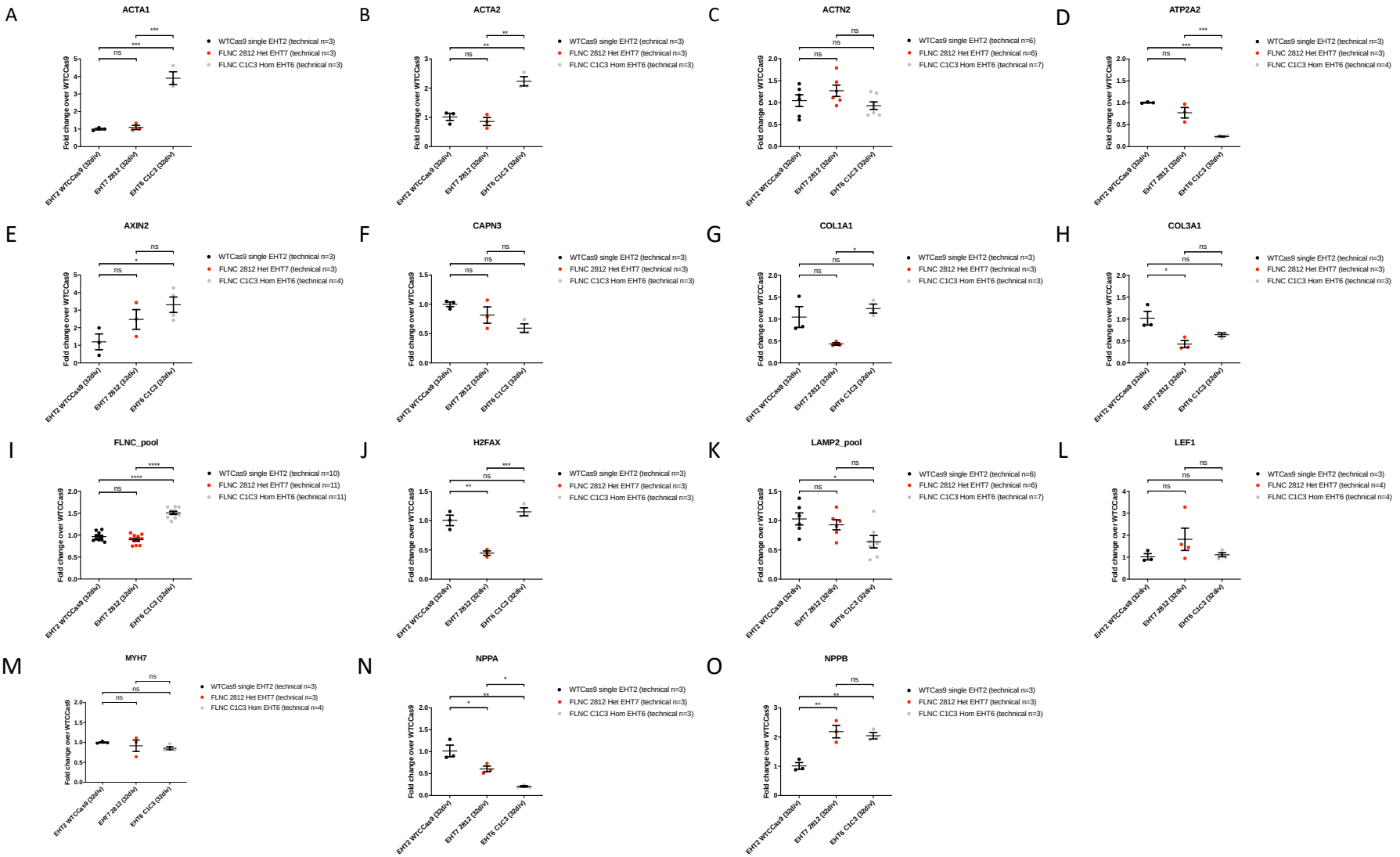

Figure 29. **Gene expression analysis of 32 div EHTs using qPCR.** Data are expressed as mean, SEM, one-way ANOVA with Bonferroni's post-test; * p<0.05; ** p<0.01; *** p<0.001.

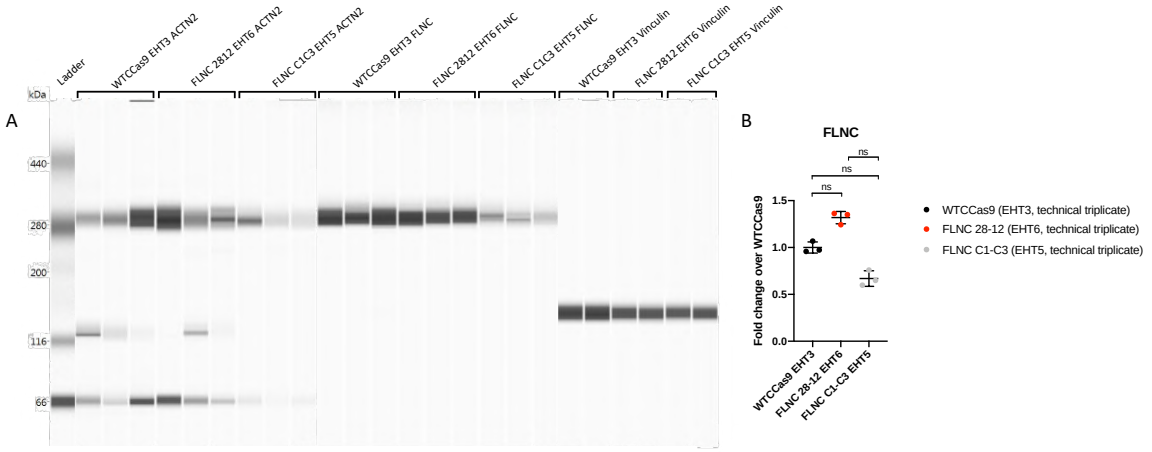

Figure 30. **Protein expression analysis by WB in single EHTs cultured for 32 div.** (A) Results of the blot performed with the *Wes* machine are shown. Lane 2 to 9: ACTN2 (100 kDa) is expressed in EHTs, but bands aligning at the same molecular weight of FLNC suggest the interaction of the proteins. Lane 11 to 19: FLNC (290 kDa) is expressed in EHTs generated with CMs from all three cell lines. Lane 20 to 25: vinculin (117 kDa) was used as a loading control and is expressed in all specimens, as represented from its defined bands. (B) Quantification of FLNC expression for the three EHT samples. FLNC synthesis appears to be upregulated in the heterozygous mutant EHT *FLNC* 28-12, yet statistical analysis yielded no significant result. One-way ANOVA analysis was used; * $p<0.05$.

Protein expression analysis in EHTs was performed using the *ProteinSimple Wes* capillary system. Vinculin was chosen as the housekeeping gene. *Figure 30* illustrates the results from the analysis (left) and the quantification of *FLNC* expression plotted in *Prism*. Three technical replicates were prepared for each EHT specimen. FLNC protein expression is upregulated in heterozygous mutant EHT *FLNC* 28-12 when compared to the control line. On the other hand, FLNC is downregulated in homozygous mutant EHT *FLNC* C1-C3. Interestingly, the blot shows bands for ACTN2 expression at the same height as FLNC, while its molecular weight is of 100 kDa and no bands were detected at this height.

Contraction analysis was performed using the *Fiji* open-source plugin *MUSCLEMOTION*. 20 seconds videos were captured at 30 fps from 7 div to 32 div, when EHTs were fixed for other downstream analyses. *Figure 31* shows a representative example of the analyzed videos and the output graphs generated by the software. The graphs show peaks in correspondence to a contraction. Contraction force was measured in arbitrary units (a.u.). It is evident that both contraction force and frequency vary among the three used cell lines. When comparing the control cell line WTCCas9 to mutant cell lines *FLNC* 28-12 and C1-C3, the force of contraction was generally greater (*Figure 31*). Moreover, *FLNC* 28-12 showed a higher contraction frequency than C1-C3.

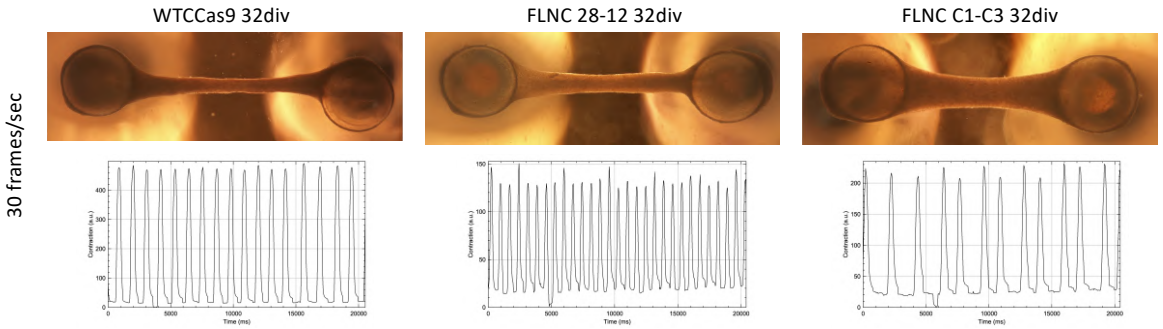

Figure 31. **Video acquisition and *MUSCLEMOTION* analysis of EHTs.** The figure depicts an example of video acquisition and analysis through the *Fiji* plugin *MUSCLEMOTION* for the contraction of EHTs. Contraction force was measured in a.u. over a time span of 20 seconds for videos captured at 30 fps. The graphs show peaks in correspondence of a contraction. Differences in frequency and contraction force are evident among the three cell lines. 152 pixels = 1 mm.

The mutation induced contraction complications, resulting in a lower force of contraction and an arrhythmic phenotype at traces (data not shown). The contraction profile of EHTs showed variance throughout the time in which models were monitored (*Figure 32)*. Arrythmia is particularly evident in contraction analysis graph from *Figure 33*, where contraction complications caused shifts in the baseline for mutant EHT model. Electrical conduction in *FLNC* C1-C3 EHTs was slow and resembled a propagating wave. This might be due to the fact that, as visible from the severe areas of cell death in the cryosections, cardiomyocytes were present as isolated islets.

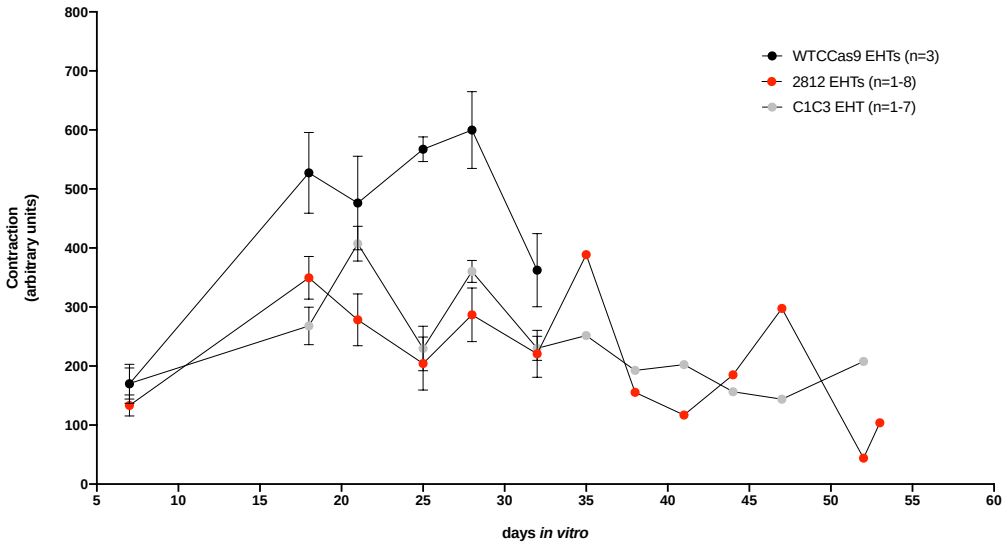

Figure 32. **EHTs force development overtime.** Plotted is the average of the force of contraction of EHTs obtained from the *MUSCLEMOTION* analysis. EHTs were monitored from 7 div to 32 div, when they were sacrificed for downstream analysis; two EHTs, one from the heterozygous and one from the homozygous mutant line, were kept in culture and monitored until 53 div.

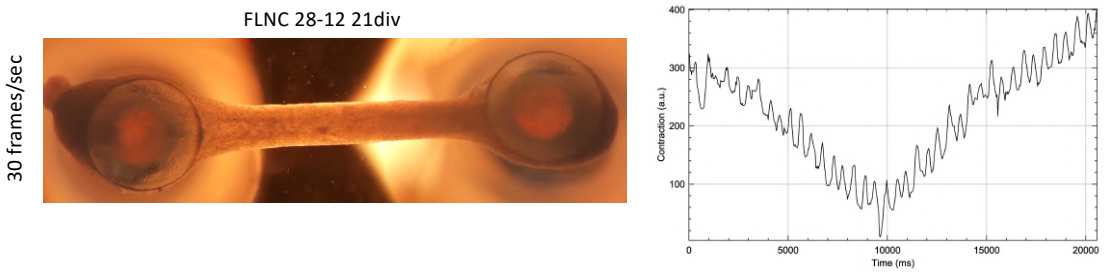

Figure 33. **Arrhythmic contraction profile of EHTs.** The figure depicts the contraction profile of mutant EHT *FLNC* 28-12 at 21 div, when arrhythmia was detected (baseline irregularity). 152 pixels = 1 mm.

Figure 34 shows the average contraction force at 7, 21, 28 and 32 div for all pooled EHTs. Along with the findings presented above, the force exerted by the controls WTCCas9 was greater than the one from *FLNC* 28-12 and C1-C3 EHTs. The result was consistent over time.

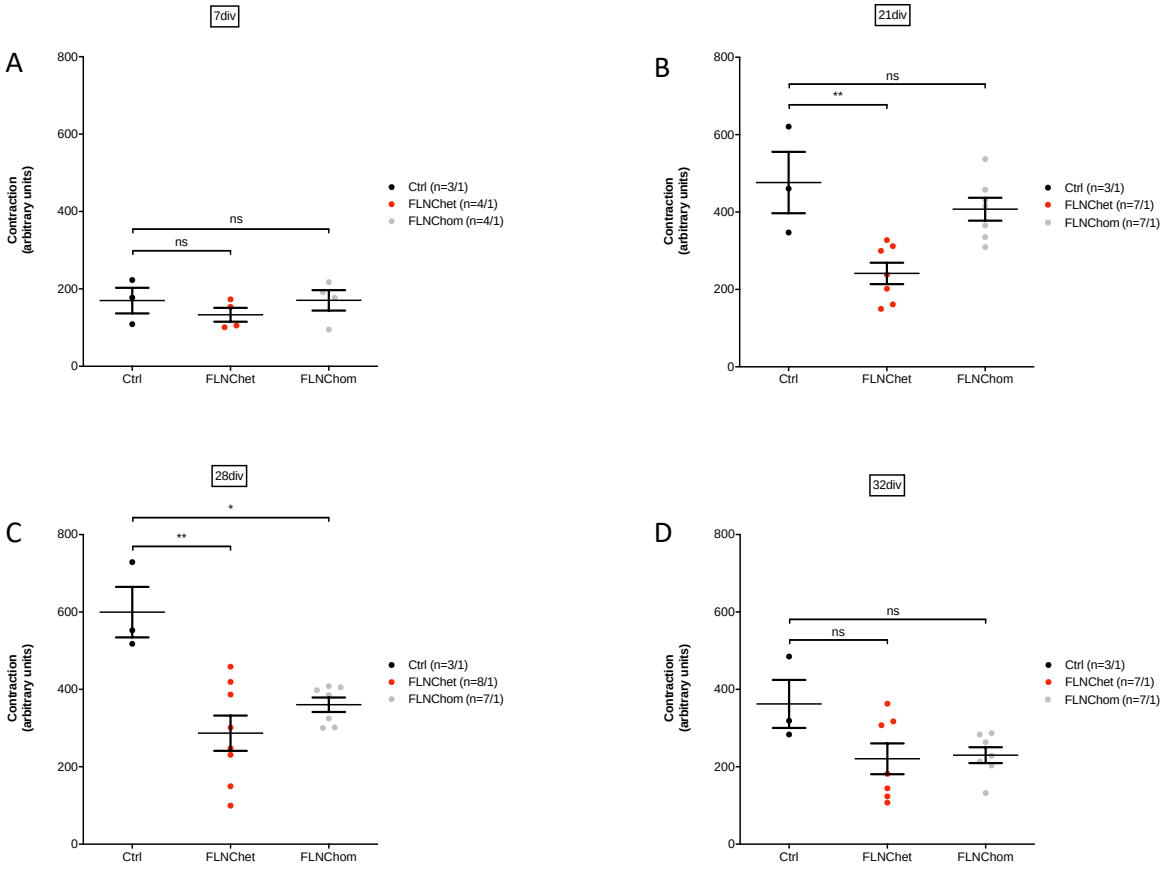

Figure 34. **Pooled contraction data from all EHTs.** The graphs show the average of the contraction force measured by *MUSCLEMOTION* from all EHTs at (A) 7, (B) 21, (C) 28 and (D) 32 div. A trend of lower contraction force exerted by mutant models when compared to the control EHTs is visible. One-way ANOVA analysis was used; two stars indicate a P value <0.01; n-numbers are indicated in the figure (number of EHTs/batch).

Two EHTs, one *FLNC* 28-12 and one C1-C3, were kept in culture to monitor the progression of the altered phenotype. Interestingly, at 53 div, most likely due to progressive cell death, tissue stiffness and an altered contraction profile led the homozygous mutant EHT to detach from the posts (*Figure 35*).

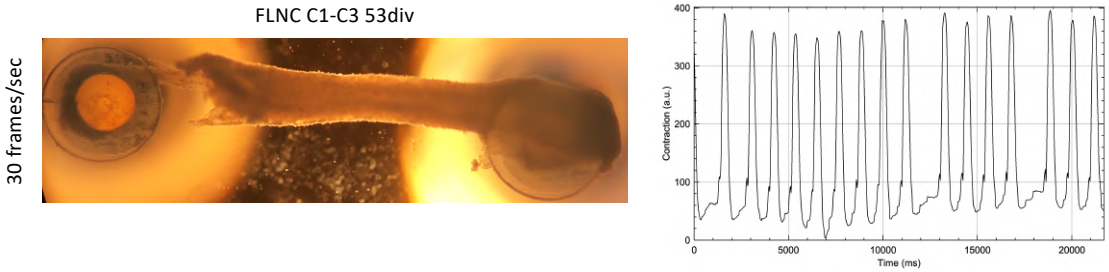

Figure 35. **Engineered RCM model death.** The figure shows homozygous mutant *FLNC* C1-C3 at 53 div, when the model had to be sacrificed to prevent disruption from the silicone post. 152 pixels = 1 mm.

4 Discussion

4.1 Usage of iPSC-CMs for disease modeling

The generation and application of iPSCs technology made new opportunities for cardiovascular research and therapies possible. Human iPSCs can be differentiated *in vitro* to almost all cells belonging to the three primary germ layers and, in turn, all the cell types present in the body. The development of reproducible and efficient protocols for differentiation is fundamental to achieve the desired cell type. *In vitro* differentiation generally recapitulates the stepwise stages of embryonic development of a selected cell type [77].

Various protocols were developed for the differentiation of iPSC into mature CMs, such as the embryoid body-mediated differentiation and the monolayer differentiation to CMs. Early efforts for the differentiation of stem cells into cardiomyocytes relied on protocols using EBs. However, often less than 25% of cells in an EB resulted in beating cardiomyocytes, making it an inefficient method [76]. Higher differentiation efficiencies were displayed by a monolayer-based differentiation protocol using the cytokines activin A and BMP4. Yet, this protocol is still rather inefficient, uses expensive growth factors and only functions in a limited number of human stem cell lines [90]. More recently, a highly efficient, monolayer-based cardiomyocyte differentiation protocol for iPSCs using the modulation of the Wnt/β-catenin pathway was developed [89].

For the purpose of this project, the monolayer differentiation of iPSC forming cultures containing beating cardiomyocytes was selected. The methods described in this work employed the modulation of the Wnt/β-catenin pathway using the small molecules CHIR and IWR to obtain a large amount of pure hiPSC-CMs, which is critical for disease modeling. Undifferentiated hiPSCs were induced to undergo mesodermal differentiation by the GSK3-β inhibitor CHIR and subsequent cardiac differentiation was induced with the Wnt signaling inhibitor IWR1 [79], [89]. Differentiated cardiomyocytes were further purified using the adaptation of a glucose starvation method. The method was proven to be density-dependent, *i.e.* cardiomyocyte survival is directly proportional to the percentage of cardiomyocyte population [79]. The transition to low-glucose medium is a stressful condition for cardiomyocytes and, for this reason, lactate was used since CMs are capable of producing energy from alternative sources to glucose such as lactate or fatty acids. Lactate was added to cultures for three days starting on day 10. However, the transition from glucose to pure lactate in culture medium was modulated by the gradual elimination of B27 from RPMI. B27 was then similarly reintroduced. B27 is a supplement used to support growth of stem cells. The presence of both the substrates in culture medium and the gradual switch to lactate was most likely beneficial for cardiomyocyte differentiation efficiencies, since FACS analysis for cTNT resulted to be positive above 80% for all cell lines.

The first rounds of differentiation served to test the protocol with different clones and to select what appeared to be the best candidates for disease modeling. Differentiation was carried out using the best clones among the generated ones. Variance in differentiation was

observed for cell morphology in monolayer formation, cell debris and beating areas were at traces inconsistent among clones from the same line. For this reason, further experiments testing more clones could be helpful to obtain a more robust model.

iPSC-based disease modeling represents a very powerful tool in biomedical research and personalized regenerative medicine. The use of iPSCs in research opens the possibility to reveal novel pathological mechanisms at the cellular level and, nowadays, a multitude of applications for high throughput drug discovery platforms and safety pharmacology associated with 3D multicellular organoids are emerging [91].

In order to delineate the etiology and pathophysiology of a disease, a physiologically relevant experimental model capable of recapitulating the pathophysiology and clinical manifestations is critical. Due to their unlimited supply, their human origin, their derivation from potentially any individual, easy accessibility and scalability, human iPSC-based disease models are a promising candidate [91]. However, limitations exist in their application, representing future challenges that will need to be overcome for an efficient clinical translation. These challenges include, for example the derivation of clinical grade iPSC-derived therapeutic cell products for acute life-threatening conditions. As a matter of fact, the selection of the donor cell type for reprogramming is the first step in generating iPSCs and it has been reported that cells retain some degree of residual epigenetic memory from the somatic cell source from which they derive. As a result, their differentiation potential into certain cell types could be biased due to the incomplete resetting of the non-CpG methylation patterns during reprogramming [92]–[94]. Residual epigenetic memory has been proven to diminish over time as the cells are passaged in culture [95]. Certain types of cells such as skin biopsy-derived dermal fibroblasts might carry more mutational burdens and chromosomal abnormalities because of exposure to ultraviolet radiation and high cell turnover rates [96]. The iPSC line used in this project was purchased from the Coriell Institute and an apparently healthy karyotype of the donor was certified by the manufacturer.

Defining the quality attributes of good iPSCs and the derived differentiated products is crucial due to the huge variability in terms of *e.g.* differentiation potential, epigenetic status, tumorigenic and immunogenic potential, maturation characteristics, batch variability and co-occurrence of heterogeneous populations of lineage subtypes or non-relevant cells [91]. To overcome phenotypic heterogeneity within the same line and assess genetic stability, different methods were used throughout the development of the RCM model. iPSCs can indeed accumulate chromosomal abnormalities, genetic instability, copy number variations and loss of heterozygosity over time when cultured and expanded *in vitro* [91]. As cells were kept in culture over a long period of time, quality control tools were frequently used, and frozen aliquots were prepared to avoid high passaging numbers.

The WTCCas9 control cell line was genetically engineered in the laboratory to induce the expression of SpCas9 through doxycycline for genome editing. Genotyping was used to verify the genotype and the correct insertion of the intended mutation in the CRISPR/Cas9-edited lines and their isogenic control. Even though the use of CRISPR/Cas9 based gene or base editing enhance genetic editing efficiently in human ESCs and iPSCs, the major

challenge with such gene engineering tools is the presence of possible off-target effects [97]. Off-target analysis was performed to avoid undesired effects including point-mutations, deletions or insertions potentially leading to non-specific genetic modifications. One out of three off-target regions was successfully assessed, as the homopolymeric region Off3 showed a not fully aligned sequence, which could be caused by an error-prone polymerase reaction. PCR was instead not technically successful for Off2. Moreover, amplicon sequencing was performed as a quality control tool to determine whether the intended mutation was correctly introduced and distributed for each cell line. Lastly, karyotyping was performed to detect chromosomal aberrations which may compromise experimental results. Karyotyping should be carried out every ten passages in long-term cultures for quality control purposes.

Altogether, it is clear how quality control experiments have an essential role in disease modeling and for good laboratory practice in general. Quality control ensures precision and accuracy of the results and, when it works effectively, it allows to find and correct flaws in the analytical process, which could lead to misleading findings. The collected results confirmed the reliability of the mutant cell lines for the generation of a valid RCM model.

4.2 Disease modeling with hiPSC-CMs of a novel *FLNC* missense mutation causative for RCM

The purpose of this study was the investigation of the effects of a novel *FLNC* missense mutation p.Glu2472_Asn2473delAsp discovered in a young patient of the Boston Children's Hospital affected by RCM. Experimental results support the hypothesis that the mutation is causative for the severe case of cardiomyopathy, as generated 2D and 3D models recapitulated the phenotype of the disease such as poor sarcomeres and myofibrillar disarray, as well as diminished force and arrhythmic events, respectively.

The RCM-causing mutation engineered in iPSCs impaired sarcomerogenesis *in vitro*. The structure of sarcomeres is among the most regular in myocytes and allows them to function as linear motors capable of highly coordinated, fast movements. Actin and myosin represent the classical contractile filaments of the sarcomere and are formed from self-assembly monomers [98]. The basics of sarcomere assembly are conserved between skeletal and cardiac muscle. α-actinin, the N-terminus of titin and actin filaments always form the first assembled complexes and, in developing embryonic heart, they are found in association with the plasma membrane of cardiomyocytes [99]. The giant protein titin spans half the sarcomere from M-band to Z-disc and is closely associated with myosin filaments. The organization of the C-termini of titin and the integration of thick filaments represents the next step in sarcomere assembly and it is achieved via the M-band protein myomesin, which crosslinks the elastic filament system and actin filaments. These components appear to play a role in the formation of a basic framework indispensable for sarcomere assembly, to integrate thin and thick filaments as well as the vast range of additional sarcomeric proteins

recently identified [98]. The maturation of thin filaments and the definition of their exact length comes after the initial assembly of sarcomeres. Nebulin plays a role in the regulation of actin filament length. This giant protein helps beyond the intrinsic self-assembly of actin and forms a contiguous α-helix closely associated with the filament. Nebulin is characterized by interaction sites for tropomodulin, desmin and CAPZ, suggesting its role in the coordination of thin-filament assembly and the integration of Z-discs with the intermediate filament system [100]–[102]. I-bands start to be visible as tropomodulin becomes integrated into the sarcomeres [99].

The subsequent steps include the lateral extension of Z-discs and the alignment of myofibrils. The myofibril acts a dynamic scaffold for sarcomere assembly and the induction of cardiac hypertrophy, hence the formation of new sarcomeres, is associated with an increase in the number of microtubules and their organization parallel to the myofibrillar axis [103]. In the embryonic heart, myofibrils assemble and disassemble continuously, as individual differentiated embryonic cardiomyocytes can still undergo division. In addition to molecular rulers titin and nebulin, other proteins of temporary importance and transient sarcomeric association are required for the formation of a myofibril [98].

A functional redundancy in the assembly of myofibrils seems to exist. This may be explained by the presence of different isoforms of sarcomeric proteins and the possibility that they may take over for the initial stages of sarcomere assembly. The delicate balance between the expression and localization of sarcomeric proteins is crucial for long-term maintenance, observation supported by data of mutations in sarcomeric proteins resulting in cardiomyopathies in humans [98].

The generated FLNC-mutant models showed an altered sarcomeric structure both in 2D and 3D. Although not statistically significant, sarcomere disarray analysis revealed a trend for increased myofibrillar disarray in mutant cell lines when compared to their isogenic control, which can also be deduced from the IF images showing α-actinin 2 (ACTN2) signals from both models. This result is in line with the findings of the study conducted by Begay *et al.*, where the morpholino knockdown of *FLNC* in zebrafish showed Z-discs abnormalities and altered distribution of junction proteins. The haploinsufficient *FLNC* model was characterized by interference with the desmosomal/cell-cell junction pathway leading to arrhythmogenic cardiomyopathy [43]. Diminished sarcomeric localization of mutant-FLNC causing an alteration of the protein's interactions with other sarcomeric components was also reported in one family affected by RCM caused by a *FLNC* mutation [45]. Future experiments would need to include a bigger sample size to validate these findings.

Remodeling of ACTN2, the only cardiac specific isoform of actinin, at the Z-disc has been associated with several cardiac diseases [104], [105]. Filamin and α-actinin 2 are involved in cell signaling though the connection of integrins to the cytoskeleton [106]. Even though there is no evidence of their direct interaction, they both simultaneously interact with actin – F-actin – through their two binding sites with similar association and dissociation rates and with no competition [107]. These proteins appear to promote F-actin function and regulate

cytoskeletal arrangements, forming orthogonal actin filament networks at low concentrations, while they induce the formation of bundles at higher concentrations [108]. WB analysis could potentially show this interaction, as results for both 2D and 3D disease modeling show bands at the same height (280 kDa) for FLNC and ACTN2, suggesting the proteins might interact at a sarcomeric level. However, the interpretation of the correct localization of FLNC in cells from both mutant lines and control is not straightforward and, therefore, further experiments such as co-immunoprecipitation would be needed to elucidate this hypothesis. In addition, fixation protocols, antibody specificity and ratios would need to be optimized.

Generated models from the heterozygous models showed hypertrophy at both 7 div and 30 div. Comparable results were found by Prondzynski *et al.* for hiPSC-CM-derived HCM models cultured for 30 div, where heterozygous HCM-mutant cells also had an area of approximately 5000 μm^2 [85]. Hypertrophic signaling seemed to be impaired for homozygous mutants between 7 div and 30 div. In fact, visual analysis from IF pictures and cell area analysis results show a decreased size at 30 div when compared to the control. Results from mRNA analysis of homozygous mutants at both timepoints exhibit an increased expression of proteins associated with hypertrophy such as the actin isoforms skeletal muscle α-actin (ACTA1), smooth muscle α-actin (ACTA2) and natriuretic peptides A and B (NPPA, NPPB) [109], [110].

RCM is characterized by rigid ventricular walls, which are causative for diastolic dysfunction of the heart and subsequent heart failure. As ventricular fibrosis has been linked to myocardial stiffness, the mRNA levels of proteins associated with fibrosis were investigated [111]. The mRNA expression analysis of collagen type 1 α-1 and collagen type 3 α-1 (COL1A1, COL3A1) in both FLNC-mutant models did not show significant changes. Nevertheless, WGA-stained cryosections of 32 div EHTs suggest the presence of fibrotic tissue [112]. This interpretation is supported by the strong signal from the WGA staining in correspondence with areas where no CMs are present; WGA has indeed been used to label fibrotic tissue after myocardial infarction in previous studies [113].

Alterations in hypertrophy can be causative for cardiac stress and are dependent from cellular metabolism, but also proliferation, non-coding RNAs, immune response, translational regulation and epigenetic modifications [114]. Cardiac remodeling is caused by cardiac stress and is characterized by morphological, structural and functional changes of the heart. Pathological remodeling is defined by the increased deposition of extracellular matrix proteins such as collagens and fibronectin and loss of cardiomyocytes by necrosis [115]. Necrosis is a type of cell death characterized by defective plasma and organelle membranes, cell swelling, severe ATP depletion and marked inflammation [116], [117]. Cell death by apoptosis, on the other hand, is accompanied by the rounding-up of the cell, retraction of pseudopods, pyknosis (reduction of cellular volume) and chromatin condensation followed up by karyorrhexis, or nuclear fragmentation [116]. However, biochemical studies of the apoptotic death receptor pathway showed that it can also signal

survival, necrosis, proliferation and inflammation [117]. Stainings of both 2D and 3D models show characteristics from both definitions. Alterations in multinucleation were seen in 2D, but EHTs in particular were characterized by a massive accumulation of nuclei. An upregulation in the expression of axin-related protein 2 (AXIN2) and lymphoid enhancer binding factor 1 (LEF1), regulators in the Wnt/β-catenin pathway, could be attributable to an increased cell cycle activity even though mRNA expression results were not statistically significant [118]. Interestingly, mRNA expression of histone H2 marker (H2FAX) for DNA damage and autophagy marker lysosome-associated membrane protein 2 (LAMP2) were downregulated in heterozygous mutant models. Several studies reported RCM phenotype characterized by protein aggregation, causing the weakening of myofibers [50], [52], [57], [59]. A suitable hypothesis for the effect of the heterozygous *FLNC* mutation at a sarcomeric level was given by Kley *et al.*: protein degradation strategies are activated by muscle fibers to cope with aggregation. However, proteosomal and autophagic degradation pathways decline with oxidative stress and mitochondrial alterations, triggering back aggregation and resulting in altered Z-disc protein homeostasis and focal myofibril destruction [40]. Hence, experiments for the validation of protein aggregation in the models can be performed in the future.

With the lack of cellular energy and chaperones, the sarcomere is in a locked state and, therefore, their involvement is essential in sarcomere assembly [104]. The calcium-regulated cysteine protease calpain-3 (CAPN3) is also implicated in myofibril assembly and has been shown to interact with FLNC. The proteolytic enzyme autolyzes and cleaves its substrate in response to exposure to calcium. In particular, the cleavage of FLNC by CAPN3 reduces its ability to interact with sarcoglycans at the sarcolemma [119]. Results from both FLNC-mutant models show that the downregulation of expression of genes encoding for sarcomeric proteins is accompanied by downregulation of CAPN3 translation, suggesting that cells are most likely undergoing extensive sarcomeric and cytoskeletal remodeling. Moreover, the insufficient calcium handling of the mutant models was reflected by the lower mRNA levels of the sarcoplasmic reticulum calcium ATPase 2 (ATP2A2) [120]. Conduction alterations and arrhythmia can be linked to calcium handling deficiencies and were visible in EHT models of the FLNC-mutant lines. Because of the fact that cardiomyocytes appeared to be isolated in islets throughout the tissue in heterozygous and homozygous models, reduced contraction force and frequency could be deriving from extracellular matrix degradation and cell death resulting in loss of cell to cell contact. This is contrast with EHT models generated from HCM-mutations, where heterozygous mutants generally showed a higher contraction force when compared to their isogenic controls [85]. Nevertheless, the used data acquisition and analysis methods represent a limitation of this project and would have to be improved for more accurate results in the future. Furthermore, these *in vitro* models might be able to model progressive heart failure, which is often observed in pediatric cases of RCM. Reduced ventricular function has been linked to the remodeling of sarcomeric proteins in cardiac diseases [104]. Hein *et al.* suggested that the transition from hypertrophy to heart failure occurs in two consecutive stages. The first, reversible stage involves an accumulation of

cytoskeletal proteins to cope with the increased strain on the myocardium. The second, irreversible stage is instead characterized by the loss of contractile filaments and crucial sarcomeric proteins such as α-actinin 2. The significant downregulation at 30 div in the heterozygous mutants of both genes encoding for the proteins might indicate that the models reached this second, irreversible stage, which characterizes heart failure. In line with this hypothesis, results also displayed a downregulation in the expression of the gene encoding for the thick filament myosin heavy chain 7 (MYH7).

The detachment of homozygous mutant EHT from the posts after 53 div suggests cell death, increased stiffness and consequent problems in conduction and could therefore represent a novel model of heart failure *in vitro*. However, certain aspects of RCM cannot be recapitulated or interpreted at this point from the model carrying the homozygous mutation due to the differences in gene and protein expression when compared to the heterozygous counterpart. As a matter of fact, such a mutation does not exist in nature and would probably be lethal at an embryonic stage as it was for the complete ablation of the protein in the mouse study conducted by Zhou *et al.* [39].

Understanding the mechanisms underlying the *FLNC* mutation-derived RCM and the different interactions of the proteins at a sarcomeric level is of great complexity. Yet, the generation of *in vitro* models such as the ones presented in this thesis aimed not only to assess the diseased phenotype, but also to elucidate the biology behind it.

4.3 Outlook

Myocardial disorders such as RCM are causative for heart failure or sudden cardiac death. Pharmacological treatment can be used to soften the pathology but does not target the genetic cause at the root of the disease. The technology of hiPSCs represents a very promising resource in particular for pediatric patients, as therapeutic approaches for RCM are limited.

The modeling of the novel *FLNC* mutation p.Glu2472_Asn2473delAsp using hiPSC-derived CMs helped to study underlying pathomechanism underlying RCM. The results presented in this thesis will potentially allow testing of novel therapeutic strategies to target the disease and ultimately help with the design of a personalized medicine for the patient carrying this mutation.

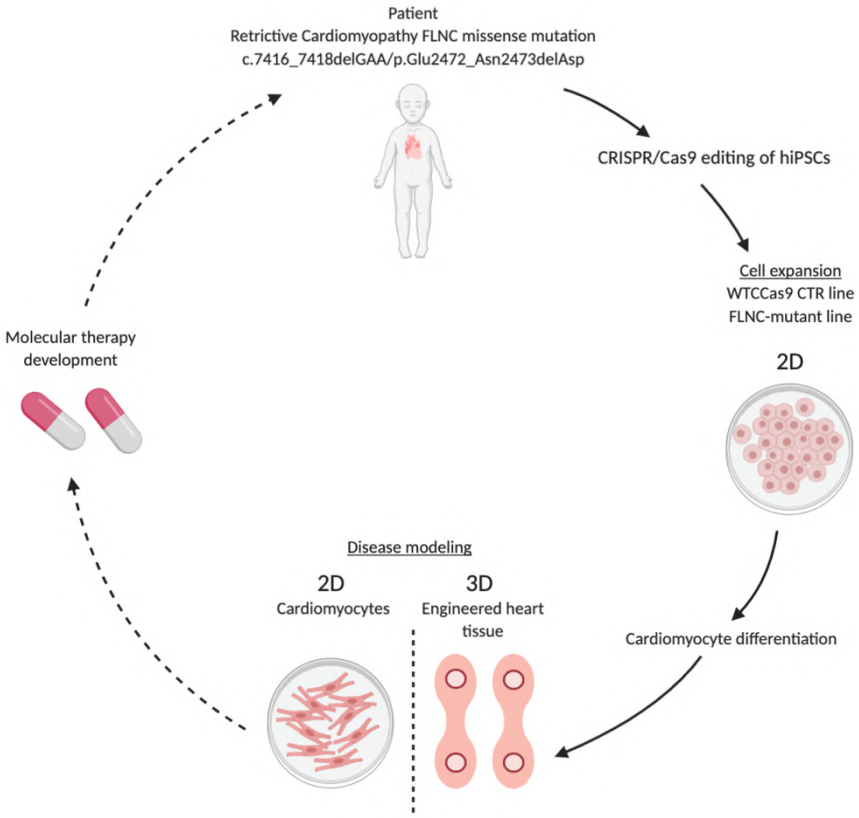

Figure 36. **Graphical abstract.** The figure depicts the workflow of the project and the potential use of results for the design of a personalized medicine for the patient carrying the RCM-causing mutation. Figure generated with *BioRender*.

Bibliography

[1] E. Muchtar, L. A. Blauwet, e M. A. Gertz, «Restrictive Cardiomyopathy: Genetics, Pathogenesis, Clinical Manifestations, Diagnosis, and Therapy», *Circ. Res.*, vol. 121, n. 7, pagg. 819–837, set. 2017, doi: 10.1161/CIRCRESAHA.117.310982.

[2] T. M. Lee *et al.*, «Pediatric Cardiomyopathies», *Circ. Res.*, vol. 121, n. 7, pagg. 855–873, set. 2017, doi: 10.1161/CIRCRESAHA.116.309386.

[3] S. E. Lipshultz, A. M. Lowe, P. R. Lurie, e J. E. Messere, «The Incidence of Pediatric Cardiomyopathy in Two Regions of the United States», *N. Engl. J. Med.*, pag. 9, 2003.

[4] A. W. Nugent, P. Chondros, J. B. Carlin, L. C. Wilkinson, C. W. Chow, e R. G. Weintraub, «The Epidemiology of Childhood Cardiomyopathy in Australia», *N. Engl. J. Med.*, pag. 8, 2003.

[5] S. E. Lipshultz *et al.*, «Cardiomyopathy in Children: Classification and Diagnosis: A Scientific Statement From the American Heart Association», *Circulation*, vol. 140, n. 1, lug. 2019, doi: 10.1161/CIR.0000000000000682.

[6] A. Arola *et al.*, «Epidemiology of Idiopathic Cardiomyopathies in Children and Adolescents: A Nationwide Study in Finland», *Am. J. Epidemiol.*, vol. 146, n. 5, pagg. 385–393, set. 1997, doi: 10.1093/oxfordjournals.aje.a009291.

[7] S. A. Webber *et al.*, «Outcomes of Restrictive Cardiomyopathy in Childhood and the Influence of Phenotype: A Report From the Pediatric Cardiomyopathy Registry», *Circulation*, vol. 126, n. 10, pagg. 1237–1244, set. 2012, doi: 10.1161/CIRCULATIONAHA.112.104638.

[8] S. S. Kushwaha, J. T. Fallon, e V. Fuster, «Restrictive Cardiomyopathy», *N. Engl. J. Med.*, vol. 336, n. 4, pagg. 267–276, gen. 1997, doi: 10.1056/NEJM199701233360407.

[9] Prondzynski, Gabbin et al., «Molecular Mechanism of Pediatric Restrictive Cardiomyopathies». Manuscript in preparation.

[10] «ACTC1 actin alpha cardiac muscle 1 [Homo sapiens (human)] - Gene - NCBI». https://www.ncbi.nlm.nih.gov/gene/70 (consultato apr. 27, 2020).

[11] «ACTN2 actinin alpha 2 [Homo sapiens (human)] - Gene - NCBI». https://www.ncbi.nlm.nih.gov/gene/88 (consultato ago. 18, 2020).

[12] «BAG3 BAG cochaperone 3 [Homo sapiens (human)] - Gene - NCBI». https://www.ncbi.nlm.nih.gov/gene/9531 (consultato ago. 18, 2020).

[13] «CRYAB crystallin alpha B [Homo sapiens (human)] - Gene - NCBI». https://www.ncbi.nlm.nih.gov/gene/1410 (consultato ago. 18, 2020).

[14] «DES desmin [Homo sapiens (human)] - Gene - NCBI». https://www.ncbi.nlm.nih.gov/gene/1674 (consultato apr. 27, 2020).

[15] «FLNC filamin C [Homo sapiens (human)] - Gene - NCBI». https://www.ncbi.nlm.nih.gov/gene/2318 (consultato ago. 18, 2020).

[16] «MYBPC3 myosin binding protein C3 [Homo sapiens (human)] - Gene - NCBI». https://www.ncbi.nlm.nih.gov/gene/4607 (consultato ago. 18, 2020).

[17] «MYH7 myosin heavy chain 7 [Homo sapiens (human)] - Gene - NCBI». https://www.ncbi.nlm.nih.gov/gene/4625 (consultato apr. 27, 2020).

[18] «MYH6 myosin heavy chain 6 [Homo sapiens (human)] - Gene - NCBI». https://www.ncbi.nlm.nih.gov/gene/4624 (consultato ago. 18, 2020).

[19] «MYL2 myosin light chain 2 [Homo sapiens (human)] - Gene - NCBI». https://www.ncbi.nlm.nih.gov/gene/4633 (consultato apr. 27, 2020).

[20] «MYL3 myosin light chain 3 [Homo sapiens (human)] - Gene - NCBI». https://www.ncbi.nlm.nih.gov/gene/4634 (consultato ago. 18, 2020).

[21] «MYPN myopalladin [Homo sapiens (human)] - Gene - NCBI». https://www.ncbi.nlm.nih.gov/gene/84665 (consultato ago. 18, 2020).

[22] «TMEM87B transmembrane protein 87B [Homo sapiens (human)] - Gene - NCBI». https://www.ncbi.nlm.nih.gov/gene/84910 (consultato ago. 18, 2020).

[23] «TNNC1 troponin C1, slow skeletal and cardiac type [Homo sapiens (human)] - Gene - NCBI». https://www.ncbi.nlm.nih.gov/gene/7134 (consultato ago. 18, 2020).

[24] «TNNI3 troponin I3, cardiac type [Homo sapiens (human)] - Gene - NCBI». https://www.ncbi.nlm.nih.gov/gene/7137#reference-sequences (consultato apr. 27, 2020).

[25] «TNNT2 troponin T2, cardiac type [Homo sapiens (human)] - Gene - NCBI».

https://www.ncbi.nlm.nih.gov/gene/7139 (consultato apr. 27, 2020).
[26] «TTN titin [Homo sapiens (human)] - Gene - NCBI». https://www.ncbi.nlm.nih.gov/gene/7273 (consultato ago. 18, 2020).
[27] «TPM1 tropomyosin 1 [Homo sapiens (human)] - Gene - NCBI». https://www.ncbi.nlm.nih.gov/gene/7168 (consultato ago. 18, 2020).
[28] «LMNA lamin A/C [Homo sapiens (human)] - Gene - NCBI». https://www.ncbi.nlm.nih.gov/gene/4000 (consultato apr. 27, 2020).
[29] «ABCC9 ATP binding cassette subfamily C member 9 [Homo sapiens (human)] - Gene - NCBI». https://www.ncbi.nlm.nih.gov/gene/10060 (consultato ago. 18, 2020).
[30] «CBL Cbl proto-oncogene [Homo sapiens (human)] - Gene - NCBI». https://www.ncbi.nlm.nih.gov/gene/867 (consultato ago. 18, 2020).
[31] «ADD3 adducin 3 [Homo sapiens (human)] - Gene - NCBI». https://www.ncbi.nlm.nih.gov/gene/120 (consultato ago. 18, 2020).
[32] «TTR transthyretin [Homo sapiens (human)] - Gene - NCBI». https://www.ncbi.nlm.nih.gov/gene/7276 (consultato apr. 27, 2020).
[33] S. W. Denfield e S. A. Webber, «Restrictive Cardiomyopathy in Childhood», *Heart Fail. Clin.*, vol. 6, n. 4, pagg. 445–452, ott. 2010, doi: 10.1016/j.hfc.2010.05.005.
[34] H. N. Anderson, F. Cetta, D. J. Driscoll, T. M. Olson, M. J. Ackerman, e J. N. Johnson, «Idiopathic Restrictive Cardiomyopathy in Children and Young Adults», *Am. J. Cardiol.*, vol. 121, n. 10, pagg. 1266–1270, mag. 2018, doi: 10.1016/j.amjcard.2018.01.045.
[35] M. Fujita *et al.*, «Filamin C plays an essential role in the maintenance of the structural integrity of cardiac and skeletal muscles, revealed by the medaka mutant zacro», *Dev. Biol.*, vol. 361, n. 1, pagg. 79–89, gen. 2012, doi: 10.1016/j.ydbio.2011.10.008.
[36] Z. Mao e F. Nakamura, «Structure and Function of Filamin C in the Muscle Z-Disc», *Int. J. Mol. Sci.*, vol. 21, n. 8, pag. 2696, apr. 2020, doi: 10.3390/ijms21082696.
[37] N. L. Pereira, M. Grogan, e G. W. Dec, «Spectrum of Restrictive and Infiltrative Cardiomyopathies», *J. Am. Coll. Cardiol.*, vol. 71, n. 10, pagg. 1149–1166, mar. 2018, doi: 10.1016/j.jacc.2018.01.017.
[38] D. O. Fürst, L. G. Goldfarb, R. A. Kley, M. Vorgerd, M. Olivé, e P. F. M. van der Ven, «Filamin C-related myopathies: pathology and mechanisms», *Acta Neuropathol. (Berl.)*, vol. 125, n. 1, pagg. 33–46, gen. 2013, doi: 10.1007/s00401-012-1054-9.
[39] Y. Zhou *et al.*, «Loss of Filamin C Is Catastrophic for Heart Function», *Circulation*, vol. 141, n. 10, pagg. 869–871, mar. 2020, doi: 10.1161/CIRCULATIONAHA.119.044061.
[40] R. A. Kley *et al.*, «Pathophysiology of protein aggregation and extended phenotyping in filaminopathy», *Brain*, vol. 135, n. 9, pagg. 2642–2660, set. 2012, doi: 10.1093/brain/aws200.
[41] G. H. Reference, «Myofibrillar myopathy», *Genetics Home Reference*. https://ghr.nlm.nih.gov/condition/myofibrillar-myopathy (consultato apr. 13, 2020).
[42] A. Brodehl *et al.*, «Mutations in *FLNC* are Associated with Familial Restrictive Cardiomyopathy», *Hum. Mutat.*, vol. 37, n. 3, pagg. 269–279, mar. 2016, doi: 10.1002/humu.22942.
[43] R. L. Begay *et al.*, «Filamin C Truncation Mutations Are Associated With Arrhythmogenic Dilated Cardiomyopathy and Changes in the Cell–Cell Adhesion Structures», *JACC Clin. Electrophysiol.*, vol. 4, n. 4, pagg. 504–514, apr. 2018, doi: 10.1016/j.jacep.2017.12.003.
[44] D. O. Fürst, L. G. Goldfarb, R. A. Kley, M. Vorgerd, M. Olivé, e P. F. M. van der Ven, «Filamin C-related myopathies: pathology and mechanisms», *Acta Neuropathol. (Berl.)*, vol. 125, n. 1, pagg. 33–46, gen. 2013, doi: 10.1007/s00401-012-1054-9.
[45] Tucker Nathan R. *et al.*, «Novel Mutation in FLNC (Filamin C) Causes Familial Restrictive Cardiomyopathy», *Circ. Cardiovasc. Genet.*, vol. 10, n. 6, pag. e001780, dic. 2017, doi: 10.1161/CIRCGENETICS.117.001780.
[46] F. Ader *et al.*, «*FLNC* pathogenic variants in patients with cardiomyopathies: Prevalence and genotype-phenotype correlations», *Clin. Genet.*, vol. 96, n. 4, pagg. 317–329, ott. 2019, doi: 10.1111/cge.13594.
[47] R. Valdés-Mas *et al.*, «Mutations in filamin C cause a new form of familial hypertrophic cardiomyopathy», *Nat. Commun.*, vol. 5, n. 1, pag. 5326, dic. 2014, doi: 10.1038/ncomms6326.
[48] J. R. Golbus *et al.*, «Targeted Analysis of Whole Genome Sequence Data to Diagnose Genetic Cardiomyopathy», *Circ. Cardiovasc. Genet.*, vol. 7, n. 6, pagg. 751–759, dic. 2014,

doi: 10.1161/CIRCGENETICS.113.000578.
[49] T. Löwe *et al.*, «The pathomechanism of filaminopathy: altered biochemical properties explain the cellular phenotype of a protein aggregation myopathy», *Hum. Mol. Genet.*, vol. 16, n. 11, pagg. 1351–1358, giu. 2007, doi: 10.1093/hmg/ddm085.
[50] J. Schubert, M. Tariq, G. Geddes, S. Kindel, E. M. Miller, e S. M. Ware, «Novel pathogenic variants in filamin C identified in pediatric restrictive cardiomyopathy», *Hum. Mutat.*, vol. 39, n. 12, pagg. 2083–2096, dic. 2018, doi: 10.1002/humu.23661.
[51] A. Brodehl *et al.*, «Mutations in FLNC are Associated with Familial Restrictive Cardiomyopathy», *Hum. Mutat.*, vol. 37, n. 3, pagg. 269–279, 2016, doi: 10.1002/humu.22942.
[52] A. Kiselev *et al.*, «De novo mutations in FLNC leading to early-onset restrictive cardiomyopathy and congenital myopathy», *Hum. Mutat.*, vol. 39, n. 9, pagg. 1161–1172, 2018, doi: 10.1002/humu.23559.
[53] F. Xiao *et al.*, «Clinical exome sequencing revealed that FLNC variants contribute to the early diagnosis of cardiomyopathies in infant patients», *Transl. Pediatr.*, vol. 9, n. 1, pagg. 21–33, feb. 2020, doi: 10.21037/tp.2019.12.02.
[54] A. Roldán-Sevilla *et al.*, «Missense Mutations in the *FLNC* Gene Causing Familial Restrictive Cardiomyopathy: Growing Evidence», *Circ. Genomic Precis. Med.*, vol. 12, n. 3, mar. 2019, doi: 10.1161/CIRCGEN.118.002388.
[55] H.-C. H. Lee *et al.*, «Clinical and pathological characterization of FLNC-related myofibrillar myopathy caused by founder variant c.8129G>A in Hong Kong Chinese», *Clin. Genet.*, vol. 97, n. 5, pagg. 747–757, 2020, doi: 10.1111/cge.13715.
[56] A. J. Sanoja, H. Li, F. J. Fricker, S. F. Kingsmore, e M. R. Wallace, «Exome sequencing identifies FLNC and ADD3 variants in a family with cardiomyopathy», *J. Transl. Genet. Genomics*, 2018, doi: 10.20517/jtgg.2017.13.
[57] J. I. van Waning *et al.*, «FLNC missense variants in familial noncompaction cardiomyopathy», *Cardiogenetics*, vol. 9, n. 1, Art. n. 1, ott. 2019, doi: 10.4081/cardiogenetics.2019.8181.
[58] M. F. Ortiz-Genga *et al.*, «Truncating FLNC Mutations Are Associated With High-Risk Dilated and Arrhythmogenic Cardiomyopathies», *J. Am. Coll. Cardiol.*, vol. 68, n. 22, pagg. 2440–2451, dic. 2016, doi: 10.1016/j.jacc.2016.09.927.
[59] I. Dalkilic, J. Schienda, T. G. Thompson, e L. M. Kunkel, «Loss of FilaminC (FLNc) Results in Severe Defects in Myogenesis and Myotube Structure», *Mol. Cell. Biol.*, vol. 26, n. 17, pagg. 6522–6534, set. 2006, doi: 10.1128/MCB.00243-06.
[60] Y. Leber *et al.*, «Filamin C is a highly dynamic protein associated with fast repair of myofibrillar microdamage», *Hum. Mol. Genet.*, vol. 25, n. 13, pagg. 2776–2788, lug. 2016, doi: 10.1093/hmg/ddw135.
[61] S. F. Gilbert e S. F. Gilbert, *Developmental Biology*, 6th ed. Sinauer Associates, 2000.
[62] K. Tanabe, K. Takahashi, e S. Yamanaka, «Induction of pluripotency by defined factors», *Proc. Jpn. Acad. Ser. B*, vol. 90, n. 3, pagg. 83–96, 2014, doi: 10.2183/pjab.90.83.
[63] H. Spemann, *Embryonic development and induction,*. New Haven, London: Yale University Press; HMilford, Oxford University Press, 1938.
[64] R. Briggs e T. J. King, «Transplantation of living nuclei from blastula cells into enucleated frogs' eggs», *Proc. Natl. Acad. Sci.*, vol. 38, n. 5, pagg. 455–463, mag. 1952, doi: 10.1073/pnas.38.5.455.
[65] J. B. Gurdon, «The Developmental Capacity of Nuclei taken from Intestinal Epithelium Cells of Feeding Tadpoles», pag. 20.
[66] I. Wilmut, A. E. Schnieke, J. McWhir, A. J. Kind, e K. H. S. Campbell, «Viable offspring derived from fetal and adult mammalian cells», *Nature*, vol. 385, n. 6619, pagg. 810–813, feb. 1997, doi: 10.1038/385810a0.
[67] «1544.full.pdf». Consultato: mag. 13, 2020. [In linea]. Available at: https://cancerres.aacrjournals.org/content/canres/24/9/1544.full.pdf.
[68] V. E. Papaioannou, R. L. Gardner, M. W. McBURNEY, C. Babinet, e M. J. Evans, «Participation of cultured teratocarcinoma cells in mouse embryogenesis», pag. 12.
[69] M. J. Evans e M. H. Kaufman, «Establishment in culture of pluripotential cells from mouse embryos», *Nature*, vol. 292, n. 5819, pagg. 154–156, lug. 1981, doi: 10.1038/292154a0.
[70] Y. Matsui, K. Zsebo, e B. L. Hogan, «Derivation of pluripotential embryonic stem cells from murine primordial germ cells in culture», *Cell*, vol. 70, n. 5, pagg. 841–847, set. 1992, doi:

10.1016/0092-8674(92)90317-6.
[71] K. Takahashi *et al.*, «Induction of Pluripotent Stem Cells from Adult Human Fibroblasts by Defined Factors», *Cell*, vol. 131, n. 5, pagg. 861–872, nov. 2007, doi: 10.1016/j.cell.2007.11.019.
[72] A. Brodehl *et al.*, «Human Induced Pluripotent Stem-Cell-Derived Cardiomyocytes as Models for Genetic Cardiomyopathies», *Int. J. Mol. Sci.*, vol. 20, n. 18, pag. 4381, set. 2019, doi: 10.3390/ijms20184381.
[73] G. Lee *et al.*, «Modelling pathogenesis and treatment of familial dysautonomia using patient-specific iPSCs», *Nature*, vol. 461, n. 7262, pagg. 402–406, set. 2009, doi: 10.1038/nature08320.
[74] D. Mosqueira *et al.*, «CRISPR/Cas9 editing in human pluripotent stem cell-cardiomyocytes highlights arrhythmias, hypocontractility, and energy depletion as potential therapeutic targets for hypertrophic cardiomyopathy», *Eur. Heart J.*, vol. 39, n. 43, pagg. 3879–3892, nov. 2018, doi: 10.1093/eurheartj/ehy249.
[75] W. C. Claycomb *et al.*, «HL-1 cells: A cardiac muscle cell line that contracts and retains phenotypic characteristics of the adult cardiomyocyte», *Proc. Natl. Acad. Sci.*, vol. 95, n. 6, pagg. 2979–2984, mar. 1998, doi: 10.1073/pnas.95.6.2979.
[76] J. Zhang *et al.*, «Functional Cardiomyocytes Derived From Human Induced Pluripotent Stem Cells», *Circ. Res.*, vol. 104, n. 4, feb. 2009, doi: 10.1161/CIRCRESAHA.108.192237.
[77] C. L. Mummery, J. Zhang, E. S. Ng, D. A. Elliott, A. G. Elefanty, e T. J. Kamp, «Differentiation of Human ES and iPS Cells to Cardiomyocytes: A Methods Overview», *Circ. Res.*, vol. 111, n. 3, pagg. 344–358, lug. 2012, doi: 10.1161/CIRCRESAHA.110.227512.
[78] R. R. Besser, M. Ishahak, V. Mayo, D. Carbonero, I. Claure, e A. Agarwal, «Engineered Microenvironments for Maturation of Stem Cell Derived Cardiac Myocytes», *Theranostics*, vol. 8, n. 1, pagg. 124–140, gen. 2018, doi: 10.7150/thno.19441.
[79] A. Sharma, G. Li, K. Rajarajan, R. Hamaguchi, P. W. Burridge, e S. M. Wu, «Derivation of Highly Purified Cardiomyocytes from Human Induced Pluripotent Stem Cells Using Small Molecule-modulated Differentiation and Subsequent Glucose Starvation», *J. Vis. Exp. JoVE*, n. 97, mar. 2015, doi: 10.3791/52628.
[80] M. Vorgerd *et al.*, «A Mutation in the Dimerization Domain of Filamin C Causes a Novel Type of Autosomal Dominant Myofibrillar Myopathy», *Am. J. Hum. Genet.*, vol. 77, n. 2, pagg. 297–304, ago. 2005, doi: 10.1086/431959.
[81] «GM25256». https://www.coriell.org/0/Sections/Search/Sample_Detail.aspx?Ref=GM25256 (consultato mar. 19, 2020).
[82] K. Ban, S. Bae, e Y. Yoon, «Current Strategies and Challenges for Purification of Cardiomyocytes Derived from Human Pluripotent Stem Cells», *Theranostics*, vol. 7, n. 7, pagg. 2067–2077, mag. 2017, doi: 10.7150/thno.19427.
[83] «f9d805bc-c242-4f4a-b401-260a60900a67.pdf». Consultato: ago. 17, 2020. [In linea]. Available at: http://investors.nanostring.com/static-files/f9d805bc-c242-4f4a-b401-260a60900a67.
[84] K. Breckwoldt *et al.*, «Differentiation of cardiomyocytes and generation of human engineered heart tissue», *Nat. Protoc.*, vol. 12, n. 6, pagg. 1177–1197, giu. 2017, doi: 10.1038/nprot.2017.033.
[85] M. Prondzynski *et al.*, «Disease modeling of a mutation in α-actinin 2 guides clinical therapy in hypertrophic cardiomyopathy», *EMBO Mol. Med.*, vol. 11, n. 12, dic. 2019, doi: 10.15252/emmm.201911115.
[86] M. Prondzynski *et al.*, «Evaluation of MYBPC3 trans -Splicing and Gene Replacement as Therapeutic Options in Human iPSC-Derived Cardiomyocytes», *Mol. Ther. - Nucleic Acids*, vol. 7, pagg. 475–486, giu. 2017, doi: 10.1016/j.omtn.2017.05.008.
[87] «trizol_reagent.pdf». Consultato: ago. 19, 2020. [In linea]. Available at: https://assets.thermofisher.com/TFS-Assets/LSG/manuals/trizol_reagent.pdf.
[88] «superscript_firststrand_qrtpcr_man.pdf». Consultato: ago. 19, 2020. [In linea]. Available at: https://assets.thermofisher.com/TFS-Assets/LSG/manuals/superscript_firststrand_qrtpcr_man.pdf.
[89] X. Lian *et al.*, «Cozzarelli Prize Winner: Robust cardiomyocyte differentiation from human pluripotent stem cells via temporal modulation of canonical Wnt signaling», *Proc. Natl. Acad. Sci.*, vol. 109, n. 27, pagg. E1848–E1857, lug. 2012, doi: 10.1073/pnas.1200250109.
[90] S. J. Kattman *et al.*, «Stage-Specific Optimization of Activin/Nodal and BMP Signaling

Promotes Cardiac Differentiation of Mouse and Human Pluripotent Stem Cell Lines», *Cell Stem Cell*, vol. 8, n. 2, pagg. 228–240, feb. 2011, doi: 10.1016/j.stem.2010.12.008.
[91] M. X. Doss e A. Sachinidis, «Current Challenges of iPSC-Based Disease Modeling and Therapeutic Implications», *Cells*, vol. 8, n. 5, apr. 2019, doi: 10.3390/cells8050403.
[92] K. Kim *et al.*, «Epigenetic memory in induced pluripotent stem cells», *Nature*, vol. 467, n. 7313, pagg. 285–290, set. 2010, doi: 10.1038/nature09342.
[93] K. Kim *et al.*, «Donor cell type can influence the epigenome and differentiation potential of human induced pluripotent stem cells», *Nat. Biotechnol.*, vol. 29, n. 12, pagg. 1117–1119, nov. 2011, doi: 10.1038/nbt.2052.
[94] M. J. Boland, K. L. Nazor, e J. F. Loring, «Epigenetic Regulation of Pluripotency and Differentiation», *Circ. Res.*, vol. 115, n. 2, pagg. 311–324, lug. 2014, doi: 10.1161/CIRCRESAHA.115.301517.
[95] K. Nishino *et al.*, «DNA Methylation Dynamics in Human Induced Pluripotent Stem Cells over Time», *PLoS Genet.*, vol. 7, n. 5, mag. 2011, doi: 10.1371/journal.pgen.1002085.
[96] V. L. Sardo, W. Ferguson, G. A. Erikson, E. J. Topol, K. K. Baldwin, e A. Torkamani, «The effect of aging on human induced pluripotent stem cells», *Nat. Biotechnol.*, vol. 35, n. 1, pagg. 69–74, gen. 2017, doi: 10.1038/nbt.3749.
[97] A. C. Komor, Y. B. Kim, M. S. Packer, J. A. Zuris, e D. R. Liu, «Programmable editing of a target base in genomic DNA without double-stranded DNA cleavage», *Nature*, vol. 533, n. 7603, pagg. 420–424, mag. 2016, doi: 10.1038/nature17946.
[98] E. Ehler e M. Gautel, «The Sarcomere and Sarcomerogenesis», in *The Sarcomere and Skeletal Muscle Disease*, vol. 642, N. G. Laing, A c. di New York, NY: Springer New York, 2008, pagg. 1–14.
[99] E. Ehler, «Chicken heart myofibrillogenesis», pag. 11.
[100] A. S. McElhinny, B. Kolmerer, V. M. Fowler, S. Labeit, e C. C. Gregorio, «The N-terminal End of Nebulin Interacts with Tropomodulin at the Pointed Ends of the Thin Filaments», *J. Biol. Chem.*, vol. 276, n. 1, pagg. 583–592, gen. 2001, doi: 10.1074/jbc.M005693200.
[101] M.-L. Bang, C. Gregorio, e S. Labeit, «Molecular Dissection of the Interaction of Desmin with the C-Terminal Region of Nebulin», *J. Struct. Biol.*, vol. 137, n. 1–2, pagg. 119–127, gen. 2002, doi: 10.1006/jsbi.2002.4457.
[102] C. C. Witt *et al.*, «Nebulin regulates thin filament length, contractility, and Z-disk structure in vivo», *EMBO J.*, vol. 25, n. 16, pagg. 3843–3855, ago. 2006, doi: 10.1038/sj.emboj.7601242.
[103] L. Rappaport *et al.*, «Isomyosins, microtubules and desmin during the onset of cardiac hypertrophy in the rat», *Eur. Heart J.*, vol. 5, n. suppl F, pagg. 243–250, dic. 1984, doi: 10.1093/eurheartj/5.suppl_F.243.
[104] S. Hein, «The role of the cytoskeleton in heart failure», *Cardiovasc. Res.*, vol. 45, n. 2, pagg. 273–278, gen. 2000, doi: 10.1016/S0008-6363(99)00268-0.
[105] J. G. Lichter *et al.*, «Remodeling of the Sarcomeric Cytoskeleton in Cardiac Ventricular Myocytes during Heart Failure and after Cardiac Resynchronization Therapy», *J. Mol. Cell. Cardiol.*, vol. 72, pagg. 186–195, lug. 2014, doi: 10.1016/j.yjmcc.2014.03.012.
[106] T. Kiema *et al.*, «The Molecular Basis of Filamin Binding to Integrins and Competition with Talin», *Mol. Cell*, vol. 21, n. 3, pagg. 337–347, feb. 2006, doi: 10.1016/j.molcel.2006.01.011.
[107] W. H. Goldmann e G. Isenberg, «Analysis of filamin and a-actinin binding to actin by the stopped flow method», vol. 336, n. 3, pag. 3, 1993.
[108] O. Esue, Y. Tseng, e D. Wirtz, «α-Actinin and Filamin Cooperatively Enhance the Stiffness of Actin Filament Networks», *PLoS ONE*, vol. 4, n. 2, feb. 2009, doi: 10.1371/journal.pone.0004411.
[109] L. C. Boraas, J. B. Guidry, E. T. Pineda, e T. Ahsan, «Cytoskeletal Expression and Remodeling in Pluripotent Stem Cells», *PLOS ONE*, vol. 11, n. 1, pag. e0145084, gen. 2016, doi: 10.1371/journal.pone.0145084.
[110] J. L. Januzzi, «Natriuretic Peptides as Biomarkers in Heart Failure», *J. Investig. Med. Off. Publ. Am. Fed. Clin. Res.*, vol. 61, n. 6, pagg. 950–955, ago. 2013, doi: 10.231/JIM.0b013e3182946b69.
[111] K. Yamamoto, «Myocardial stiffness is determined by ventricular fibrosis, but not by compensatory or excessive hypertrophy in hypertensive heart», *Cardiovasc. Res.*, vol. 55, n. 1, pagg. 76–82, lug. 2002, doi: 10.1016/S0008-6363(02)00341-3.
[112] L. E. Felkin, E. Lara-Pezzi, R. George, M. H. Yacoub, E. J. Birks, e P. J. R. Barton,

«Expression of Extracellular Matrix Genes During Myocardial Recovery From Heart Failure After Left Ventricular Assist Device Support», *J. Heart Lung Transplant.*, vol. 28, n. 2, pagg. 117–122, feb. 2009, doi: 10.1016/j.healun.2008.11.910.

[113] B. Emde, A. Heinen, A. Gödecke, e K. Bottermann, «Wheat Germ Agglutinin Staining as a Suitable Method for Detection and Quantification of Fibrosis in Cardiac Tissue after Myocardial Infarction», *Eur. J. Histochem. EJH*, vol. 58, n. 4, dic. 2014, doi: 10.4081/ejh.2014.2448.

[114] M. Nakamura e J. Sadoshima, «Mechanisms of physiological and pathological cardiac hypertrophy», *Nat. Rev. Cardiol.*, vol. 15, n. 7, pagg. 387–407, lug. 2018, doi: 10.1038/s41569-018-0007-y.

[115] A. Piek, R. A. de Boer, e H. H. W. Silljé, «The fibrosis-cell death axis in heart failure», *Heart Fail. Rev.*, vol. 21, pagg. 199–211, 2016, doi: 10.1007/s10741-016-9536-9.

[116] G. Kroemer *et al.*, «Classification of cell death», *Cell Death Differ.*, vol. 16, n. 1, pagg. 3–11, gen. 2009, doi: 10.1038/cdd.2008.150.

[117] G. Kung, K. Konstantinidis, e R. N. Kitsis, «Programmed Necrosis, Not Apoptosis, in the Heart», *Circ. Res.*, vol. 108, n. 8, pagg. 1017–1036, apr. 2011, doi: 10.1161/CIRCRESAHA.110.225730.

[118] Y. Fan *et al.*, «Wnt/β-catenin-mediated signaling re-activates proliferation of matured cardiomyocytes», *Stem Cell Res. Ther.*, vol. 9, dic. 2018, doi: 10.1186/s13287-018-1086-8.

[119] J. R. Guyon *et al.*, «Calpain 3 cleaves filamin C and regulates its ability to interact with γ- and δ-sarcoglycans», *Muscle Nerve*, vol. 28, n. 4, pagg. 472–483, 2003, doi: 10.1002/mus.10465.

[120] L. Lipskaia, E. R. Chemaly, L. Hadri, A.-M. Lompre, e R. J. Hajjar, «Sarcoplasmic reticulum Ca2+ ATPase as a therapeutic target for heart failure», *Expert Opin. Biol. Ther.*, vol. 10, n. 1, pagg. 29–41, gen. 2010, doi: 10.1517/14712590903321462.

List of Figures

List of Tables

List of Abbreviations

2D	Two-dimensional
3D	Three-dimensional
A	Atrial filling velocity
ABLP	Actin-binding-like protein
ACTA1	Skeletal muscle α-actin
ACTA2	Smooth muscle α-actin
ACTN2	α-actinin 2
ANOVA	Analysis of variance
ATP2A2	Sarcoplasmic reticulum calcium ATPase 2
a.u.	Arbitrary unit
AXIN2	Axin-related protein 2
BDM	2,3-butanedione 2-monoxime
BMP	Bone morphogenetic proteins
bp	Base pair
BSA	Bovine serum albumin
BTS	N-benzyl-p-toulene sulphonamide
CAPN3	Calpain 3
cDNA	Complementary DNA
CM	Cardiomyocyte
CMR	Cardiac magnetic resonance imaging
COL1A1	Collagen type 1 α-1
COL3A1	Collagen type 3 α-1
CRISPR	Clustered regularly interspaced short palindromic repeat
CRISPR/Cas9	Clustered regularly interspaced short palindromic repeat associated protein 9
cTnT	Cardiac troponin T
DCM	Dilated cardiomyopathy
div	Days *in vitro*
DTI	Doppler tissue imaging
E	Diastolic filling velocity
ECC	Embryonal carcinoma cell
EGC	Embryonic germ cell
ESC	Embryonic stem cell
EB	Embryoid body
EHT	Engineered heart tissue
FACS	Fluorescence-activated cell sorting
FGF	Fibroblast growth factor
FLN2	Filamin-2
FLNC	Filamin-C
fps	Frames per second
IF	Immunofluorescence
iPSC	Induced pluripotent stem cell
iRCM	Idiopathic restrictive cardiomyopathy
H2FAX	Histone H2 variant
HCM	Hypertrophic cardiomyopathy
hiPSC	Human induced pluripotent stem cell
LAMP2	Lysosome-associated membrane protein 2
LEF1	Lymphoid enhancer binding factor 1
MEF2	Myocyte enhancer factor 2
Mesp1	Transcription factor mesoderm posterior 1
MFM	Myofibrillar myopathy
MYH7	Myosin heavy chain 7
NGS	Next-generation sequencing
NPPA	Natriuretic peptide A

NPPB	Natriuretic peptide B
PCR	Polymerase chain reaction
qPCR	Quantitative polymerase chain reaction
PFA	Paraformaldehyde
PGC	Primordial germ cell
RCM	Restrictive cardiomyopathy
ROI	Region of interest
rpm	Rotation per minute
SCD	Sudden cardiac death
SD	Standard deviation
SNP	Single-nucleotide polymorphism
sgRNA	Single guide RNA
SRF	Serum response factor
T	T-box factor Brachyury
TAE	Tris-acetate-EDTA
TALEN	Transcription activator-like effector nuclease
WB	Western blot
Wnt	Wingless and Int-1
WT	Wild type
WTC	WTC-11
XIRP	Xin actin-binding repeat protein

A: FLNC-mutant CRISPR lines

A.1 FLNC homozygous mutants

FLNC Hom.

Gene	Peptide seq.	mRNA	Pathology
FLNC	p.Glu2472_Asn2473DelInsAsp	c.7416_7418delGAA	RCM

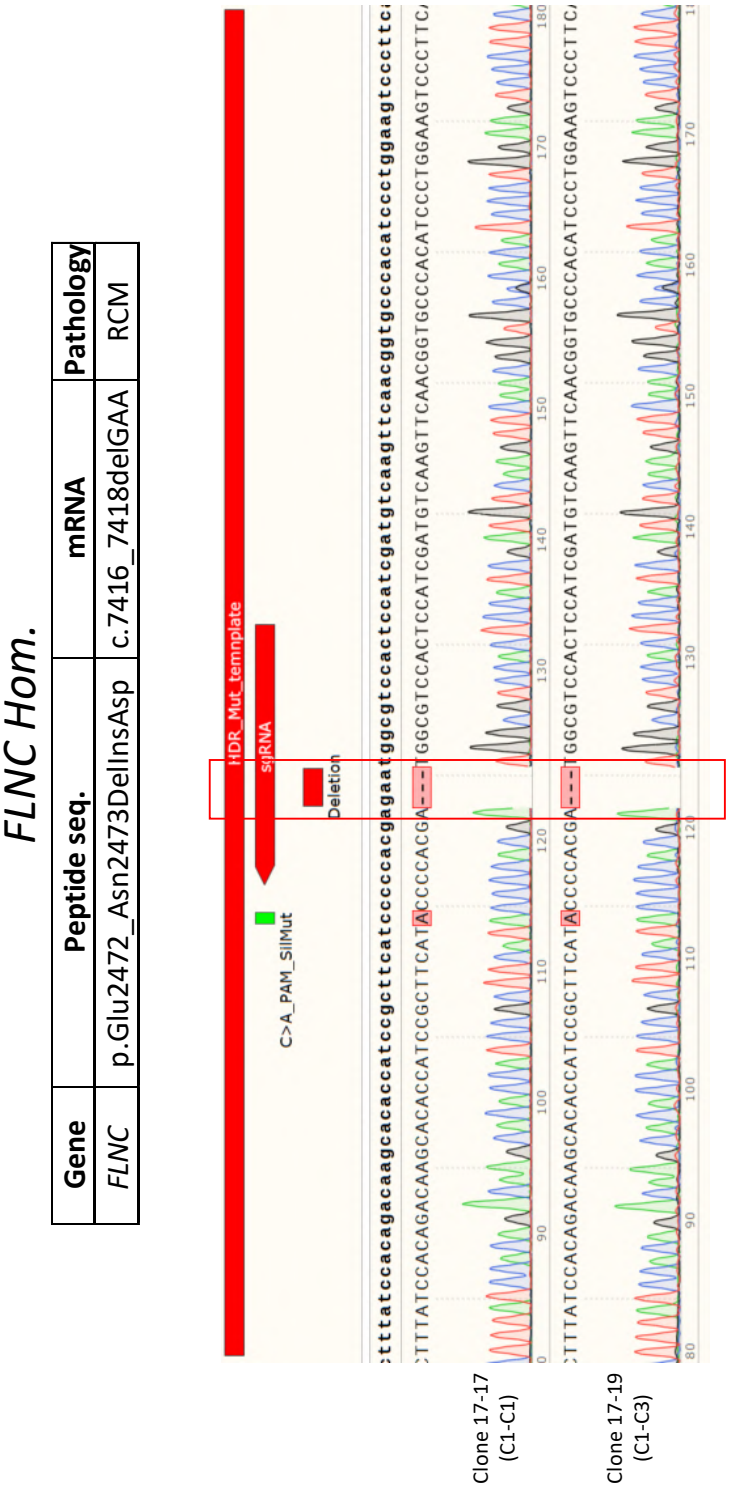

A.2 FLNC heterozygous mutants

FLNC Het.

Gene	Peptide seq.	mRNA	Pathology
FLNC	p.Glu2472_Asn2473DelInsAsp	c.7416_7418delGAA	RCM

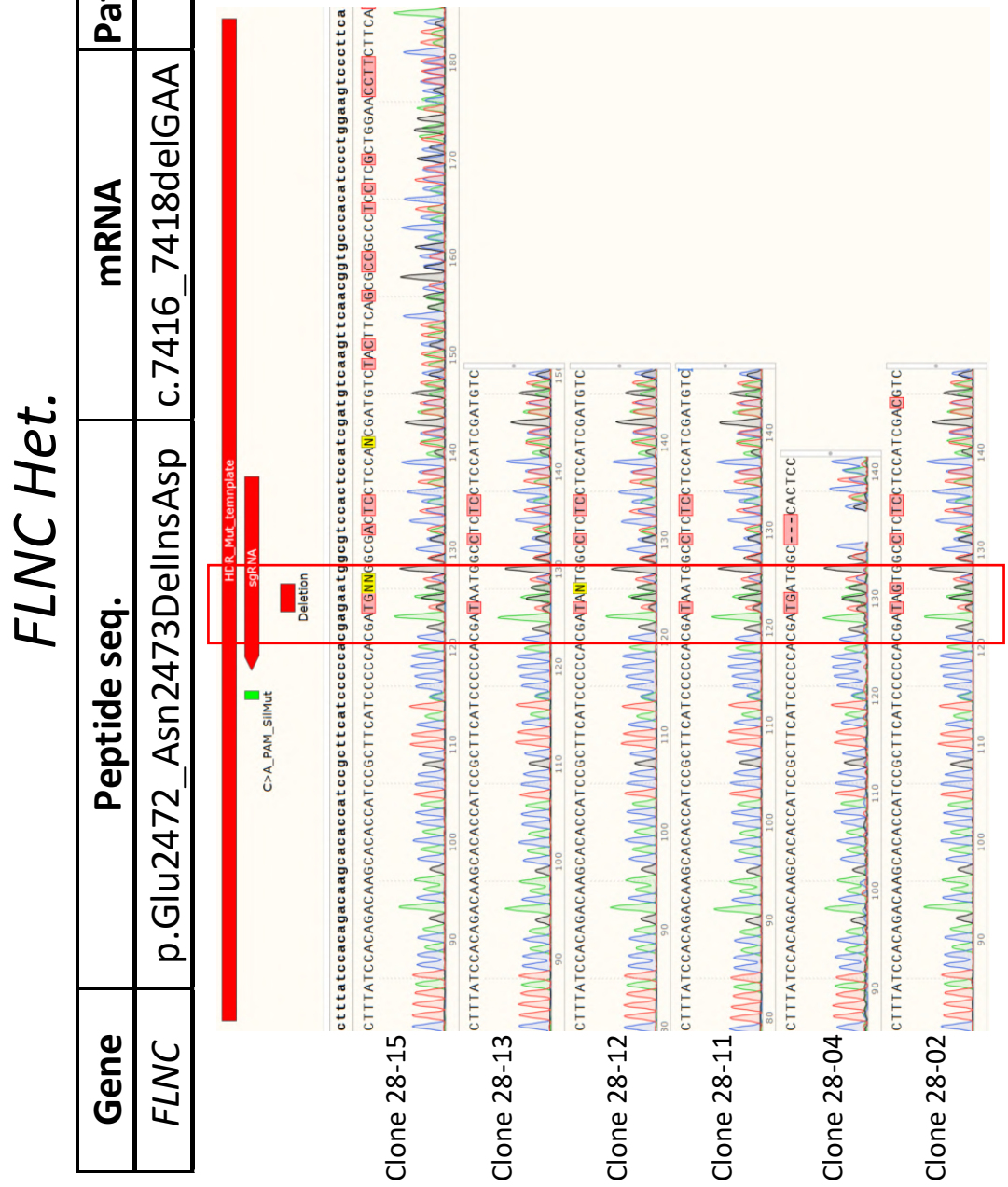

B: Primers

Number	Primers	5'-3'	Fragment size
22	FLNC_for_genomic	ctcccaggagtctgagcatc	779 bp
23	FLNC_rev_genomic	ggggccatgggagtataagt	
26	FLNC_for_genomic_II	tgctacgtctctgagctgga	666 bp
27	FLNC_rev_genomic_II	caccgtacttgatggcaatg	
34	FLNC_for_amplicon	ACACTCTTTCCCTACACGACGCTCTTCCGATCTtgctacgtctctgagctgga	411 bp
35	FLNC_rev_amplicon	GACTGGAGTTCAGACGTGTGCTCTTCCGATCTtctgtggggactcctggctt	
1	FLNC_for_Off1_deletion	gccagtgggaaatagctgtc	359 bp
2	FLNC_rev_Off1_deletion	ctttacctggggtttgggta	
3	FLNC_for_Off2_deletion	cgaggtgtccatcaagttca	472 bp
4	FLNC_rev_Off2_deletion	taatgtccctggacctgctc	
5	FLNC_for_Off3_deletion	ctgcagaaggctatcagatgaa	503 bp
6	FLNC_rev_Off3_deletion	ttggtgtctgtctcgtggaa	
41	hACTN2_for_ex7	GCCATGGAAATCGCTGAGAA	164 bp
42	hACTN2_rev_ex9	ATCCTGTTAGCCGCTGTCTC	
43	hGAPDH_for_ex5	ATGTTCGTCATGGGTGTGAA	136 bp
44	hGAPDH_rev_ex6	TGAGTCCTTCCACGATACCA	
47	CAPN3_for_ex1	ggaaacccaagtggcatcta	134 bp
48	CAPN3_rev_ex1	gggaactcagggtccacata	
49	AXIN2_for_ex1	caaacccatgcctgtctctt	162 bp
50	AXIN2_rev_ex1	tccaggaaagttcggaacag	
51	Lef1_for_ex1	gacgagatgatccccttcaa	187 bp
52	Lef1_rev_ex1	agggctcctgagaggtttgt	
53	H2AFX_for	tacctcaccgctgagatcct	168 bp
54	H2AFX_rev	ctggatgttgggcaggac	
57	COL1A1_for	aagaggaaggccaagtcgag	156 bp
58	COL1A1_rev	agatcacgtcatcgcacaac	
59	COL3A1_for	aggggagctggctacttctc	159 bp
60	COL3A1_rev	cggatcctgagtcacagaca	
66	hNPPA_for	GCTGCTTCGGGGGCAGGATG	153 bp
67	hNPPA_rev	TGCAGCAGAGACCCCAGGGG	
68	hNPPB_for	TGCAAGGGTCTGGCTGCTTTGG	165 bp
69	hNPPB_rev	CACTTCAAAGGCGGCCACAGGG	
70	hACTA1_for	AGCAGTTGTAGCTACCCGCCCA	176 bp
71	hACTA1_rev	GACCATGACGCCCTGGTGTCG	
72	hMYH7_for_ex1	GCTCTGTGTCTTTCCCTGCTGCTC	159 bp
73	hMYH7_rev_ex3	GCTCCTTCTCTGACTTGCGCAGG	
74	hATP2A2_for	CCGCAACTACCTGGAACCTG	128 bp
75	hATP2A2_rev	TCAGTCATGCACAGGGTTGG	
76	LAMP2_for	GTGCAACAAAGAGCAGACTGT	180 bp
77	LAMP2_rev	ATAAGGAAGCCCAAGGCCAC	

C: *MUSCLEMOTION*

SOP – Cardiomyocyte analysis using *ImageJ* plugin *MUSCLEMOTION*

MUSCLEMOTION is an open source software tool allowing the quantitative analysis of cardiomyocyte contraction, disease phenotypes and drug responses. The software is available as a plugin for *ImageJ* (*Fiji*) and can be downloaded at https://github.com/l-sala/MUSCLEMOTION. The detailed description of the functioning of the algorithm together with a user manual are available upon download and online. The following SOP will give guidelines on the preliminary preparation of videos and their analysis through *MUSCLEMOTION*.

Video acquisition and compression

- Acquire videos noting down the frames per second (fps) used by your device. The higher the number, the more accurate the analysis. In order to check the number of fps after the acquisition, one can use a software such as *VLC* (ctr+I).
- FFmpeg is a command-line program used to compress videos to be able to open them with *ImageJ*. The source code for FFmpeg can be found at https://ffmpeg.org/download.html. Download the file and unzip it.
    a) Windows users
        - Save the file to a folder which is easy to find *e.g.* your C:\ drive
        - In **Start Menu**, right click on **Computer** and choose **Properties**
        - Select **Advanced system settings** and open **Environment Variables**
        - Edit the **Path variable** by adding C:\ffmpeg\bin at the end of the line, making sure there is a semi-colon (;) after the previous folder
        - Go to operating system shell and type ffmpeg -codecs
    b) Macintosh users
        - The package manager *Homebrew* is needed. Go to operating system shell and type /bin/bash -c "$(curl -fsSL https//raw.githubusercontent.com/Homebrew/install/master/install.sh)"
        - Type brew install ffmpeg
- Videos can now be compressed through the operating system shell. To navigate, use the command cd+(folder name); to check sub-folders and files use the command ls. Once the folder containing the video is reached, the conversion from extension .mov to .avi can be obtained by typing ffmpeg -i (input file name).mov (output file name).avi. For the compression of .avi videos, type ffmpeg -i (input file name).avi -pix_fmt nv12 -f avi -vcodec rawvideo (output file name).avi.

Video analysis

- To install the plugin, open *ImageJ* (*Fiji*) and go to **Plugins → Macros → Install**
- Select the .ijm file in the *MUSCLEMOTION* master folder; a "MM" will appear in the tool line
- Open *MUSCLEMOTION* and adjust the parameters accordingly before running the analysis; the number of fps will be required
- First, select the folder where you want your results to be saved and then the compressed, .avi file to analyze